# ISOSPIN MIXING IN $^{21}$NA

by

Timothy Michael Mooney

A dissertation submitted to the faculty of The University of North Carolina at Chapel Hill in partial fulfillment of the requirements for the degree of Doctor of Philosophy in the Department of Physics and Astronomy.

Chapel Hill

1989

Approved by:

Edward J Ludwig
Adviser

Thomas B. Clegg
Reader

W. J. Thompson
Reader

TIM. M. MOONEY. Isospin mixing in $^{21}$Na. (Under the direction of EDWARD. J. LUDWIG.)

## Abstract

Isospin-mixing effects have been studied in resonant $^{20}$Ne(p,p)$^{20}$Ne scattering. New techniques for the acquisition and analysis of excitation-function data have been developed.

A measurement system was developed to acquire high resolution excitation-function data by applying a ramp voltage to the target rod and by monitoring accelerator devices continuously during acquisition. This measurement system was also used to directly measure the beam energy-resolution function. Nuclear-scattering targets were fabricated by low-energy ion-implantation and were found suitable for use in high energy-resolution experiments.

High-lying T = 3/2 states in $^{21}$Na were identified in $^{23}$Na(p,t)$^{21}$Na scattering at an incident proton energy of 40.1 MeV. Excitation functions were acquired, using the high resolution polarized-proton beam at Triangle Universities Nuclear Laboratory, over energy regions in which the lowest seven T = 3/2 states in $^{21}$Na were expected to contribute. Resonances were observed at energies corresponding to the lowest three states. Resonance parameters were extracted from the data using a model-independent helicity-amplitude

analysis in which correlations among the resonance and resolution-function parameters were studied.

Results of the analysis indicate that the correlations can have significant effects on the accuracy of extracted parameter values and that knowledge of the resolution function is essential in determining those values.

Acknowledgements

I thank my advisor, Dr. Ed Ludwig, for his careful, but unobtrusive, attention and guidance; Dr. Tom Clegg for his energetic support and technical expertise; and Dr. Bill Thompson for help with scattering theory, and for many useful suggestions and helpful criticism. I am grateful to these gentlemen and the other members of my doctoral committee, Drs. Eugen Merzbacher and Max Swanson, for the attention and support they gave me.

I greatly appreciate the help of my colleagues, Roy Fauber, Dave Abbott, Jim Bowsher, Eric Crosson, Susan Lemieux, and Tom Spencer, and my teachers, Drs. Chandra Bhat, Hugon Karwowski, and Mark Schnieder, in acquiring and analyzing the data that contributed to this thesis. I thank these gentlemen, this lady, and my friend, Dr. Mark Kellam, for many intelligent discussions from which I learned and which I enjoyed. Thanks, also, to my predecessors, Drs. Pitsa Ikossi, John Wilkerson, Robert Varner, Barry Burks, and Tom McAbee, upon whose work this thesis project was built.

This work would not have been possible without the expert assistance of Messrs. Bob Rummel, Paul Carter, Sidney Edwards, Pat Mulky, Al Lovette, Chris Westerfeldt, and Larry Simpson, and the considerate authority of Dr. Ed Bilpuch. Mr. Mark Boyd, and Drs. Chris Gould

and Russel Roberson made substantial contributions which I gratefully acknowledge. I also thank Drs. Art Champagne and Dick Kouzes, and the staff of the Princeton Cyclotron Laboratory for their efforts in my behalf.

I thank my wife, Susan, whose loving support has made this work seem greatly more substantial and rewarding and, when necessary, irrelevant--a rich contradiction I hope I will never fully understand.

This work was supported in part by a grant from the Department Of Energy.

# Table of Contents

# Table of Figures

# 1. Introduction

## 1.1 Brief introduction to isospin

Protons and neutrons resemble one another closely. They have the same values of intrinsic quantum numbers, such as spin, and nearly identical masses. Also, they respond similarly to the nuclear force: a reasonable first approximation to the nuclear Hamiltonian ignores the differences between them. However, for the purpose of applying the Pauli Principle to wave functions made up of them, protons and neutrons cannot be regarded as identical in *any* approximation.

The isospin formalism addresses this dichotomy by positing the neutron and proton as two states of a single particle, the *nucleon*, which has all of the quantum numbers the neutron and proton hold in common, and an additional quantum number, called isospin, by which the neutron and proton states are distinguished. Within the formalism, then, the proton and neutron do not exist separately of each other; they are one object seen from two different points of view, and that object is a two-member family of states identified by the isospin quantum number. A wave function made up of many nucleons is, similarly, a family of (one or more) states which differ in relative numbers of protons and neutrons, but which have the same total number of nucleons. Such a family is called an isospin multiplet.

### 1.1.1 The mechanism of isospin

Isospin is implemented with two related quantum numbers, T and $T_3$, which can be interpreted as the norm (T) and projection ($T_3$) of a vector-valued quantum number T. (T is a vector in the fictitious three dimensional space called "charge space". See, e.g., [Bay66]). For a single-nucleon wave function, the value of $T_3$ distinguishes between the proton ($T_3 = -1/2$) and neutron ($T_3 = +1/2$) states. (Note that the assignment of $T_3$ in nuclear physics is opposite to that used in high-energy physics.) The value of T is determined from the number (2T+1) of different values of $T_3$ which are observed--just as the angular momentum quantum number J is obtained from the number (2J+1) of eigenvalues of $J_z$. For the nucleon, $T = 1/2$.

For a multi-nucleon wave function, $T_3$ generalizes simply [Bay66] to the definition $T_3 = {}^1/_2(N-Z)$, where N and Z are the numbers of neutrons and protons which make up the wave function. T continues to indicate the number of allowed values of $T_3$.

Evidently, when $T_3$ describes a wave function of A nucleons, the values it can assume must fall in the range [-A/2 ... +A/2]. But, for many wave functions, the Pauli Principle further restricts $T_3$. For example, in the $A = 2$ system $T_3$ is restricted by its definition to the range [-1 ... +1]; however, for a particular $A = 2$ state that consists of a proton and a neutron with (otherwise) identical quantum numbers, $T_3$ can only equal zero since any other value implies a wave function of two identical particles. In other words, a two-nucleon wave function

whose spatial and spin components are symmetric under nucleon interchange must have an antisymmetric isospin component: the two nucleons must have opposite isospin, which excludes $T_3 = \pm 1$.

Thus far, the value of T has been seen as following from the range of allowed values of $T_3$, rather than the reverse, partly because discussion involving the Pauli Principle seems less verbally clumsy with this choice. The opposite viewpoint normally leads to an unintuitive discussion of isospin as a permutation symmetry. It encourages one to abstain--witlessly--from thinking about protons, neutrons, and the individual states of an isospin multiplet, and instead somehow to intuit the multiplet as a whole. This viewpoint is the more usual one, however, and it is preferable for several reasons: it is the "viewpoint" of the isospin-conserving Hamiltonian and thus seems more in keeping with the philosophy of isospin; it corresponds better with the way we view angular momentum, which, mathematically, is exactly analogous to isospin; and it focusses attention on T, rather than on $T_3$. Attention *should* be focussed on T, since this quantum number carries new information about a nuclear state, while $T_3$ is redundant, given A and Z.

### 1.1.2 Charge symmetry and charge independence

A Hamiltonian that does not distinguish in any way between protons and neutrons is said to be "charge independent". A Hamiltonian under which neutron-neutron interactions are exactly the same as proton-proton interactions is said to be "charge symmetric" (and may or may not also be charge independent). Only charge-independent

Hamiltonians conserve isospin.

### 1.1.3 Example: a T = 1 isospin multiplet

The nuclear configuration that consists of two neutrons with identical quantum numbers except for intrinsic-spin projection is the $T_3 = 1$ member of a T = 1 isospin multiplet. Such a multiplet is shown in the diagram of figure 1.1. The leftmost configuration in the diagram is the state described above; as the most neutron-rich member of the multiplet, it is conventionally called the "parent" state. In the diagram, intrinsic quantum numbers (spin and isospin) are shown explicitly; extrinsic quantum numbers (all others) are represented by "levels", each level representing some unique combination of extrinsic quantum numbers. (Since both neutrons occupy the same level, only one level is shown.)

If both of the neutrons in the parent state are transformed into protons, without changing any of their other quantum numbers, a charge-symmetric Hamiltonian will not notice the difference. The resulting state (the right-most configuration in the diagram) is said to be an "(isobaric) analogue" of the parent state since, to the extent that the Hamiltonian is charge symmetric, the two states have identical structures and binding energies.

If only one of the neutrons in the parent state is transformed into a proton, the situation is more complicated because the two possible transformations do not yield eigenstates of T. However,

## 1.2 Motivation for the project

This thesis is part of an ongoing study, undertaken by the UNC Nuclear Physics group at TUNL, of isospin-forbidden processes in nuclear scattering. A principal objective of the study is to provide data which can usefully direct or constrain theoretical consideration of the following questions:

1) What are the mechanisms by which the nuclear force violates isospin conservation?

2) To what extent is the violation of isospin conservation observed in nuclear scattering attributable to non-Coulomb components of the nuclear Hamiltonian?

3) What nuclear-structure information can be gained by studying scattering processes through the "filter" that a small violation of isospin conservation represents?

This thesis summarizes a study of the isospin-forbidden formation and decay of T = 3/2 compound-nucleus states in $^{21}$Na which occur in $^{20}$Ne(p,p)$^{20}$Ne scattering.

### 1.2.1 Isospin-forbidden compound-nucleus formation and decay

Formation of T = 3/2 states by $^{20}$Ne(p,p)$^{20}$Ne is isospin forbidden for the following reasons: the isospin of the ground state of $^{20}$Ne is 0; the isospin of the proton is 1/2; and the isospin of a compound

state is the vector sum of the component isospins. To the extent that isospin is conserved in $^{20}$Ne(p,p)$^{20}$Ne scattering, then, compound states formed in the process have isospin T = 1/2. But T = 3/2 states *are* formed by $^{20}$Ne(p,p)$^{20}$Ne, indicating that isospin is not strictly conserved in the scattering process--or, equivalently, that one or more of the participants in the process are not states of good isospin. It is universally assumed that the participants are, nevertheless, expressible as superpositions (colloquially, "mixtures") of such states and, under this assumption, the extent of the mixing parameterizes the violation of isospin conservation. When this work was begun, the nature and extent of the isospin mixing that occurs in light nuclei were not well established despite considerable experimental and theoretical effort (see, e.g., [Hin84], [Mcd76], and [Aue83]).

The T = 3/2 states, once formed, are relatively long lived (compared to T = 1/2 states in the same nucleus) because their decay by proton emission is also isospin forbidden. Therefore, via the Heisenberg Uncertainty Principle, the states have relatively well-defined energies. The T = 3/2 states, then, can be expected to contribute to excitation functions of $^{20}$Ne(p,p)$^{20}$Ne only over a relatively narrow (<1 keV, as it turns out) range of incident proton energies. This range is customarily called $\Gamma$, the resonance full width.

Here, then, is a means by which violations of isospin conservation in $^{20}$Ne(p,p)$^{20}$Ne can be quantified: measurement of the energy range $\Gamma$ over which a T = 3/2 state contributes to excitation functions

of $^{20}Ne(p,p)^{20}Ne$ is measurement of the lifetime of that state and is, therefore, measurement of the violation which allows its decay. (As we'll see shortly, $\Gamma$ is somewhat ambiguous as an indicator of isospin-conservation violation because it can include other effects. The more specific indicators are closely related to $\Gamma$, however, and the physical picture presented thus far is correct, if incomplete.)

### 1.2.2 Isospin mixing

As was mentioned above, isospin-conservation violations are frequently discussed in terms of the mixing between states of good isospin, eigenstates of the isospin-conserving and dominant component $H_0$ of the nuclear Hamiltonian H, under the action of the relatively small isospin-nonconserving (INC) components: collectively, $H_{INC}$. The INC components usually considered are the isovector and isotensor parts of the Coulomb potential. The isovector part can mix states that differ in T by one; the isotensor part can mix states that differ by one or two.

In an isospin-forbidden resonance experiment, the resonance effect is attributed to isospin admixtures in the nominally T = 0 target nucleus (ground state, in the usual case of elastic scattering) and in the resonant compound-nucleus state; admixtures in the projectile are usually ignored. The target ground state mixes with T = 1 and T = 2 states in the same nucleus of the same spin and parity. The nominally T = 3/2 compound nucleus can mix with the anti-analog state, nearby T = 1/2 states of the same spin and parity, and directly with the

continuum via the two-body Coulomb potential [Aue83].

Thus, there are a three conceptually distinct processes by which a nominally T = 3/2 compound-nucleus (CN) state can decay by proton emission to a nominally T = 0 target ground state:

1) The T = 3/2 majority of the CN state can decay via $H_0$ to a T = 1 admixture in the target ground state.
2) A T = 1/2 admixture in the CN state can decay via $H_0$ to the T = 0 majority of the target ground state.
3) The T = 3/2 majority of the CN state can decay via the two-body Coulomb part of $H_{INC}$ to the T = 0 majority of the target ground state. (This process contributes only to proton decays [Aue83].)

Since the division of H into separate pieces is purely a mathematical convenience, we expect these processes to operate in parallel and to interfere with each other.

There is no reason to expect, a priori, that effects of these processes can be disentangled by comparing data from a single decay with theoretical calculation of that decay. Rather, one hopes the different processes differ systematically in their effects so that trends in the data collected from many different decays can be compared against these systematic differences. One prerequisite to such a study of trends is a basis for comparing results from different decays and from decays involving different nuclei.

### 1.2.3 Resonance widths and isospin mixing

To facilitate comparisons between different experiments, and between experiment and theory, a systematic procedure for reporting resonance widths that signify isospin-conservation violations has evolved. The full width $\Gamma$ cannot be compared directly since it contains effects of isospin-allowed decay modes. A quantity of more direct interest in proton-scattering experiments is the *partial width* $\Gamma_p$ ($\Gamma_n$ for neutron-scattering, etc.) which would be the resonance width in the absence of any decay mode other than (isospin-forbidden) proton emission from the T = 3/2 compound-nucleus state to the observed final state. (When decays to more than one final state are considered, the final state is normally indicated by an additional subscript. For example, $\Gamma_{p0}$ is the partial width for proton decay to the target ground state.)

But $\Gamma_p$ is yet not a pure indicator of the extent to which isospin conservation has been violated. The lifetime (and thus, the partial width $\Gamma_p$) of a compound-nucleus state that decays by proton emission depends also on the Coulomb and angular-momentum barriers through which the ejectile must tunnel. To remove the effects of these dependences, $\Gamma_p$ is divided by twice the Coulomb penetrability, yielding the *reduced width* $\gamma_p^2$. This is sometimes divided by $\hbar^2/2mR^2$, an estimate of the single-particle reduced width, yielding a quantity we'll denote by $\theta_p^2$. The quantity $\theta_p$ is called the *isospin-mixing amplitude* and is the basis for comparison between experiment and theory and among results obtained for different nuclei. Thus, $\theta_p$ nicely bridges

the gap between experiment and theory since its square is the spectroscopic factor for the decay of the compound-nucleus state to the target ground state.

It should be clear that $\theta_p$ does not represent the total isospin impurity of any one of the states participating in the resonant scattering process, but is an indication of the impurity of all of them. Furthermore, the isospin-mixing amplitude $\theta_p$ doesn't represent all of the existing impurity, but only the portion that has observable effects in the particle decay studied.

## 1.3 Previous work

A considerable amount of experimental and theoretical work has been done in the hope of discovering the mechanisms responsible for violations of isospin conservation in low-mass nuclei. Much of this work has involved acquiring and analyzing data from single-nucleon, elastic scattering from nuclei of mass A = 4n (where n is an integer and A is in the range [8...40]) and attempting to understand the results that evidence violations by performing model calculations of the processes involved.

Light nuclei of mass A = 4n are particularly appropriate targets in a systematic scattering study of isospin violations for several reasons: all of these nuclei are stable; the ground states of all have spin and parity $0^+$, which simplifies theoretical calculations of elastic-scattering observables, allows a relatively unambiguous calculation of

the Coulomb penetrability and, by this, facilitates comparison between experiment and theory; and the ground states of all have isospin T = 0, rendering the isospin coupling between projectile and target unique.

But perhaps the most important reason for the choice of A = 4n nuclei is that the lowest-energy, nominally T = 1 states in these nuclei are fairly high (between 10 and 17 MeV) in excitation energy. Therefore, isospin-allowed nucleon decay from low-lying T = 3/2 compound-nucleus states formed in proton or neutron scattering from these nuclei to those T = 1 states is energetically impossible. The fact that the isospin-forbidden decay of the T = 3/2 states is observable at all in resonance experiments is attributable, in large part, to this fact.

Recently, a systematic study of isospin-forbidden resonances observed in proton scattering on A = 4n nuclei was done by Wilkerson [Wil82], who measured resonance widths of several of the lowest-energy T = 3/2 states in $^{13}$N, $^{17}$F, $^{25}$Mg, $^{29}$P, $^{33}$Cl, and $^{37}$K with polarized beam. Prior to that, Ikossi [Iko75] had measured resonance widths in the compound nuclei $^{25}$Al, $^{29}$P, and $^{33}$Cl with unpolarized beam, and had re-analyzed a resonance-width measurement in the nucleus $^{21}$Na performed by McDonald [Mcd69]. Proton-scattering measurements earlier than these are summarized in [Iko75].

A body of neutron-scattering data from isospin-forbidden compound-nucleus formation was also accumulated by a number of

studies performed in the past decade or so ([Hin84], and references therein). These data are less extensive than the proton-scattering data and comprise resonance widths of T = 3/2 states in $^{17}O$, $^{21}Ne$, and $^{25}Mg$. (Low-lying T = 3/2 states in heavier A = 4n, $T_3$ = +1/2 nuclei are bound with respect to neutron decay.)

Of particular relevance to this thesis are previous studies involving the mass-21 system: the $^{20}Ne(p,p)^{20}Ne$ study of [Mcd69] and [Iko75]; the $^{20}Ne(n,n)^{20}Ne$ study of [Hin84]; and a number of studies in which mass-21, T = 3/2 states were populated by isospin-allowed reactions. In the last group is the $^{17}O(\alpha,n)^{20}Ne$ reaction study [Mcd76] of a resonance in $^{21}Ne$, and studies which, for purposes here, serve simply to verify the T = 3/2 character of states in mass-21 nuclei (e.g., [Mai81]).

### 1.3.1 Trends in previous data

Among the scattering-data results, there are three significant trends:

1) Within the mass range [8...40], observed isospin-mixing amplitudes are systematically larger in heavier nuclei than in lighter nuclei, following approximately a power-law dependence on A. In proton decays, for example, observed amplitudes are proportional to $A^{4/3}$ [Wil82].

2) Amplitudes extracted from neutron-scattering data are larger than those extracted from proton-scattering data and increase more

swiftly with A.

3) Amplitudes extracted from elastic proton scattering through lowest-energy T = 3/2 compound-nucleus states, seen as a function of mass number A, oscillate with period A = 8. Amplitudes from inelastic proton scattering to the lowest excited state do not seem to exhibit this periodicity [Mcd76]. No significant oscillation with A has been observed in the amplitudes extracted from the less precise neutron-scattering data.

Observed amplitudes of different T = 3/2 states (of various spins and parities) in the same nucleus vary with the excitation energy of those states, but data are insufficiently extensive to describe the variation as a trend. In $^{29}$P, the nucleus for which the greatest number of T = 3/2 states have been studied, the amplitudes decrease with excitation energy [Wil82]. This finding has been used to suggest that the predominant source of isospin mixing is not in the compound system, since T = 3/2 states at higher excitation energies might be expected to have larger mixing amplitudes as a result of the increased density of T = 1/2 states with which they can mix.

### 1.3.2 Previous interpretations

For purposes here, the intent of isospin-mixing calculations is to interpret experimental data by relating theoretically-determined isospin admixtures to the isospin-mixing amplitudes $\theta_p$ extracted from those data. As we have seen, there is ample room for confusion in this

relation, and understanding the implications of some isospin-mixing calculations is difficult for this reason. For example, two early studies calculated comparable total admixtures into the target ground state from T = 1 states generally, and from the isovector-monopole state only. (The isovector-monopole state has been described hydrodynamically [Boh69] as a collective, breathing-mode vibrational state in which protons oscillate against neutrons.) The total isospin impurity in the ground state is interesting, but not directly useful information, in context here, because the decay probability of a T = 3/2 state to that ground state also depends on spectroscopic factors for decay to the admixed wave functions.

Many of the early calculations of isospin mixing were targeted at one or a few mixing mechanisms, a single nucleus, or a single systematic feature of the data that existed at the time. Several such calculations are described in [Iko75], [Wil82], and [Aue83], and they will not be reviewed here.

A systematic calculation of proton-decay, isospin-mixing amplitudes for the lowest-energy, T = 3/2 states to T = 0 ground states [Aue71] found total isospin-mixing amplitudes of approximately the same order of magnitude as experimentally determined amplitudes. This calculation also found that isovector-potential mixing with the anti-analog state dominated, and that "direct mixing" (decay not involving the isospin conserving Hamiltonian) via the two-body Coulomb potential had relatively little effect. The role of the

isovector-monopole state, which dominates isospin mixing (but, significantly, not isospin-forbidden escape widths [Aue83]) in low-lying states of heavy nuclei, was found to be small but not negligible.

Another isovector-potential calculation [Ari71] of proton-decay amplitudes focussed on mixing of the nominally T = 3/2 compound-nucleus state with other states of the same spin and parity, and also included T = 1 admixtures into the target ground state. This relatively complete calculation agreed with the experimentally determined isospin-mixing amplitudes. However, one of the objectives in the calculation was to investigate the sensitivity of the results to various types of wave functions used and an appreciable sensitivity was found.

Recently, shell-model calculations of isospin mixing in the compound nucleus of T = 3/2 states with nearby T = 1/2 states have been performed [Orm86], using the shell-model code OXBASH, for several nuclei in the mass-number range [21...37]. The principal objective of these calculations was to give some insight into the cause of the observed oscillatory behavior of isospin-mixing amplitudes in this range.

In the OXBASH calculations, isovector and isotensor components of $H_{INC}$ were arrived at empirically by assuming a parameterized form for $H_{INC}$ and fitting the parameters to experimentally determined mass differences between different members of several isospin multiplets. It has been observed [Aue83] that calculations of these mass differences

are consistently three to six percent smaller than observed differences. To use, in isospin-mixing calculations, a Hamiltonian derived purely from theory would be to ignore this discrepancy as a source of information.

Any calculation of isospin mixing between (nominally) T = 3/2 states and nearby T = 1/2 states in the compound nucleus must be sensitive to the energy differences between the mixed states, and these energy differences are a principal source of imprecision in the OXBASH results. Calculated energies of T = 1/2 states were assumed imprecise by 500 keV. The procedure used to estimate the effects of this imprecision on the resulting isospin-mixing amplitudes was to perform the mixing calculation many times while systematically varying the assumed energy differences, in steps of 10 keV, over the $\pm$500 keV range.

Results of the OXBASH calculation agree generally, within errors, with experimentally determined isospin-mixing amplitudes. But the imprecision in the calculated results is so large that there is essentially no sensitivity in the comparison between experiment and theory to the oscillatory behavior of the observed mixing amplitudes. This calculation could be made greatly more meaningful if experimentally determined excitation-energy differences could be used as input.

One mixing mechanism has been proposed, thus far, that directly addresses the subject of the A = 8 periodicity in isospin-mixing decay

amplitudes [Wil83]. The proposal is schematic, rather than the result of detailed calculation. The mechanism proposed is the admixture of $T = 3/2$ nucleon-isobar, or $\Delta$-particle, components into any or all of the participating wave functions. This mechanism also addresses the disparity between observed neutron- and proton-decay mixing amplitudes. The magnitude of the indicated isobar amplitude in light nuclei is consistent with an independent experimental estimate.

### 1.3.3 Summary

As yet there is no clear understanding of the isospin-forbidden decays observed in light-ion resonance experiments. Some of the trends in the data are understood in principle, which is to say that an isospin-mixing mechanism has been demonstrated by calculation to have the potential of reproducing a particular trend, or that the form of the INC Hamiltonian that must be involved is known. But there is no hard and fast connection between mixing mechanisms and trends in the data.

It is generally acknowledged [Aue83] that the magnitude of the observed mixing amplitudes can be explained (at the level of precision attained to date by experiment and theoretical calculations) without recourse to any purely nuclear contribution to $H_{INC}$; i.e., the Coulomb potential suffices. With the possible exception of the $A = 8$ periodicity, it seems that no feature of the particle-decay data demands other-than-Coulomb contributions either.

That predominantly iso*vector*-potential calculations of several different mixing mechanisms should yield independently results comparable to or larger than experimental results, coupled with the observation [Mcd76] that the large difference between neutron- and proton-decay mixing amplitudes requires a significant contribution from iso*tensor* mixing in the compound nucleus, together all but declare that observed effects result in part from interference between mixing mechanisms none of which dominate (see, e.g., discussion in [Wil83]).

## 1.4 Overview of current measurements in the A = 21 system

Several of the lowest-energy T = 3/2 multiplets in the mass-21 system are shown in figure 1.2. Energy scales for the nuclear level diagrams have been translated so that the lowest-energy T = 3/2 states all appear at the same level. In figure 1.3, some of the nuclear scattering and reaction data acquired for this thesis are shown in condensed form.

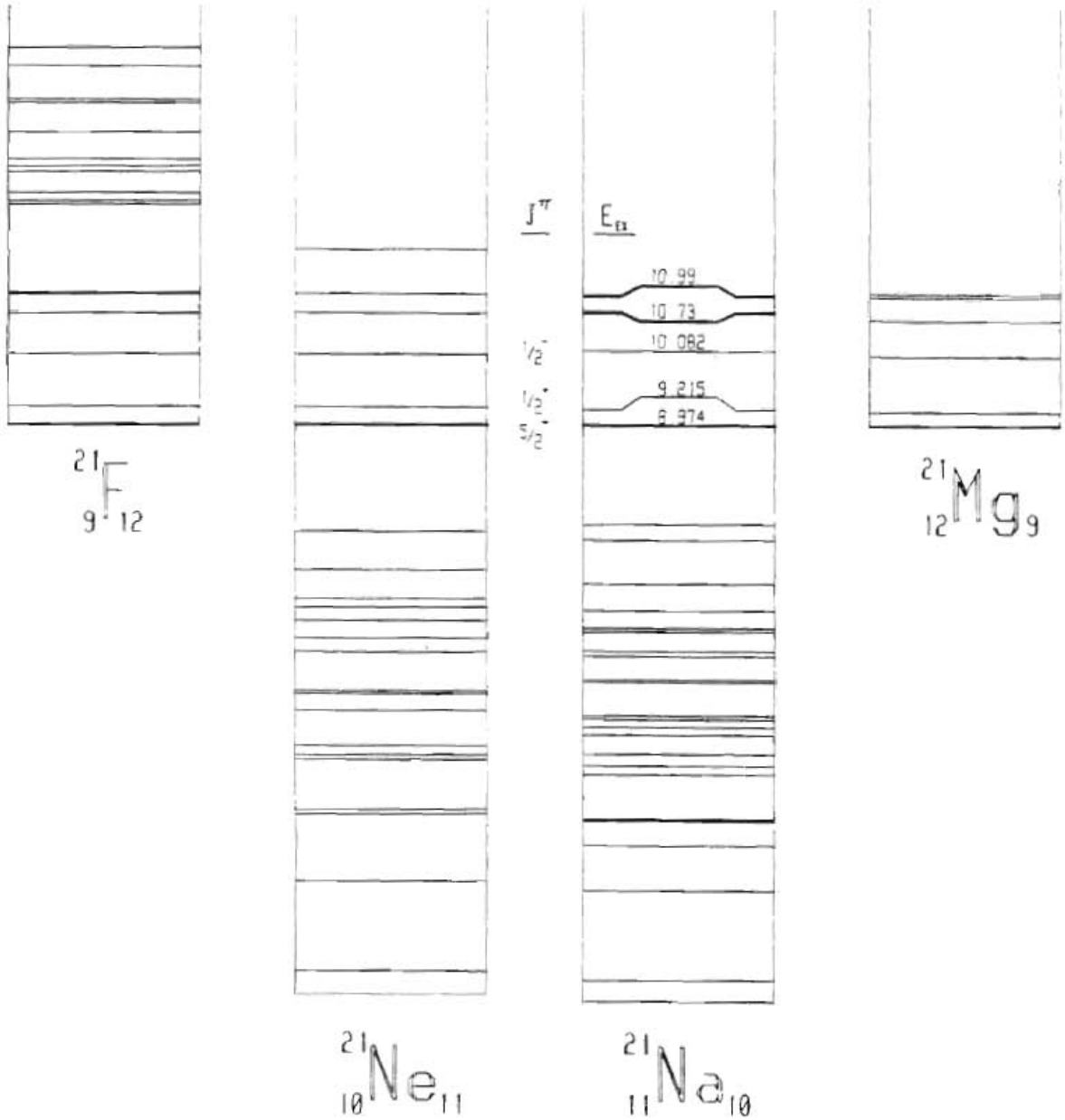


Figure 1.2 The lowest-energy T = 3/2 multiplets in the mass-21 system.

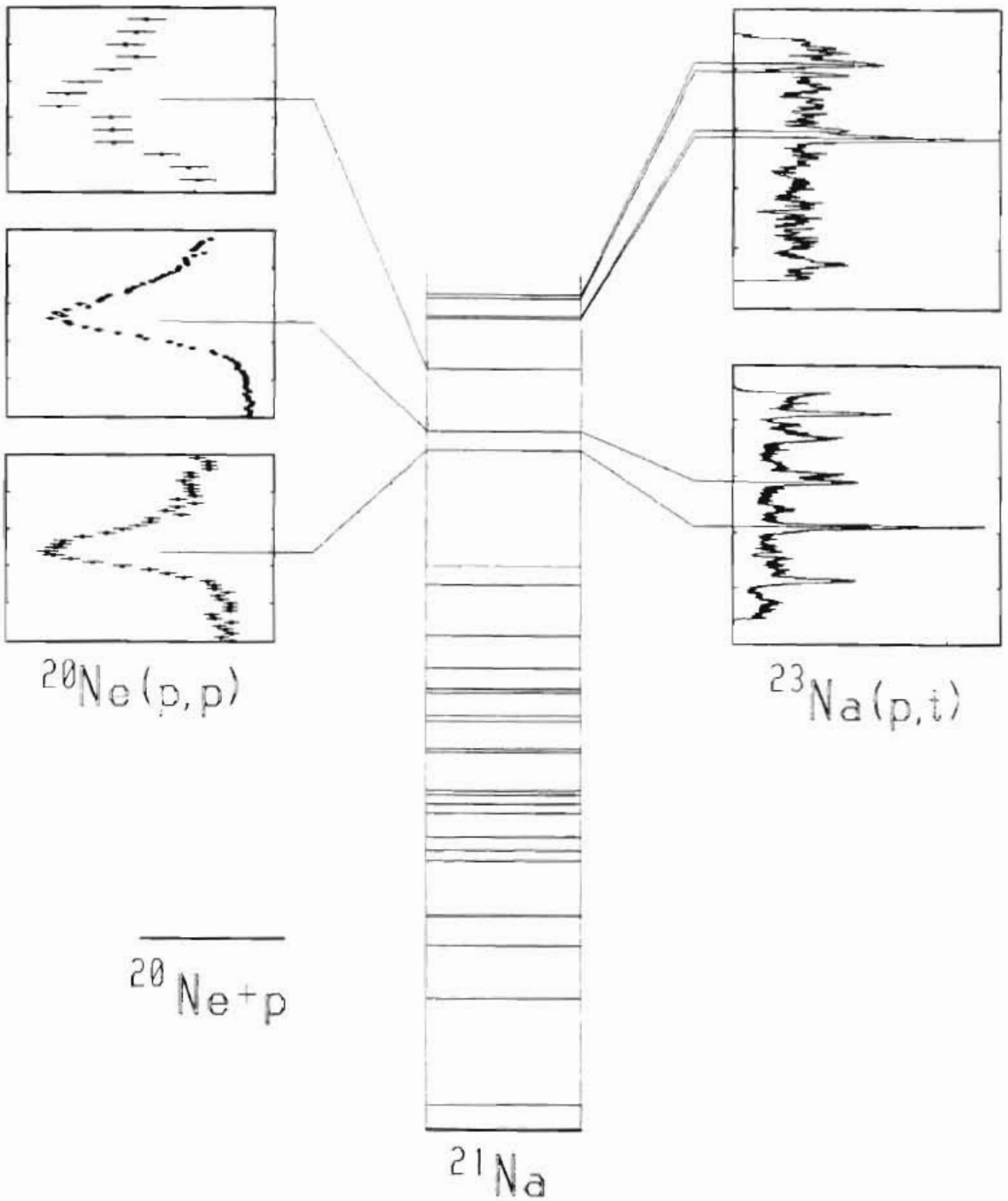


Figure 1.3 Summary of acquired scattering and reaction data involving T = 3/2 states in $^{21}$Na.

# 2. Development work

## 2.1 Upgrade of the TUNL high resolution system

### 2.1.1 Background

The TUNL high energy-resolution system (see fig. 2.1) is a system of active and passive beam handling devices whose purpose is to accelerate and focus on target a beam of light ions that is as nearly monoenergetic as possible. Since the system is fully described elsewhere (see, e.g., [Wil82], [Ble78]), only selected details will be presented here.

A central component of the system is the dual 90-degree, energy-analyzing magnet system--the "90-90" system. This system improves the beam resolution by blocking passage of particles whose energies lie outside a very narrow range (approximate width: 1/5800 of the nominal beam energy). It operates by magnetically inducing a correlation between beam energy and beam trajectory, and intercepting all but a narrow range of trajectories on a beam slit, the "analyzing slit".

The field in the upstream analyzing magnet is monitored by an NMR Gaussmeter, which is the energy-calibration reference for the 90-90 magnet system. An error signal from this Gaussmeter is fed to

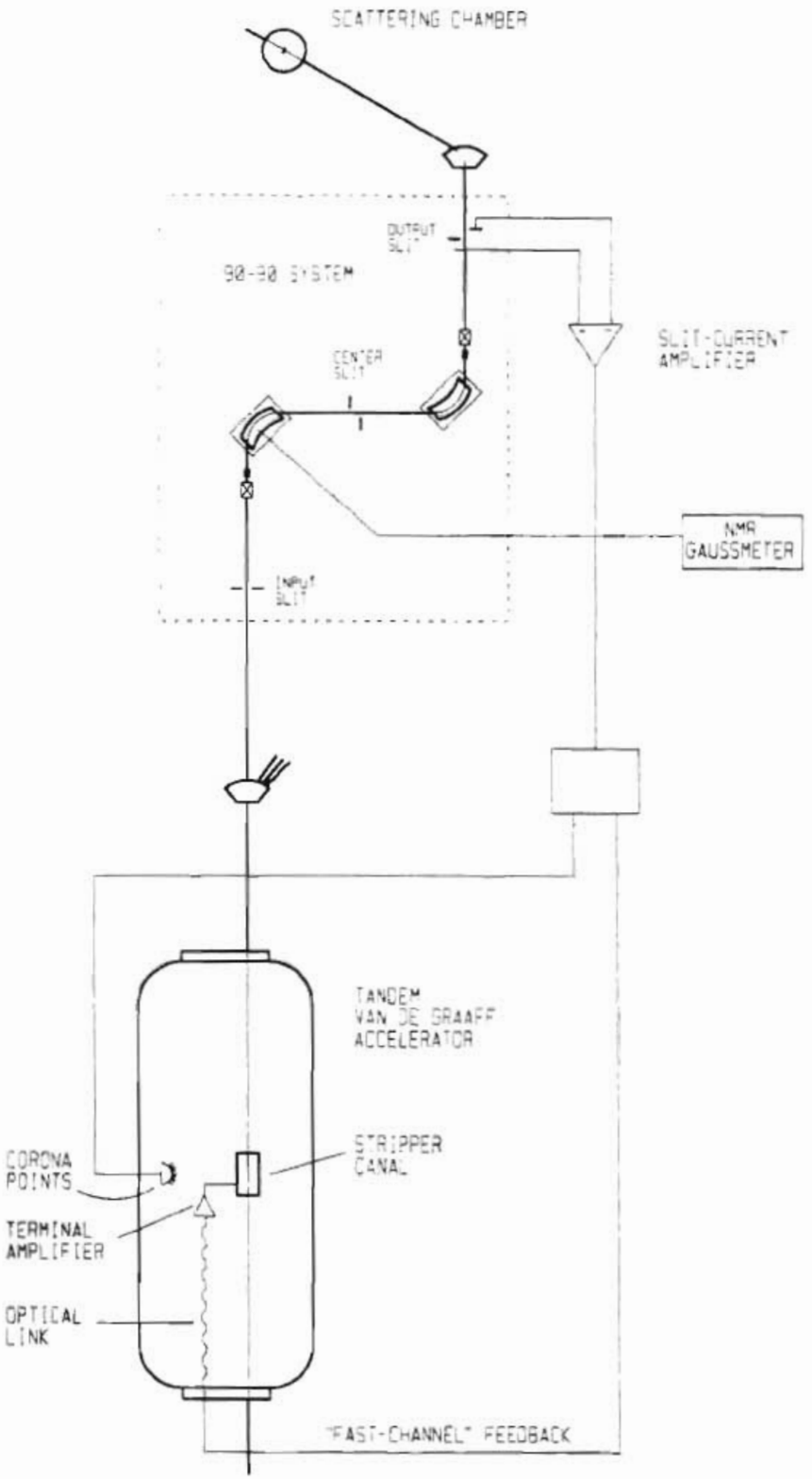


Figure 2.1 The TUNL high energy-resolution system.

the Master Reference Proportional Controller, a voltage source that modulates the setpoint of the analyzing-magnet power supply and those of all other magnet power supplies in the high-resolution system.

A fairly recent addition to the high-resolution system is the "fast-channel feedback system" [Ble78] whose business end is a high-voltage power supply, the "terminal amplifier", located at the center of the tandem Van de Graaff accelerator. The purpose of the feedback system is to null residual voltage fluctuations in the tandem, thereby maximizing the amount of beam transmitted by the 90-90 system and, it is hoped, improving the beam energy resolution. In operation, the system attempts to keep the beam centered within the analyzing slit by applying a correction voltage to the tandem stripper canal in response to a feedback signal derived from the beam current intercepted by the slit.

While the principle underlying slit-feedback control of the tandem is simple (see fig. 2.2a), the circumstances under which current intercepted by the analyzing slit can be used to improve beam energy resolution deserve discussion. (For brevity's sake, only the upstream magnet will be discussed; the two magnets are nearly identical.) In the correlation between beam energy and position that exists at the analyzing slit, the mapping of energy to position is not unique, as is suggested by figure 2.2a, because the object slit (opening) of the 90-degree magnet system is not infinitesimally narrow.

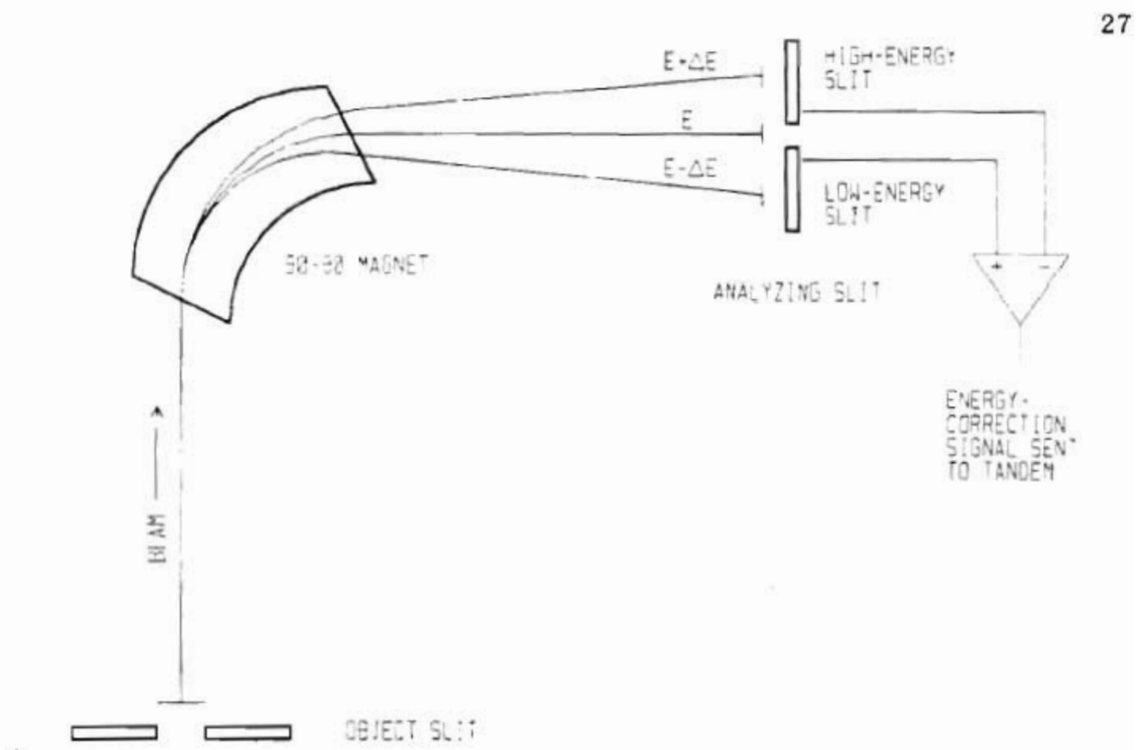


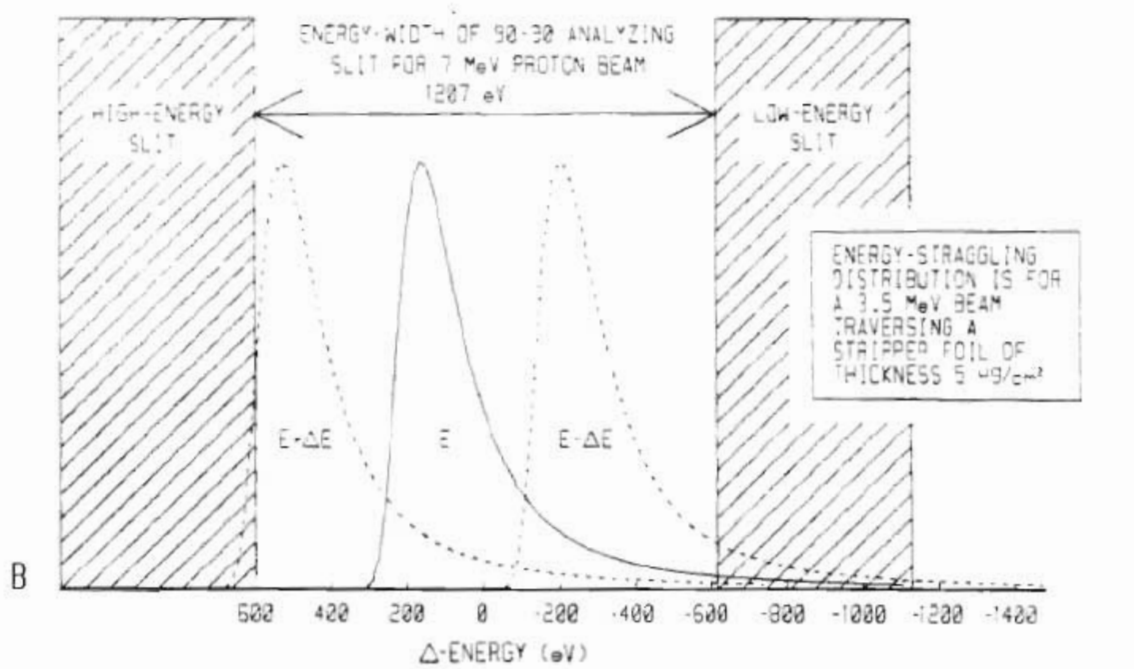


**Figure 2.2 The principle underlying slit-feedback control of the tandem.**

If the object slit had infinitesimal width, and the energy-to-position mapping were unique, little of a centered beam whose energy distribution was much narrower than the energy width of the analyzing slit would be intercepted by either slit. In this case, nearly the same feedback signal would be produced for a range of centroid beam energies. For example, figure 2.2b shows the instantaneous energy distribution of a nominally 7-MeV beam, which was monoenergetic before passing (at 3.5 MeV) through a 5 ug/cm$^2$ carbon foil in the tandem stripper canal, superimposed on the analyzing slit. The distributions rendered in dashed lines show the extremes of centroid beam energy within which essentially no beam would be intercepted by the slit. With the beam energy between these extremes, the slit-feedback amplifier, responding to balanced (at zero) slit currents, would call for no energy correction. Thus, even under feedback control, this beam could "rattle" back and forth within the analyzing slit, and only a marginal improvement in beam energy resolution would result.

But such is not the case. The object slit is 2 mm wide; the 90-degree magnet and its associated lenses produce a 1 mm image of this object at the analyzing slit, which is 1 mm wide (see fig. 2.3a). The implication of the resulting energy-to-position mapping can be described by assigning an energy-dependent transparency to the analyzing slit (see fig 2.3b). Assuming perfect beam optics (perfect focussing and alignment, and slit widths commensurate with the system magnification), the slit is completely transparent to beam of precisely the desired energy E, completely opaque to energies that differ from E

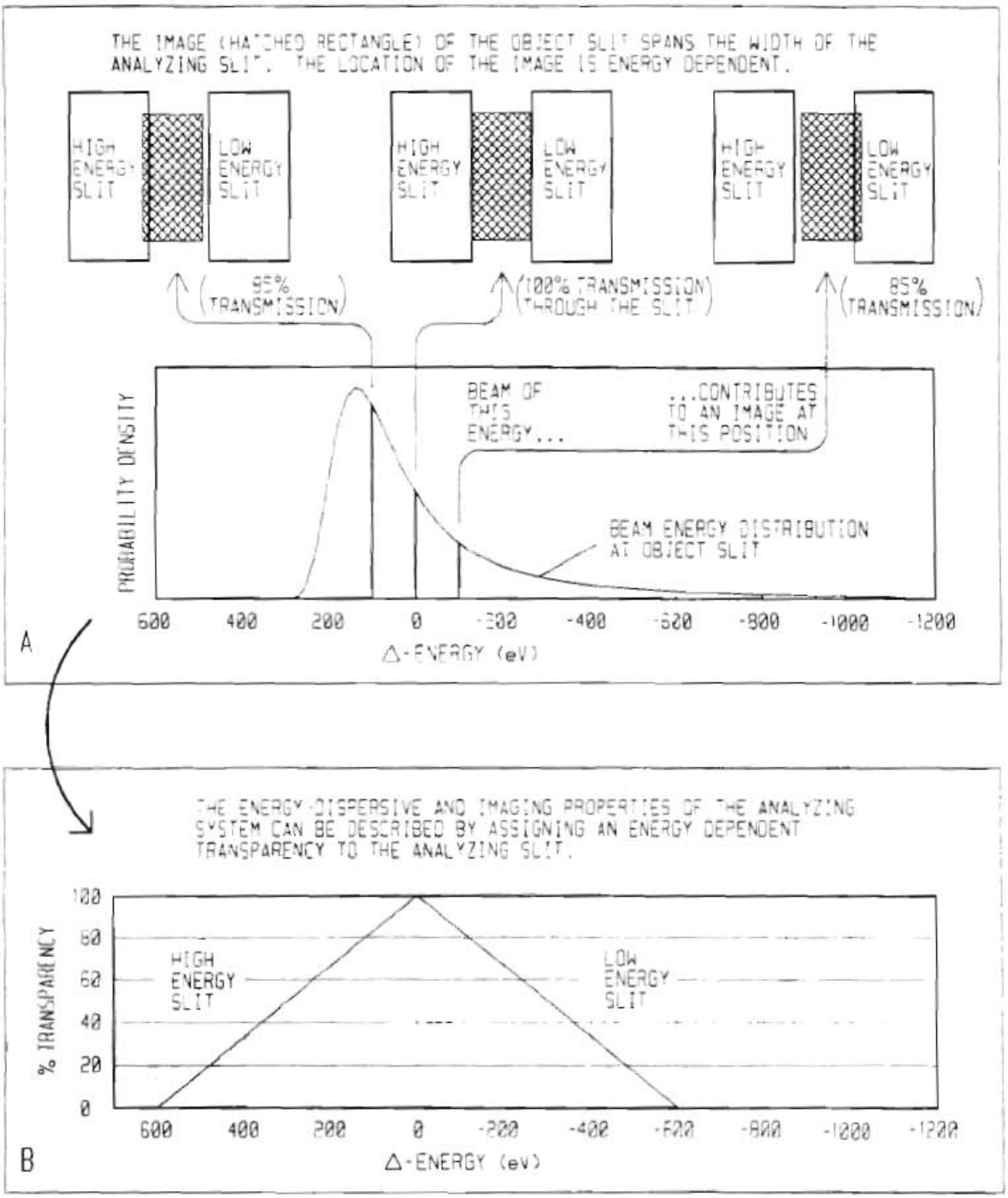


Figure 2.3 The effect of a non-zero analyzing-slit width.

by more than 1 part in 5800, and partially transparent in between. (Under the additional assumption that image position is linearly related to beam energy in the vicinity of the slit, the transparency is a piecewise linear function of energy, as shown in fig. 2.3.) Thus, beam of practically all energies is intercepted to some extent by the slit, and removal by feedback-control of all time-dependent contributions to the beam resolution function is, in principle, possible.

### 2.1.2 Motivation

Some excitation-function data previously acquired by the UNC Nuclear Group [Wil82], using the TUNL high-resolution system, contain features thought to be artifacts caused by uncontrolled and undetected variations in beam energy. The development projects described below are attempts to combat these energy variations in one or more of the following ways: by preventing them from occurring; by detecting them so that contaminated data can be discarded and retaken; and by acquiring data in such a way that artifacts due to energy variations can be removed during offline analysis.

### 2.1.3 The beamline-monitor system

The TUNL high-resolution system energy calibration depends in part on a correlation, induced by the 90-90 magnets, between beam energy and the position of the beam at the analyzing slit. Therefore, variations in the trajectory of the beam, as it travels through the 90-90 system, that are *not* induced by the 90-90 magnets, or that are inappropriately correlated with beam energy, can be misinterpreted by the system. There are many possible sources of such variations: essentially all of the beam-handling devices upstream from the analyzing slit are possible culprits.

The beamline-monitor system is a collection of measuring devices whose main purpose is to detect unwanted variations in beam trajectory, typically by measuring the fields in the beam handling devices of the high-resolution system. The system is divisible into two independent subsystems: the slow-channel monitor, and the NMR interface.

A secondary purpose of the monitor system is to record the fields for later use in reproducing the same "beam tune." This purpose is served almost entirely by the slow-channel monitor.

#### 2.1.3.1 The slow-channel monitor

Magnetic lenses, steerers, and most other beam-handling devices are monitored by a CAMAC-based analog-to-digital converter, the "Borer ADC", which is equipped with an analog multiplexer. Typically, the voltage across a shunt resistor, in a lens or steerer power supply,

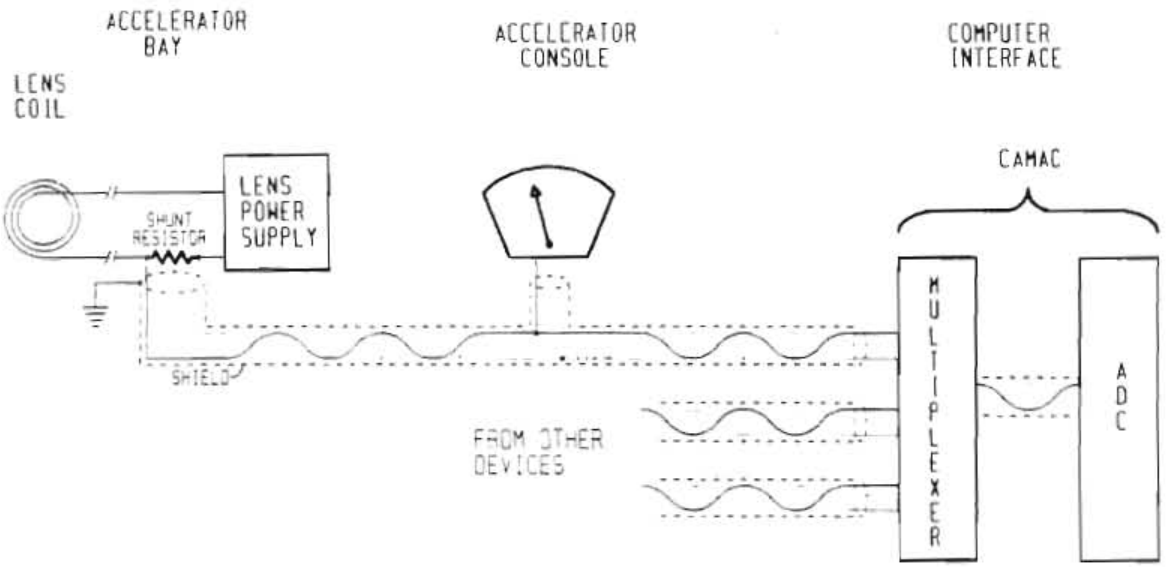


Figure 2.4 A typical signal path in the beamline-monitor system.

is fed through the multiplexer to the ADC (see fig. 2.4).

Several features of the Borer ADC render it particularly suitable for this application. The ADC is (optically) isolated: it returns all of the current used for a voltage measurement back to the voltage source; thus, no net charge is transferred from the measured device to the measuring instrument. This is important because TUNL maintains two separate ground lines: a "clean ground" for sensitive electronics, and a "dirty ground" for electrically noisy devices. CAMAC uses clean ground; lens and steerer power supplies use dirty ground; a non-isolated ADC would destroy the electrical separation between the two. Another feature is that the Borer ADC ignores the moderate common-mode voltage difference between clean and dirty grounds and withstands large common-mode voltages. A third useful feature of the ADC is that it converts voltages by integrating them over a period of 1/60 second. While this conversion method is relatively slow, it rejects noise at multiples of the 60 Hz line frequency.

The slow-channel monitor can be used in two different ways. During acquisition of scattering data, the Borer ADC can be directed by a VAX subprocess to measure voltages periodically from a small number of devices, plot the values in an XSYS [Gou81] data area, and alert the experimenter if a voltage varies from a preset range. Independently of this use, the system can measure a selected set of devices and store the measurements in a database for later recall.

The database function of the slow-channel monitor is provided by the private XSYS programs NEWLOG and OLDLOG, and the interactive program SEARCHLOG.

NEWLOG reads standard text files containing the names of all signals to be measured for a machine log, the physical device addresses and settings that are needed to measure those signals, and the format of the log sheet that normally is to be printed. NEWLOG then issues the CAMAC commands required for each signal measurement, may perform predefined operations on a signal or combination of signals, stores the signals in a database file, and normally prints a log sheet. OLDLOG extracts a previously measured machine log from the database file and prints a log sheet.

SEARCHLOG manages the machine-log database, a VAX keyed-record file, and extracts machine logs from the database according to a variety of criteria including log name, date, machine user, beamline used, beam energy, the value(s) of a specific signal or signals, and combinations of the above. SEARCHLOG interactively provides context-sensitive help, and attempts to protect the database against accidental missteps by the user.

Signal-tracking functions of the slow-channel monitor are supported in software by the private XSYS programs TRAKSET and TRAK. TRAKSET reads a text file containing the names of signals to be monitored periodically, desired limits on the values of the signals, the

number of a previously allocated XSYS data area in which to display the signals as functions of time, and an instruction directing that the experimenter be alerted if a signal value exceeds its limits. TRAKSET writes this information into a previously allocated XSYS data area in a format readable by the program TRAK. TRAK is run as a detached VAX subprocess, reads the XSYS data area prepared and maintained by TRAKSET, and implements the instructions found there, using an MBD channel reserved for use by the experimenter.

#### 2.1.3.2 NMR interface

In May of 1984, TUNL acquired a Scanditronix model *NMR 751* Gaussmeter/field lock, which replaced the Varian NMR previously used to stabilize the fields in the energy-analyzing-magnet system. The new system has a larger signal-to-noise ratio in the acquired NMR waveform and, primarily for this reason, regulates the fields with greater precision than was previously possible. Another advantage of the new system is that it can be interfaced to a computer, which can both monitor and control it.

The provisions built into the Scanditronix NMR for computer interfacing are extremely crude, consisting for the most part simply of wires connected to the front panel switches, and wires tapped directly from the electronics that control the front-panel display. To interface the NMR, then, the front panel was emulated in electronic hardware, and communication between that hardware, CAMAC, and the physical front panel was arranged.

Since computer control is not always desired, the front-panel emulation also can act as a transparent buffer for communication between the physical front panel and the NMR. A shared-access protocol is built into the interface so that computer and human users have simultaneous read access to the NMR, while write access is exchanged through a handshaking scheme in which the human user has priority.

The TUNL NMR/CAMAC INTERFACE comprises an array of buffers and registers on the NMR side which communicate via an internal data bus with a set of registers and buffers on the CAMAC side. The NMR-side registers emulate switches and display devices on the NMR's front panel and present data, from either the front panel or the computer, to the NMR. The CAMAC-side registers store instructions and data from the computer and, using timing signals generated by the NMR, select valid data for transmission to the computer.

There is one set of signals from the NMR interface that deserves special notice because of its use in acquisition of high-resolution scattering data. The eight lines that carry a digitization of the NMR error signal are updated continuously and presented to CAMAC whenever the NMR and interface are turned on and an NMR resonance is present--regardless of other data traffic through the interface, and regardless of any instructions to or settings of the devices. This error signal is a function of the difference between the NMR field

setting and the measured field in the upstream 90-90 analyzing magnet, and is used by XSYS event-analysis (EVAL) software to reject scattering events that occurred while the field was away from its set value.

Software support for the NMR interface consists of the private XSYS program XNMR ("private" because XNMR is inherently a laboratory-specific program, and because XNMR does not make use of the XSYS error-reporting facility) and a library of subroutines used in XNMR that can be linked to other programs.

XNMR is essentially a front end for the subroutine NMR which accepts commands and carries them out using the NMR interface. Also, XNMR implements a few commands, such as conversion of field to energy, that have nothing directly to do with the interface. The subroutine NMR translates commands (e.g., "SET FIELD") into sequences of binary instructions which control the flow of information through the interface, encodes command parameters to be sent to the Gaussmeter (e.g., the desired field value), and decodes numbers returned from it.

### 2.1.4 The TUNL automatic energy-stepping system

Thus far, discussion of uncontrolled variations in beam energy has centered on the task of maintaining discipline among the sometimes unruly devices with which an experimenter manipulates the beam. No complete list of unruly devices can fail to include the experimenter himself: his eyes that see "34" and somehow report "43"; his hands that painstakingly adjust the wrong dial to *precisely* the right setting --generally, the wandering focus of his attention.

That wandering focus is essential to an experimenter; it underlies his ability to discover and is a faculty that should not be blunted. But it is also inappropriate for the rote, repetitive tasks that are part of data acquisition; such tasks call for unswerving attention to detail so that the silly errors to which humans are prone can be avoided.

For acquisition of excitation-function data, one wants in addition the precision regularity characteristic of a machine: the analysis of excitation-function data is greatly simplified if those data are regularly spaced in energy. For these reasons and also to relieve the experimenter of much mindless drudgery, TUNL developed a system for automatically stepping the beam energy. Recent interfacing of the NMR Gaussmeter to the data-acquisition computer allowed implementation of the more capable stepping system described below.

The TUNL energy-stepping-system hardware is diagrammed in figure 2.5. The NMR Gaussmeter, as mentioned previously, is the

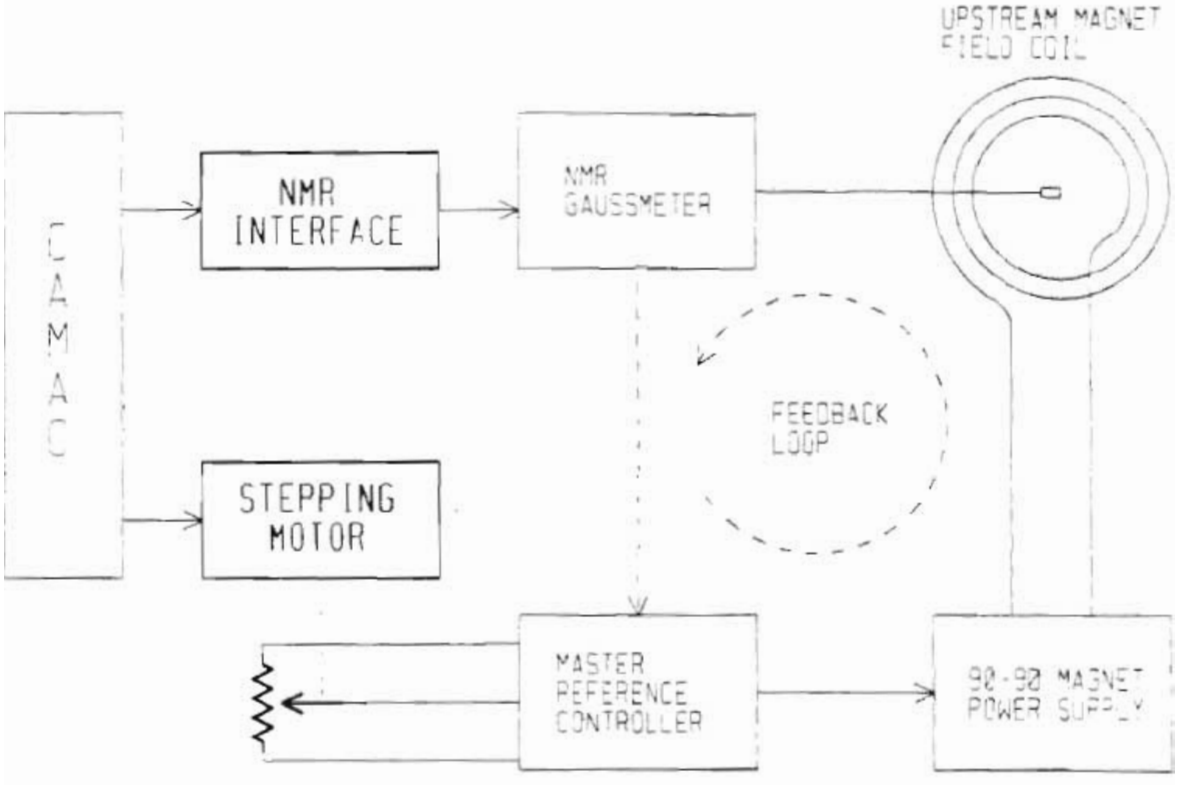


Figure 2.5 The TUNL energy stepping system.

TUNL high-resolution system's energy-calibration reference. The Gaussmeter compares the field of the upstream 90-90 magnet, which field is directly related to the beam energy, to a reference field setting. The Master Reference Proportional Controller, whose voltage output programs the 90-90 magnet power supply (and all other power supplies in the TUNL high resolution system) is in turn programmed by a variable resistor controlled by the data-acquisition computer. To make an energy change, the Gaussmeter's reference field setting is changed, and the Master-Reference programming resistance is varied until the measured 90-90-magnet field agrees with the new field setting. Once the energy change has been completed, the Master-Reference programming resistance is fixed and the Gaussmeter is allowed to modulate the Master Reference about its new setting to maintain a constant field in the 90-90 magnet.

The Master-Reference programming resistor is a precision 20-turn helipot which the data-acquisition computer controls by means of a stepping motor. The motor turns the helipot armature through a gear box so that the motor's coarse step size does not limit its ability to set the armature position. The remaining system hardware, the NMR interface, is described in section 2.1.3.2.

As might be expected, the energy-stepping-system software overlaps considerably with the NMR-interface software described in section 2.1.3.2; also there is overlap with the HIRES system of data-acquisition programs. Specific to the energy-stepping system are the

NMR-interface subroutines GOTO.FOR and FINESET.FOR, and the HIRES programs ESTEP.COM and BSTEP.COM.

ESTEP.COM reads the NMR Gaussmeter, determines the current beam energy, calculates a new energy, and invokes the program NMR to set the Master Reference Controller and the Gaussmeter's reference field in agreement with that energy. BSTEP.COM is an alternative to ESTEP.COM and performs nearly the same task, but does not read the NMR to determine the current field. Instead, BSTEP.COM reads the current field value stored in a VAX global symbol. Because of this, small errors (of a few $\mu$T--which typically translates into a few tens of eV) inevitable in reading from and writing to the Gaussmeter do not accumulate from one energy step to the next when BSTEP.COM is used.

### 2.1.5 Target voltage ramp

#### 2.1.5.1 Motivation

In acquiring excitation-function data, the usual method of stepping the beam energy is to vary the setting of the energy-analyzing magnet. An alternative method, applicable if the beam is charged, is to apply a varying voltage to the target, leaving the analyzing-magnet setting fixed. Both methods have advantages: the former has unlimited range and requires little or no additional hardware; the latter has great precision and flexibility.

In varying the analyzing-magnet setting by the tiny amount appropriate for a single step of an excitation function, one makes a small change in a relatively very large quantity. Also, one contends with hysteresis in the analyzing magnet, and the self-inductance that magnet represents to its power supply. For these reasons alone, an alternative means of stepping energy is desirable. But further, contending with hysteresis, in practice, means requiring that data points be acquired in order of increasing or decreasing energy only; as we shall see, this leaves the data vulnerable to systematic errors that cannot practically be corrected.

In contrast, varying the target voltage by the amount required for an excitation function is relatively easy to do precisely and accurately, since only a marginal change in beam energy is needed. Also, since a voltage can be varied quickly and with essentially no

hysteresis, data points can be acquired in any desired order.

In particular, an energy region can be scanned many times, while data are being acquired, by applying a periodic staircase-ramp waveform to the target. (See fig. 2.6. Actually, a staircase-*triangle* wave is used; "ramp" is a misnomer which persists for historical reasons.) I'll call an excitation function acquired in this way a "ramp excitation", and one acquired by stepping once through an energy region (e.g., by stepping the analyzing-magnet current) a "step excitation." The effects of energy deviations--time-dependent differences between the actual beam energy and the energy inferred from settings of the analyzing magnet and/or voltage ramp--on the two types of data are different.

While there is a continuum of possible energy deviations, it is useful for discussion of their effects to represent all deviations as combinations of four idealized types:

1) energy drift--a slowly and constantly changing deviation.
2) energy shift--an instantaneous and lasting deviation.
3) slow-random deviations--an accumulation of many drifts and shifts which occur over a time that is comparable to the time during which an excitation function is acquired.
4) fast-random deviations--an accumulation of many drifts and shifts which occur over a time that is short compared with the time required to collect an excitation function.

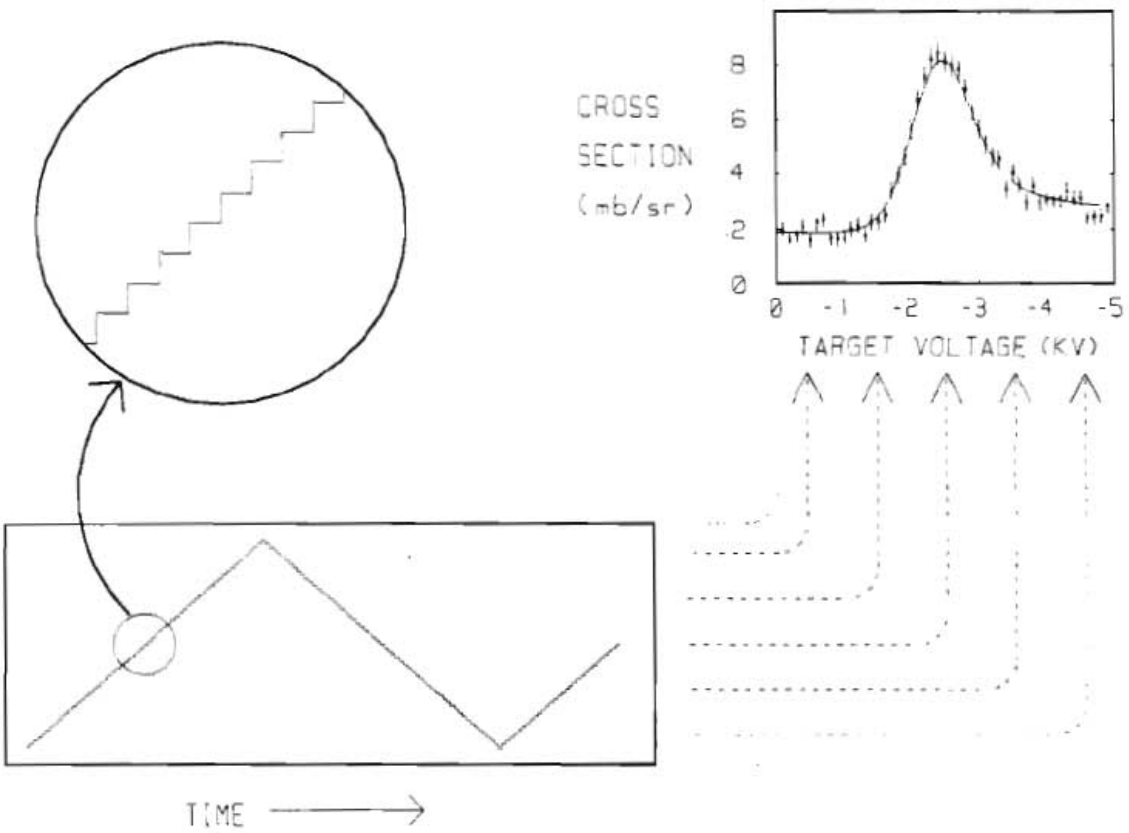


Figure 2.6 The target-ramp voltage and a ramp-excitation function.

The effects of energy drift and of fast-random energy deviations can, in principle, be removed from step-excitation data by deconvolution with an appropriately chosen kernel. If neither of the other two types of energy deviations occurred while the data were being collected, the appropriate kernel is the beam resolution function.

In contrast, the effects of energy shifts and of slow-random energy deviations are normally impossible to remove from step-excitation data. An energy shift, for example, that occurs during acquisition of a step excitation, causes an energy region to be skipped or scanned twice (see fig. 2.7); if the latter, the data are in principle correctible, but only with exact knowledge of the extent and timing of the shift.

On ramp-excitation data, however, all four types of energy deviation produce artifacts that are removable in principle by deconvolution, unless those deviations are correlated in time with the voltage ramp. This is so to the extent that all data points of a ramp excitation are affected equally by the deviations. In practice, such removal requires at minimum a measurement of the beam-energy distribution under conditions that accurately sample those under which the afflicted data were acquired--that is, it requires knowledge of the beam resolution function. If no correlated energy deviations occurred while the data were being collected, the deconvolution kernel is simply the beam resolution function.

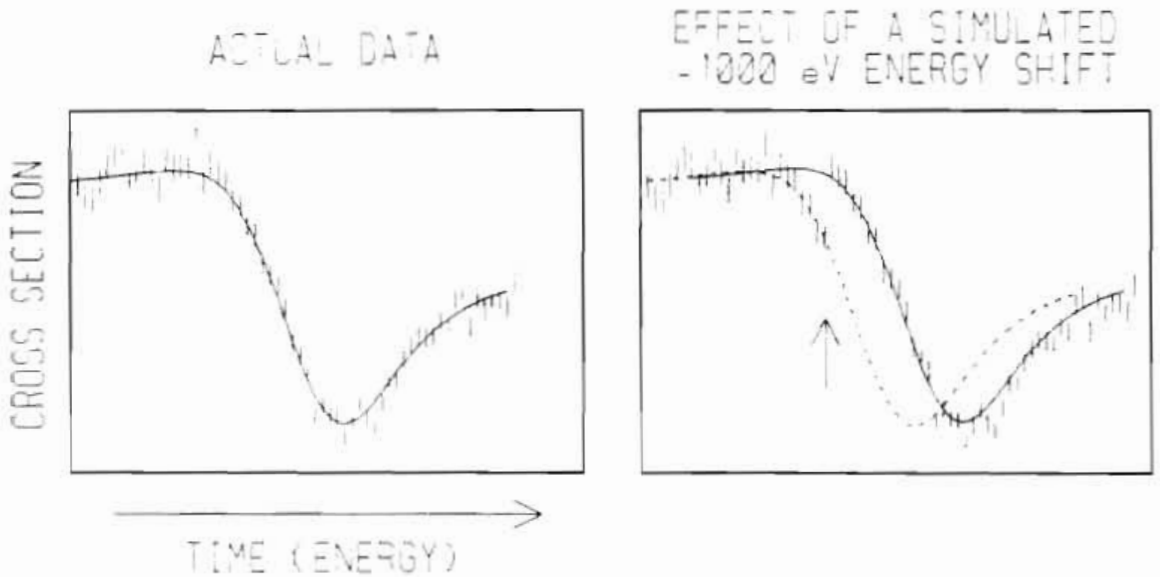


Figure 2.7 An excitation function resulting from a simulated energy shift.

Time-dependent errors in normalization--for example, errors in beam integration--also typically affect ramp-excitation data in a much more uniform way than they affect step-excitation data. In both, the errors produce artifacts that are correctible by renormalization; but while afflicted step excitations must be renormalized point-by-point, which requires exact knowledge of the extent and timing of the errors, ramp excitations require only an overall normalization since all points are affected equally. If the errors average to zero over the course of a ramp excitation, no correction at all is needed. (Once again, errors that are correlated in time with the ramp are not easily corrected: such errors affect ramp-excitation data the way all time dependent errors affect step-excitation data.)

#### 2.1.5.2 Implementation

##### 2.1.5.2.1 Chamber configuration

The scattering chamber used for high-resolution data acquisition was designed for application of high voltage to the target: the target rod is isolated from the rest of the chamber, which is grounded. The only change required in chamber configuration to accommodate the high voltage was a beefing up of the existing electron suppression, applied to detectors and the Faraday cup, to handle higher-energy electrons. A strong magnet was placed on top of the chamber and downstream from the target rod to divert electrons from the Faraday cup, and existing magnets in front of the detectors were replaced with stronger ones.

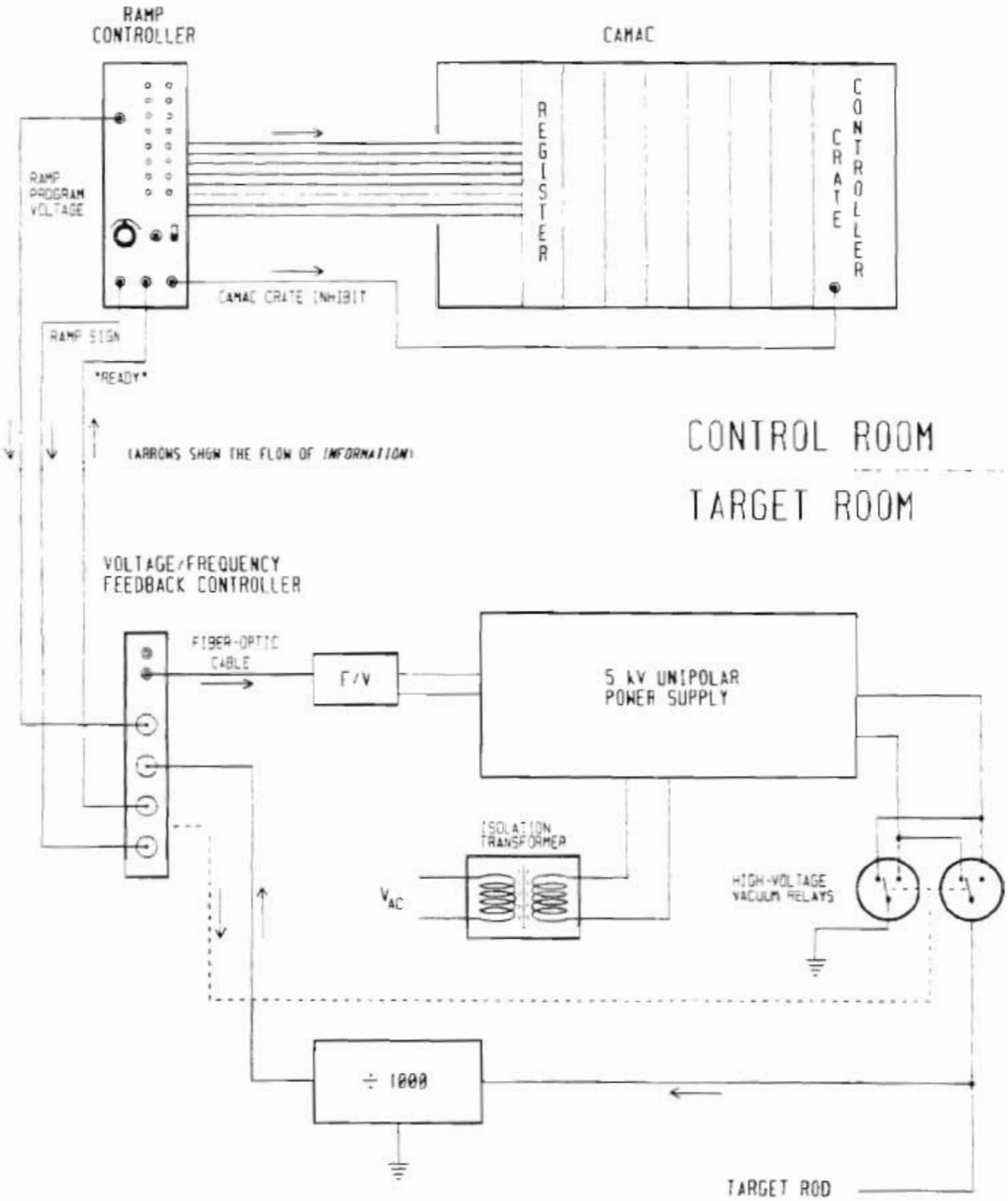


Figure 2.8 The target-ramping system.

#### 2.1.5.2.2 Overview

The target-ramping system (see fig. 2.8) is built around a Kepco 5-kV, unipolar, programmable power supply. The supply responds quickly enough to changes in programming voltage that stepping frequencies in the 100 Hz range are practical, allowing a complete sweep of 128 steps over an energy region in about one second. Unfortunately, the 5 kV voltage range--which translates, for protons, into a 5 keV range of beam energy--is insufficient for our purpose.

We therefore configured the ramping system to produce a bipolar output by powering the unipolar supply through an isolation transformer and switching its output leads with a pair of high-voltage vacuum relays. Depending on the state of the relays, the supply is grounded and drives the target negative, or the supply floats, driving itself and the target positive. Since the supply's programming voltage is referenced to the (floating) chassis ground, programming information is delivered through a fiber-optic cable. Since the supply's load is not constant, that programming information derives in part from voltage feedback.

#### 2.1.5.2.3 Ramp generator and CAMAC interface

The Digital Ramp Controller is a NIM module located in the control room that generates programming and control signals for the ramp system, and sends the ramp-step number to CAMAC for use by an XSYS event-analysis (EVAL) program. Front-panel selection of the ramp amplitude and frequency, of the number of ramp steps, and of

unipolar or bipolar operation is possible. The Controller comprises an up/down counter, a digital-to-analog converter (DAC), an arithmetic logic unit (ALU), and some control electronics.

The counter generates an eight-bit digital representation of the unipolar staircase-ramp waveform which is to program the 5 kV supply. The output of the counter is converted to an analog voltage and sent to the target-room electronics. If bipolar operation is selected, a sign bit is generated and also sent.

When the ramp system is operating in unipolar mode, the ALU simply passes the number generated by the counter to CAMAC. In bipolar mode, the number is combined with the sign bit into an offset-binary number proportional to the desired target voltage, and that number is sent to CAMAC. Thus, the same EVAL program can be used without modification for both unipolar and bipolar operation, and no data-sorting time is spent to perform the numerical conversion.

In bipolar mode, the Controller halts the counter and raises the CAMAC crate inhibit each time the sign bit changes state so that data are not acquired while the relays are switching. (Normally after switching, relays continue to bounce for a few tens of milliseconds.) The wait state persists until the target-room electronics responds to the change of state with a "ready" signal.

#### 2.1.5.2.4 Ramp Voltage-to-Frequency Controller

The remainder of the ramp-system electronics is located in the target room. The Voltage-to-Frequency (V/F) Controller accepts a unipolar ramp-programming voltage and a sign bit from the Ramp Controller and supervises the generation of the target voltage.

The programming voltage is converted to a frequency in the range [1 ... 500] kHz and sent over fiber-optic cable to a frequency-to-voltage converter which directly programs the Kepco 5 kV supply. The sign bit drives high-voltage relays as described above. The relay-switched supply output, a bipolar staircase-ramp waveform with a nominally 10-kV swing, is applied to the target rod and to a 1000:1 voltage divider. The divider output is sent to the V/F Controller which rectifies it, using the sign bit and a set of low-voltage relays, compares it to the programming voltage, and adjusts the frequency to null any difference.

In retrospect, the decision to use voltage/frequency conversion, rather than, say, an analog fiber-optic link or a parallel, digital fiber-optic link, to send programming information to the voltage supply was a mistake. The problem is not with the conversion itself, but that it occurs in a feedback loop, where an unavoidable side effect of v/f conversion, the voltage-dependent time delay, is an unwelcome complication.

### 2.1.6 Beam resolution function measurement

#### 2.1.6.1 Motivation

Thorough analysis of excitation-function data requires knowledge of the energy resolution function of the instrument used to acquire those data. For the high-energy-resolution experiments described in this thesis, the function is the convolution of two contributions: the target resolution function, which describes the effects of energy loss incurred by the beam while traversing the target foil; and the beam resolution function, the energy distribution of the beam evaluated at a point just upstream of the target.

In the analysis of high-resolution data for this thesis, all objectives could be met with knowledge of the total resolution function only; the beam and target contributions are not individually useful. However, we found no reliable way of measuring the total resolution function and so have attempted to measure the beam resolution function separately. (The target resolution function is discussed in section 4.5.)

#### 2.1.6.2 Previous work

A beam-resolution measurement apparatus used previously at TUNL [Wil82] is shown in figure 2.9. The measurement principle this apparatus exploits is that the energy selectivity of an energy-dispersive magnet system can be increased by narrowing the object- and image-slit openings. Beam passing through the object slit is

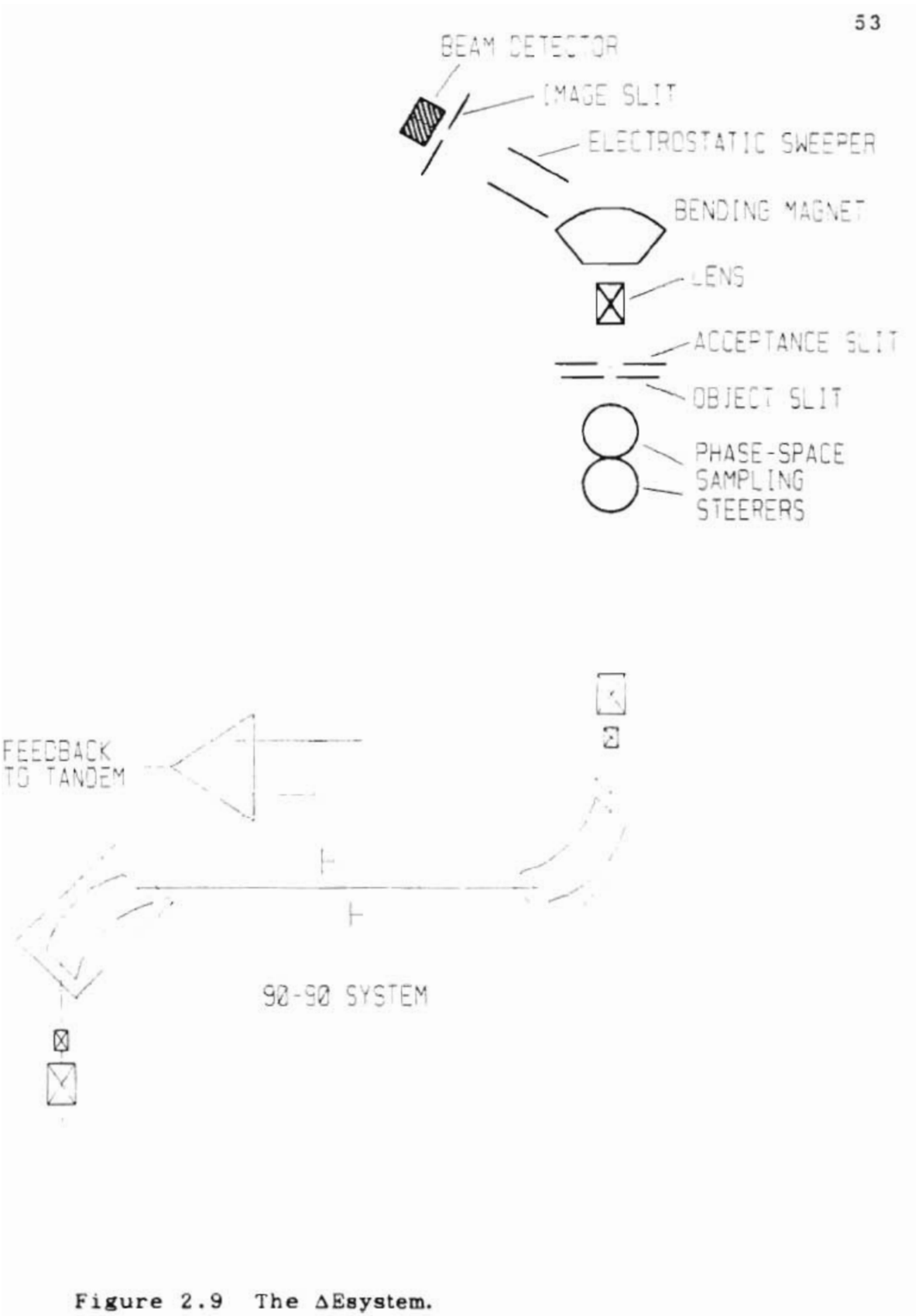


**Figure 2.9 The ΔEsystem.**

energy dispersed by the magnet/lens system into a continuum of images of that slit focussed on the plane containing the image slit. The beam-intensity distribution in this continuum, as a function of position, is presumed to represent the beam-intensity distribution as a function of energy. The distribution is measured by sweeping it past the image slit with an electrostatic steerer and counting the beam particles that pass through the slit. The system's energy calibration is contained in the term $\Delta E/\Delta V$, where E is the centroid energy of the beam transmitted through the image slit when a voltage V is applied to the steerer plates. (Thus, the apparatus is referred to as the "$\Delta E$ system.") $\Delta E/\Delta V$ is presumed a constant function of V.

Since the object-slit opening, when narrowed sufficiently to allow a meaningful measurement of beam energy, cannot accommodate the entire phase space of the beam incident on it, a pair of steerers upstream from the slit is used to sample that phase space. Also, since beam position at the image slit is correlated with the angle of incidence at the object slit (an unwanted correlation whose effects can contribute noise to the measurement), an acceptance slit is used to limit that angle.

The system has a few practical problems. It is extremely difficult to steer the beam through the object and acceptance slits and then adjust its intensity so that the measurement can be made: "usually, several hours of tuning the system were required..." [Wil82]. It is certainly possible that a beam tune optimized for resolution-

function measurement by this apparatus results in a different beam resolution than a tune optimized for data acquisition.

There is a more fundamental problem as well. The underlying principle of the ΔE system (narrowed slit openings produce greater energy selectivity) is valid only if (1) focussing errors and beam-optical aberrations of the system of lenses that produces a 10-μm-wide image of the 13-μm-wide object slit are negligible, and (2) the magnification of the magnet/lens system is equal to the ratio of image- and object- slit widths. Since that focussing is directed by beam-optics calculations (the program TRANSPORT [Bro70]) valid only to second order and carried out by devices that weren't designed for this fantastic accuracy, the question of whether errors are negligible is a real one. Moreover, there is no practical way of verifying the quality of the focus because a focussing/magnification error or aberration produces the same observable effect that some beam-energy distribution of nonzero width would produce with perfect beam optics.

One source of our difficulty in measuring the beam resolution produced by the TUNL high-resolution system is simple and fundamental: we are already using the most sensitive, most accurate, and most precise energy-measurement device available to us--the 90-90 magnet system--to *produce* the beam-energy distribution we would like to measure.

However, since the 90-90 system is composed of two nearly

identical magnets, it is conceivable to use the downstream magnet to measure the energy distribution produced by the upstream magnet. Immediately, this possibility raises the question of whether the upstream magnet by itself produces a sufficiently narrow beam-energy distribution that the downstream magnet can be sacrificed into use as a measuring device. Experimental data indicate that the answer is a qualified "yes."

A test designed to answer this question was made by J. Wilkerson and is summarized in the following excerpt from [Wil82]: "Excitation functions over a narrow [FWHM: 50 eV] resonance in $^{50}Cr(p,p)^{50}Cr$ ... were measured [using a 1.4 μA beam of unpolarized, gas-stripped, 3.93 MeV protons] with slit control at the center slits and the output slits, with no statistically significant difference in the observed resolution between the measurements." (See fig. 2.1 for slit locations. The slit widths were not specified, undoubtedly indicating that they were set to standard high-resolution specifications: 1 mm for the center-slit opening, and 2 mm for the output-slit opening.)

Since the center- and output-slit widths were the same in both measurements, this result can mean one of two things: 1) the slit feedback system produces no improvement in beam resolution and the location from which feedback control derives is therefore irrelevant; or 2) the slit feedback system *does* improve the beam resolution and the upstream magnet with its image slit produces enough information to exploit fully the capability of the system. Interpretation (1) is

difficult to reconcile with the fact that the total resolution function extracted from analysis of the resonance data is consistent with 460 eV FWHM, whereas the beam resolution alone expected from the 90-90 system unassisted by slit feedback is 680 eV FWHM (3.93 MeV / 5800) at this energy. Interpretation (2) gains credence from the fact that, with feedback control derived from the center slit, narrowing that slit opening by a factor of two produced no perceptible difference in the observed resolution.

Thus, with an intense, low-energy, unpolarized, gas-stripped beam of protons under feedback control, the downstream 90-90 magnet has produced little or possibly no improvement in beam resolution and might therefore be used for other purposes, such as for measuring the beam resolution function. One naturally wants to know how well this proof-of-principle result holds up under other circumstances. Since the result depends on beam-resolution improvement by the fast-feedback system, it holds up or doesn't depending strongly on how well the tandem behaves under those circumstances. Certainly at much higher beam energies (larger tandem fluctuations) or much lower beam intensities (poorer feedback information), the sacrifice of the downstream 90-90 magnet will be felt more keenly. Somewhat less certainly, the beam energy spread obtained with the upstream magnet acting alone will not be more than a factor of two worse than what could have been obtained with both magnets acting together.

For the purpose here, to answer the question more precisely

would be to argue irrelevantly because the criterion with which the answer compares is known even less well. Given that sacrificing the downstream magnet results in poorer--but not disastrously poorer--beam resolution, the relevant question is "How does this loss compare to what is gained with approximate knowledge of the beam resolution function?" Since what is gained depends in large part on how well the function is known, we turn to discussion of the measurement apparatus.

#### 2.1.6.3 Analyzing-magnet current ramp

In a new system for measuring the beam resolution function (see fig. 2.10), the downstream 90-90 magnet samples the energy distribution produced by the upstream magnet, passing beam with a small range of energies on to the scattering chamber for analysis. Each of, typically, sixteen samples is characterized, by acquiring excitation-function data with it, according to its intensity and centroid energy relative to the other samples. From this information, a plot of beam intensity versus beam energy is generated.

With the field in the upstream 90-90 magnet held fixed by feedback from the NMR Gaussmeter, and slit-feedback control of the tandem derived from the center 90-90 slit, the beam is steered into the scattering chamber and focussed on target as for normal data acquisition. A narrow resonance is located and centered within the energy range of the target-voltage ramp, and the data-acquisition system is set up for collection of a ramp-excitation function.

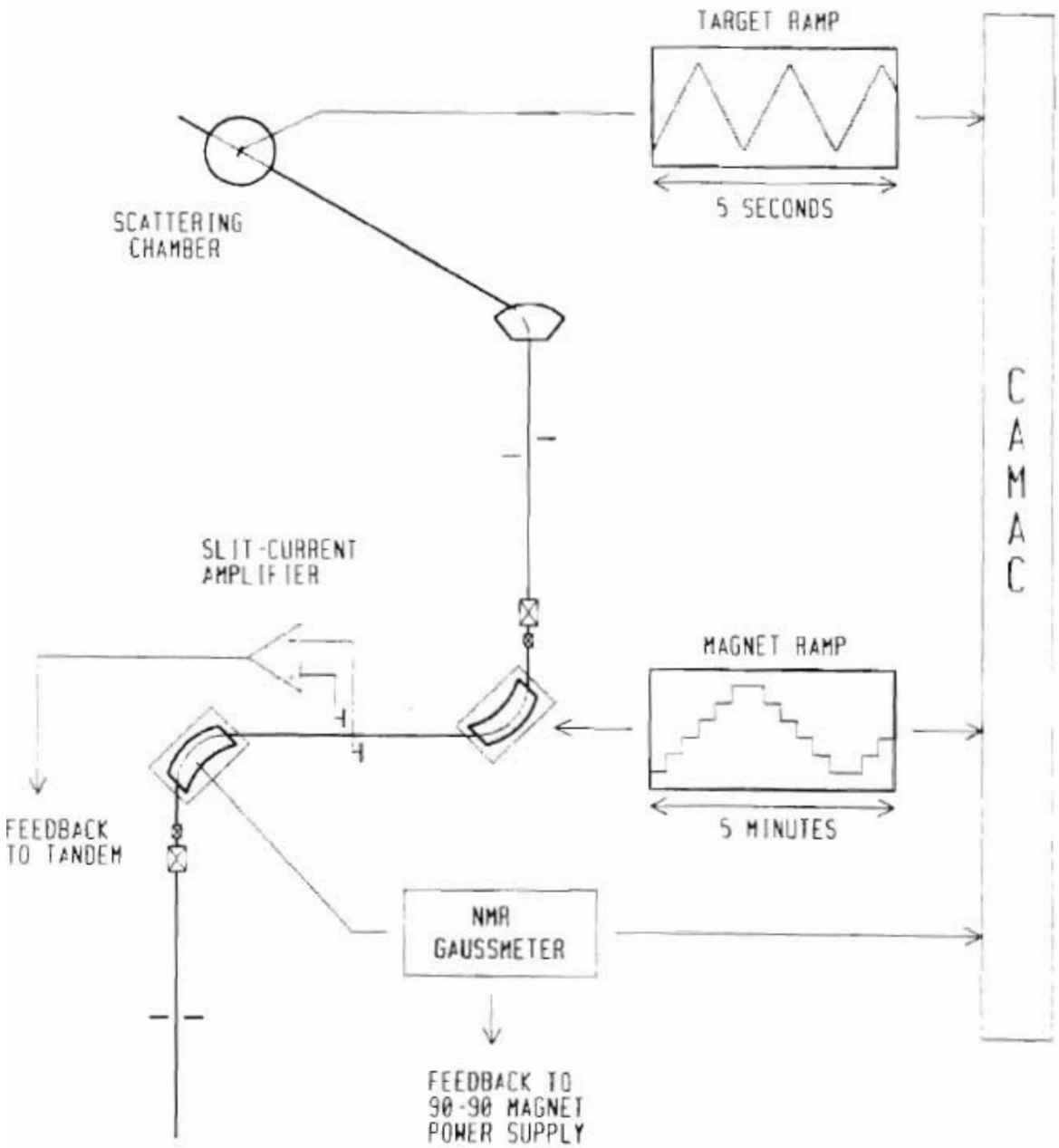


**Figure 2.10** The ramp-ramp system for measuring beam resolution.

The downstream 90-90 magnet's output-slit opening is then narrowed to increase the energy selectivity of the magnet/slit combination, and the field in the magnet is varied in steps so that beam samples from the entire energy range of the distribution to be measured are transmitted through the slit to target. In actual practice, the field is stepped up and down many times through the same set of values until statistically meaningful data have been acquired. (The stepping process is very similar to the target-voltage ramping that is taking place simultaneously, but at a higher ramp frequency, in the target chamber. The resulting data is called a "ramp-ramp excitation," and the method the "ramp-ramp measurement" for this reason.)

For each field setting of the downstream magnet, the intensity of the beam on target is measured. Only a relative measurement is needed since the end result is to be a probability density (whose overall normalization is fixed by the requirement that its integral be unity). Consequently, any convenient measure of beam intensity that is independent of beam energy can be used; a typical measure is the number of counts in the elastic-scattering peak of a target contaminant whose cross section is known to be locally energy independent.

The relative centroid beam energy for each field setting is determined from the location of the resonance in the excitation function collected using the target-voltage ramp (see fig. 2.11). Note that this determination is completely independent of the field setting of the downstream magnet; although one expects the centroid beam energy to

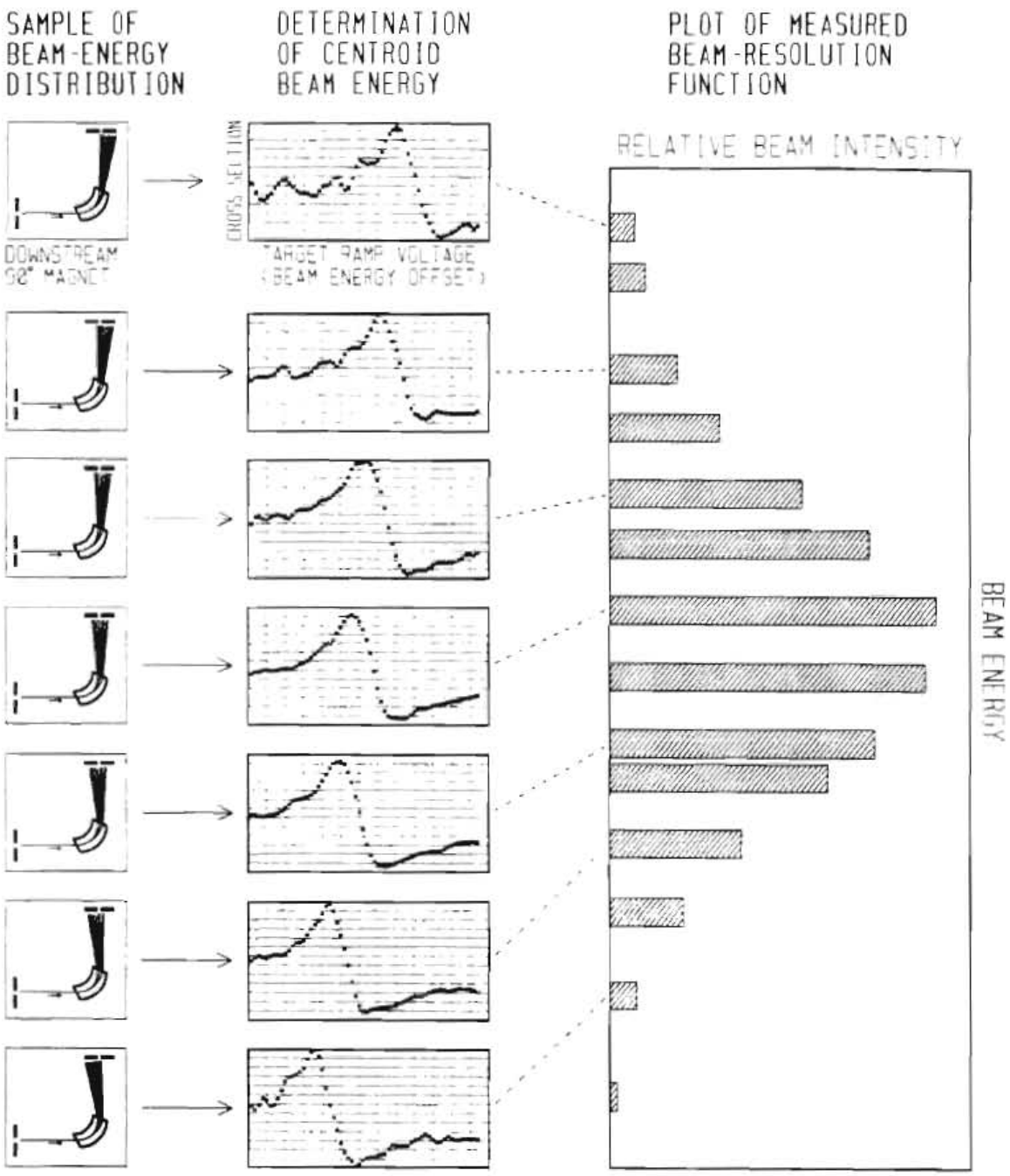


Figure 2.11 Schematic analysis of beam-resolution-function data.

vary approximately linearly with that field setting, the measurement must not depend on this because behind the expectation are implied assumptions about the beam-energy distribution being measured.

2.1.6.4 Parameters affecting the measurement, practical compromises

The width of the resonance used to measure differences in centroid beam energy is, in principle at least, of little importance. In particular, the resonance need not be narrower than the presumed width of the beam resolution function to be measured. All that is required of the resonance is that its location in the target-ramp excitation be accurately measurable; this requirement argues as strongly for a high count rate and a large resonance effect (to minimize statistical uncertainty) as for narrowness.

The length of time taken to acquire beam-resolution-function data ideally should be the same as that taken to acquire the resonance data for which a resolution function is desired. This helps to ensure that any slow drifts in energy that might occur during resonance-data acquisition are represented also in the resolution-function data. However, accelerator time is precious and one is naturally (and correctly, I believe) inclined to compromise in favor of the resonance data.

The degree to which the downstream magnet's image-slit opening is narrowed for the measurement is another subject for compromise. With other factors equal, narrower would be better since a narrow slit clearly produces a less energy-averaged result (about which more later)

than a wide slit. But a narrower slit passes less beam, and the resulting lower count rate may render determination of the resonance location less precise (through increased statistical uncertainty in the excitation-function data), or increase the time required to make a beam-resolution-function measurement.

The energy-averaged result produced by an image slit whose opening is not infinitesimally narrow can be seen (in an approximation discussed later) as a convolution of the true beam resolution function with the transparency function (refer to fig. 2.3b in sec. 2.1.1) of the magnet/slit combination. Thus, the instrument used to measure the beam resolution function has, in turn, a resolution function of its own. To avoid ambiguity in what follows, this resolution function will henceforth be referred to as the *instrument function*.

It should be clear that the width of the instrument function, for the ramp-ramp measurement, depends on the position-to-energy correlation that exists *within the image slit only*, and on the transparency function that describes the slit's effect. (Consequently, the instrument function can differ from one field setting to another; to the extent that it does, it is not a true resolution function because convolution is not the appropriate mathematical tool with which to model its effect. I believe the extent to be small and, in any case, will ignore this fine point in what follows.)

This much the ramp-ramp measurement system has in common

with the ΔE measurement discussed above (and, arguably, with any other practical measurement scheme): the instrument function is not generally ignorable. There are significant differences between the two methods, however, in the sensitivity of the instrument function to imperfections of the instrument. In the ΔE method, the instrument-function width (and, through it, the observed width of the beam resolution function) increases without limit as focussing errors increase because the energy scale for the measurement derives completely from the position-to-energy correlation at the image slit. In the ramp-ramp method, since the energy scale is determined independently, the position-to-energy correlation serves only to sample the beam-energy distribution. Consequently, the net effects of a focussing error are that less beam is transmitted through the image slit, and that a larger change in the downstream magnet's field is required to swing the beam completely across the slit.

There is another difference. In the ramp-ramp method, the instrument-function width decreases as the image-slit width decreases, regardless of focussing errors, to a lower limit imposed solely by the quality of the position-to-energy correlation within the slit. In the ΔE method, as already mentioned, the instrument-function width does not necessarily decrease as slit widths decrease.

It should be emphasized that the ramp-ramp method is a means of measuring the beam resolution *at the center 90-90 slit*. Obviously, one would prefer that the measurement be a indication of the beam

resolution at the *target*. Under certain circumstances, this seems possible.

If the measured beam resolution at the center 90-90 slit is already better (by virtue of active slit-feedback control) than one would expect from the full, passive, magnet/slit system, one has good reason to expect this center-slit measurement to be a good indication of the resolution at the target. The remainder of the analyzing system can hardly be expected to improve the beam resolution in such a case and, barring slit scattering, there is no way in which the system can possibly worsen the beam resolution. However, if the measured beam resolution at the center 90-90 slit is poorer than one would expect from the passive magnet/slit system, there is little doubt that the beam resolution at the target will be better, perhaps by as much as a factor of two, than the center-slit measurement indicates.

2.1.6.5 Implementation

In addition to the target-voltage-ramp hardware described elsewhere, three pieces of electronic hardware are used for the beam resolution measurement: a digital ramp controller, which directs the variation of the downstream 90-90 magnet's field; a digital-to-analog converter (DAC) with optically isolated inputs, which is the interface between the ramp controller and the downstream magnet trim supply; and a set of digital opto-isolators that interface the ramp controller to the "parameter-bit" inputs of one of the data-acquisition ADC's. Together, this hardware constitutes the "ramp-ramp system" (fig. 2.12).

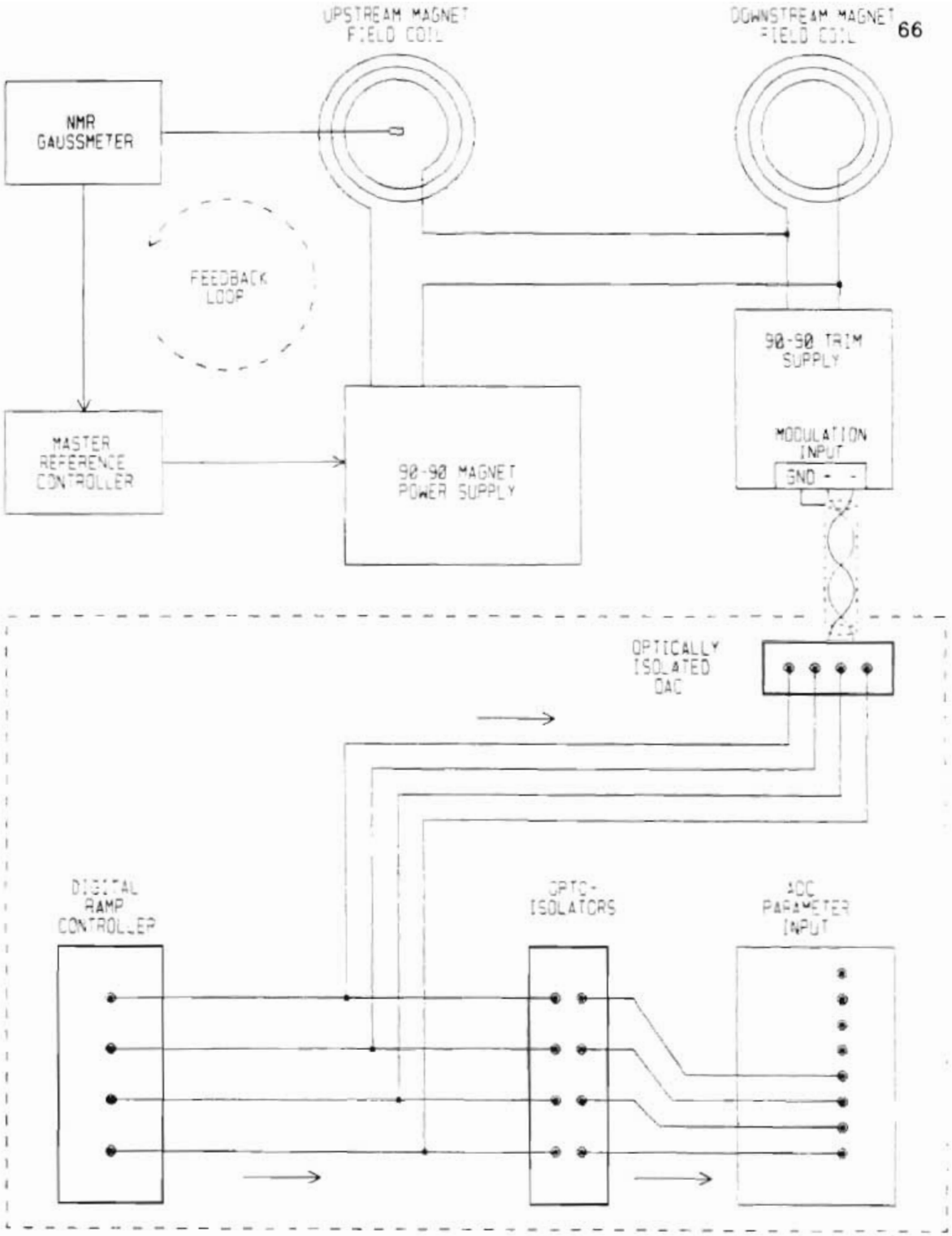


Figure 2.12 The ramp-ramp system hardware.

Note that both upstream and downstream magnets in fig. 2.12 are powered from the same supply. Independent variation of the field in the downstream magnet can be accomplished, nevertheless, by varying the setting of a trim supply that acts as a load electrically in parallel with the downstream magnet's field coil. If the field of the upstream is not stabilized, it will also vary with the trim supply; for this reason, it is imperative that NMR feedback from the upstream magnet to the 90-90 supply be maintained throughout the measurement.

The digital ramp controller is similar to the ramp controller used in the target-voltage-ramp system. (In fact, it *was* the ramp controller of an early, unipolar-only version of that system.) As used here, the circuit is simply a four-bit, up/down counter. The clock that drives the counter allows adjustment of the ramp-step period in the range [1 ... 30] seconds.

The optically isolated DAC is a very simple circuit (see fig. 2.13) in which four digital opto-isolators are followed by an R-2R ladder DAC, in turn followed by an operational amplifier. The circuit is battery powered and, once connected to the modulation input of the trim supply, imposes a negligible load on that supply. This is important because the trim supply floats on the output of the main 90-90 magnet supply; any load--any D.C. or A.C. path to ground through the DAC--would disturb the 90-90 system energy calibration, possibly throwing the system out of the field lock established by feedback from the NMR Gaussmeter.

It should be clear from earlier discussion that the accuracy (e.g., the linearity) of the DAC is not an issue in the measurement scheme, although its precision *is*. By far the most significant source of imprecision is variation of the supply voltage as the batteries run down, which is minimized but not completely removed by voltage regulators in the DAC circuitry. In our use of the DAC, batteries were changed daily.

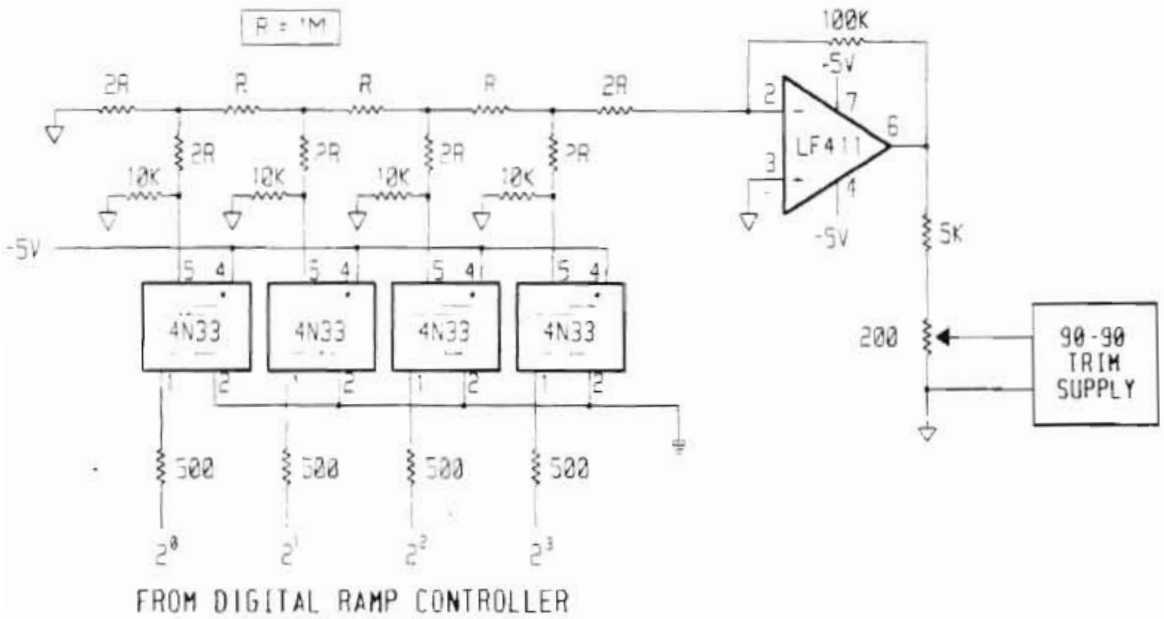


Figure 2.13 The optically isolated digital-to-analog converter used in the ramp-ramp system.

## 2.2 Ion-implanted targets

### 2.2.1 Motivation

There are many means of confining a gas for use as a target in a nuclear-scattering experiment. The most common, a thin-walled gas cell, is inappropriate for high-energy-resolution scattering since energy straggling experienced by the beam in traversing the cell wall results in an unacceptably wide beam-energy distribution. Means of confinement that are appropriate for high-resolution scattering, such as windowless, differentially pumped gas cells; gas jets; and cryogenic targets generally require a substantial investment of time and money, and involve extensive modification of the scattering chamber. If one intends to apply a high voltage to the target as we did (see discussion of the target voltage ramp in section 2.1.5) the engineering problem becomes more complicated since the target must be electrically isolated from ground, and electrical conduction by the gas cannot be ignored.

For many gaseous elements, a solid target can be made by evaporating a compound containing the element onto a thin backing foil. Unfortunately, the gas in which we are interested, neon, does not form a stable compound under any circumstances of which we are aware.

Ion-implantation of a gas into a thin foil is an attractive alternative method of producing a target suitable for high-resolution scattering. Such a target is as easily handled and stored as a solid-foil

target, and its use requires no modification to a scattering chamber intended for conventional solid-foil targets. Another advantage of target making by ion-implantation is that chemically and isotopically pure gas is not required since implanters generally do a good job of isotope separation.

### 2.2.2 General Remarks

An implanted target, to be useful in high-resolution nuclear-scattering experiments, should have a high concentration of the implant very near to (ideally, in our case, within a few hundred Angstroms of) the surface, and a very low concentration everywhere else. Equally important, the areal number density of implanted ions should be large enough that scattering data can be acquired reasonably quickly from the target with the available beam current. (In our case, a reasonable areal number density of $^{20}Ne$ ions is greater than about $3 \times 10^{16}$ ions/cm$^2$ --approximately equivalent to 1 $\mu$g/cm$^2$ $^{20}Ne$.) These criteria, which together seek to minimize energy straggling in the target while maximizing the scattering yield from it, describe in gross terms the desired implant-depth distribution, the number density of implanted ions as a function of distance into the target.

There is a third criterion: the depth distribution should be accurately measurable or calculable since knowledge of it is required to calculate the energy-resolution function for the scattering process. As we'll see, the first two criteria are in conflict with the third; the third will lose that conflict.

The depth distribution of $^{20}Ne$ ions implanted into a substrate can be controlled, to some extent, by varying the following implant conditions: the ion energy, the substrate species and structure, and the areal number density of incident ions--the "implant dose". (Note that "dose" does not imply "accepted dose": incident ions do not necessarily stop in the substrate, nor, if they stop, do they necessarily remain there.) One wants to know the details of these dependences, whether and how their effects are interrelated, and most importantly, what choices are practical, in order to produce the best possible target by implantation.

The choice of substrate species is sharply limited by practical considerations some of which have nothing to do with ion implantation. The substrate is to be the major contaminant in a nuclear-scattering target; scattering from it must not obscure scattering from the implant. This virtually eliminates elements of high atomic number from consideration since scattering from them can populate a large number of low-lying nuclear excited states; for the same reason, it argues against compounds and against elements that are not at least nearly monoisotopic. The substrate must be formable into thin, strong foils (possibly by evaporation onto a carbon foil) and it must not sublime under heating in vacuum.

Nuclear-scattering-kinematics calculations were performed using the program RKIN for the small number of elements that satisfied the above criteria, to verify their suitability as contaminants. Carbon,

aluminum, and beryllium were final substrate candidates; beryllium was rejected because it is poisonous.

The remaining implant conditions, energy and dose, have effects that are not independent as they pertain to our target criteria. Briefly, although target thickness increases generally with implant dose, for a given implant energy there is a maximum achievable target thickness, called the *saturation thickness* [Bur83]. This result is expected from the patent inability of any substrate to accept an arbitrary number of implanted ions, but the saturation thickness can be reached at lower implant doses than this simple observation would imply.

The saturation thickness is an equilibrium effect. As ions are implanted into a substrate, substrate atoms and previously implanted atoms are knocked out by the inevitable ion-atom collisions. The process is called *sputtering*, and results in a gradual erosion of the substrate surface. As the implant dose increases, the density of implanted atoms near the substrate surface grows; so grows the rate at which implanted atoms are sputtered away. Eventually, this rate equals the rate at which new ions are implanted. The dose at which this equality is reached is called the "saturation dose", and beyond it, the implant distribution is (ostensibly, at least) independent of dose.

This is an important result for us because it facilitates a simple restatement of our first two target criteria in terms of implant

conditions. Since one knows from the start that a higher implant energy implies a deeper implant, and that sputtering preferentially removes atoms near the substrate surface, a higher implant energy also implies a greater saturation thickness. The target criteria, then, are satisfied generally by implanting to saturation at an energy that yields an acceptable target thickness.

The saturation target thickness W[g/cm$^2$] is given approximately by the following formula [Bur83]:

$$W = \frac{M \rho R(E)}{m\,[S(E) + 1]} ,$$

where R[cm] is the projected range (see below) of the implanted ions of energy E in the substrate; m and M are the masses of the implant and substrate ions, respectively; $\rho$[g/cm$^3$] is the substrate density; and S is the sputtering yield, the number of substrate atoms sputtered per implant ion of energy E. For many ion/substrate combinations, R can be found tabulated in a reference such as [Gib75]. For noble gas implant ions in a wide variety of substrates, S can be found plotted in [Alm61].

This formula is useful for discovering the range of values of the implant energy in which to search for optimal implant conditions; with our target criteria, the indicated range is [10 ... 20] keV. (This is a relatively low implant-energy range, wholly below the range of most implanters. Also, saturation doses in this energy range are relatively high, a factor of ten or so higher than doses typically used in

semiconductor processing.) To choose within these energy limits, more detailed information about the implant-depth distribution than simply its first moment, the projected range R, is needed--especially in view of the fact that R does not include the effect of sputtering on the distribution.

### 2.2.3 Modelling the implant distribution

There is no formula or heuristic that can accurately predict the depth distribution of an arbitrary implant. This is especially true of the high-dose, low-energy implantation which yields a useful high-resolution scattering target. One reason for this is the complexity of the mechanism by which ions are stopped in a substrate; another is that the properties of the substrate are continuously modified by the incoming ions.

#### 2.2.3.1 Theory

The depth distribution depends on the implant energy, the energy loss experienced by implanted ions per unit distance travelled through the substrate, the degree to which those ions travel in straight lines, and the rate at which the substrate surface is sputtered away by the incoming ion beam.

The theory which describes the energy loss and stopping of low-energy ions travelling through a substrate is not as well developed as one might like. One problem is that low-energy ions move slowly enough to interact chemically with substrate atoms: "molecules" are

formed and broken up as an ion moves through the substrate. A rigorous, time-dependent, quantum-mechanical description of this process is out of the question. (To gain a sense of the time scale over which the ion/atom interaction occurs, the following approximations may be helpful: a 10 keV Ne ion moves at approximately $10^6$ m/s, or some 2 x $10^{16}$ Bohr radii per second; in a slash-and-burn-crude classical approximation, a hydrogen electron completes some $10^{16}$ revolutions per second. A point to be made from this is that, at much higher ion velocities--velocities typical of, say, projectiles in a nuclear-scattering experiment--substrate electrons may nearly as well be standing still. At much lower velocities, substrate electrons complete many classical orbits while the projectile ion is in their vicinity.)

In addition to the sheer complexity of the energy-loss mechanism, there is a complication that hampers the translation of ion-energy-loss information into ion-depth-distribution information: the ions don't go straight in the substrate; they meander. (The reasons for this are simple and widely known: at a low projectile energy, the cross section for Coulomb scattering through an appreciable angle is generally quite large, while atoms in any solid substrate are quite closely spaced.) Therefore the path length over which an ion travels and loses energy is not a length in which we are particularly interested; to calculate a depth distribution, we need the *projected range* of the ion--the depth into the substrate it reached before stopping.

Fortunately, an idealized description of ion implantation that

captures the essence of the ion/atom interaction and facilitates calculation of, at least, moments of the ion-depth distribution has been made. In the LSS projected-range theory ([Lin63], [Gib75]), two relatively simple scattering processes are abstracted from the complex ion-atom interaction: elastic collisions of ions with substrate nuclei, to which collisions are attributed some of the energy loss and all of the angular scattering; and inelastic collisions of ions with electrons modelled using the Thomas-Fermi atom. An analogy that aptly describes the intent of the LSS abstraction: ion-implantation is like playing pinball in pea soup.

An accurate description of the implanting process also requires detailed knowledge of the substrate throughout the implant. But the substrate is continually changing in several ways as the implant proceeds: the substrate is accumulating implanted ions whose distribution is not, generally, uniform with depth; the substrate is accumulating stress; and the substrate surface is being sputtered away.

If the accumulating implant distribution were known to be uniform with depth, the evolving substrate could be modelled, within the LSS theory, using a weighted average of (pristine) substrate and implant properties ("Bragg's rule", see [Chu78]). But, the LSS theory does not provide for nonuniformity in the substrate; it cannot, for it calculates *moments* of the projected-range distribution. Accordingly, since the implant distributions of interest here are nonuniform, the accumulating-implant problem is ignored here. The accumulating stress

is also ignored.

Sputtering of the substrate, in contrast, can be modelled with relative ease if the sputtering yield is known: one simply "implants" in stages, shaving away the surface of the substrate with its accumulated ions after each stage. Although this method of modelling allows for a sputtering yield that varies as the implant accumulates, available sputtering-yield data are insufficient to direct that variation, and so the yield is assumed constant.

#### 2.2.3.2 The program RANGE

The Fortran program RANGE models ion implantation using an approximate parameterization, calculated and compiled by J. F. Gibbons, et al. [Gib75], of the LSS projected range distribution as developed by Sanders [San68]. Of several approximations described in [Gib75], the most detailed is the Edgeworth distribution--the product of a polynomial and a Gaussian function--derived from the first three moments of the LSS range distribution. RANGE calculates the Edgeworth distribution according to formula (4.9) in [Gib75] from the moments compiled in that reference.

RANGE accepts as input the areal number density of ions to be implanted, the sputtering yield, and the three distribution moments. These numbers completely describe the implantation process in the approximations discussed above. The implant substrate is divided into slices normal to the incident-ion direction; the slices are used as bins

into which implanted ions are deposited as the modelled implantation proceeds. RANGE accepts a number of other quantities whose net effect, for purposes here, is to specify the thickness of the slices.

Using the sputtering yield, RANGE calculates the ion dose that would completely sputter away a single slice of the substrate. (Normally for us, this dose is a small fraction of the total dose.) Implantation of this dose is modelled by binning the Edgeworth distribution into the array of slices, according to their depths in the substrate, and then removing ("sputtering away") the slice nearest the substrate surface along with its binned implant. Modelling continues in steps like this, the substrate surface receding after each step, until the total ion dose has been administered. The modelling process is illustrated in fig 2.14; results of actual RANGE calculations for 15 keV Ne into carbon and aluminum substrates are shown in fig 2.15.

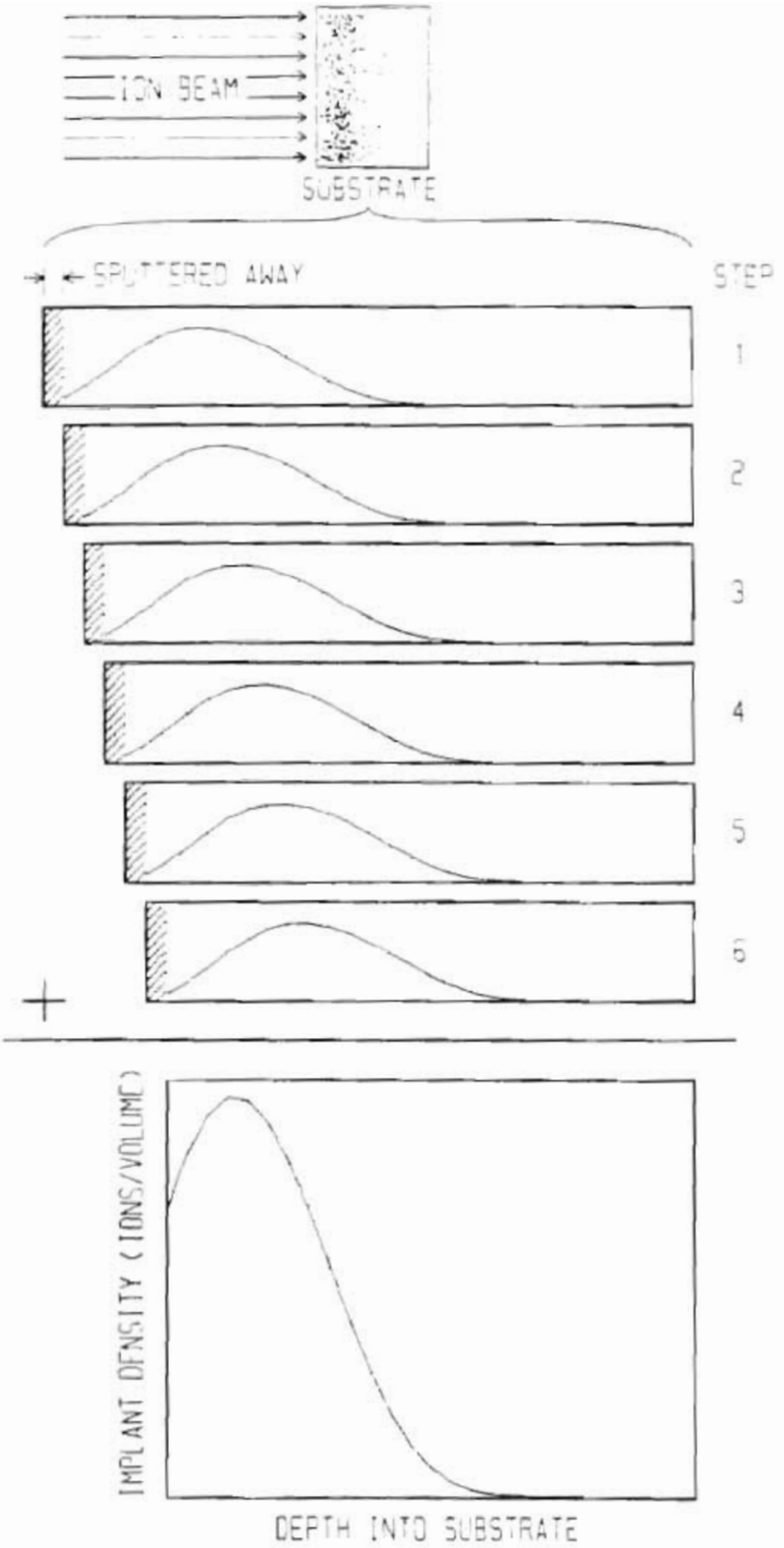


**Figure 2.14** Sample calculation of an implant-depth distribution using the LSS Theory supplemented with sputtering-yield data.

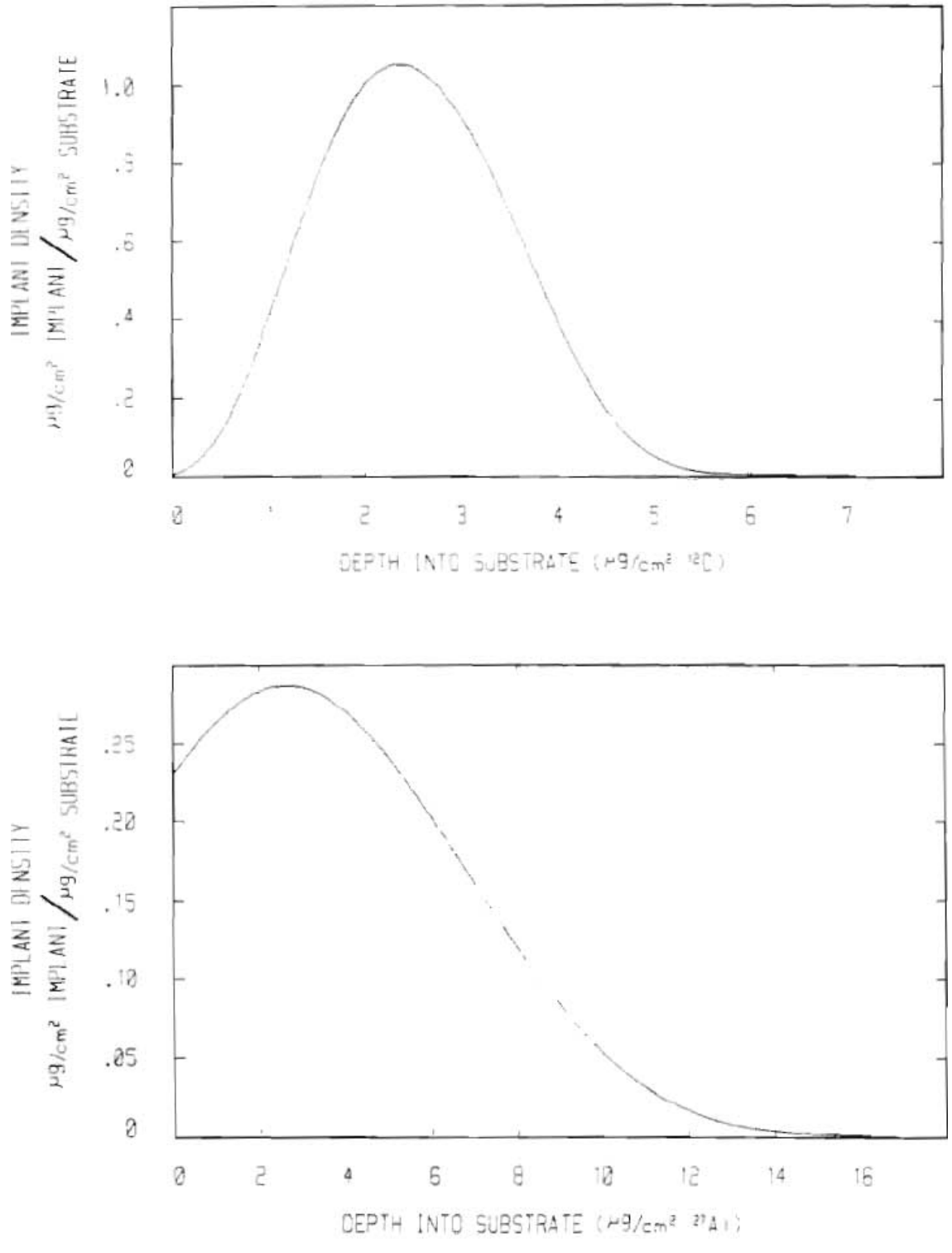


**Figure 2.15 Calculated depth distributions for carbon (top) and aluminum (bottom) substrates.**

### 2.2.4 Modification of the implanter

Implant-modelling calculations indicated that optimal $^{20}Ne$ targets in carbon and aluminum substrates would be produced with implant energies in the range [10 ... 15] keV. Lower energies would produce too thin a target; higher energies would produce too deep an implant. However, the lowest energy implanter available to us had a minimum implant energy of 25 keV.

The 25 keV limit was imposed by the extraction voltage used to draw Ne ions from the implanter's duoplasmatron. With extraction voltages lower than this the implanter behaved very unstably and produced little beam. There was no provision in the implanter design for deceleration of the beam from the extraction energy; our modifications addressed this.

In the first modification, the unipolar accelerating-voltage supply was replaced with one of the opposite polarity so that the beam might be decelerated (from 25 keV) rather than accelerated. This simple and plausible modification didn't work because, with the new power supply arrangement, the deceleration voltage could not be maintained as charge was lost from the high-voltage frame into the exiting beam. In figure 2.16 are shown the paths through which charge is lost from and returned to the ion source. The beam path is non-ohmic: the amount of current flowing through this path is not proportional to the potential difference spanned by the path.

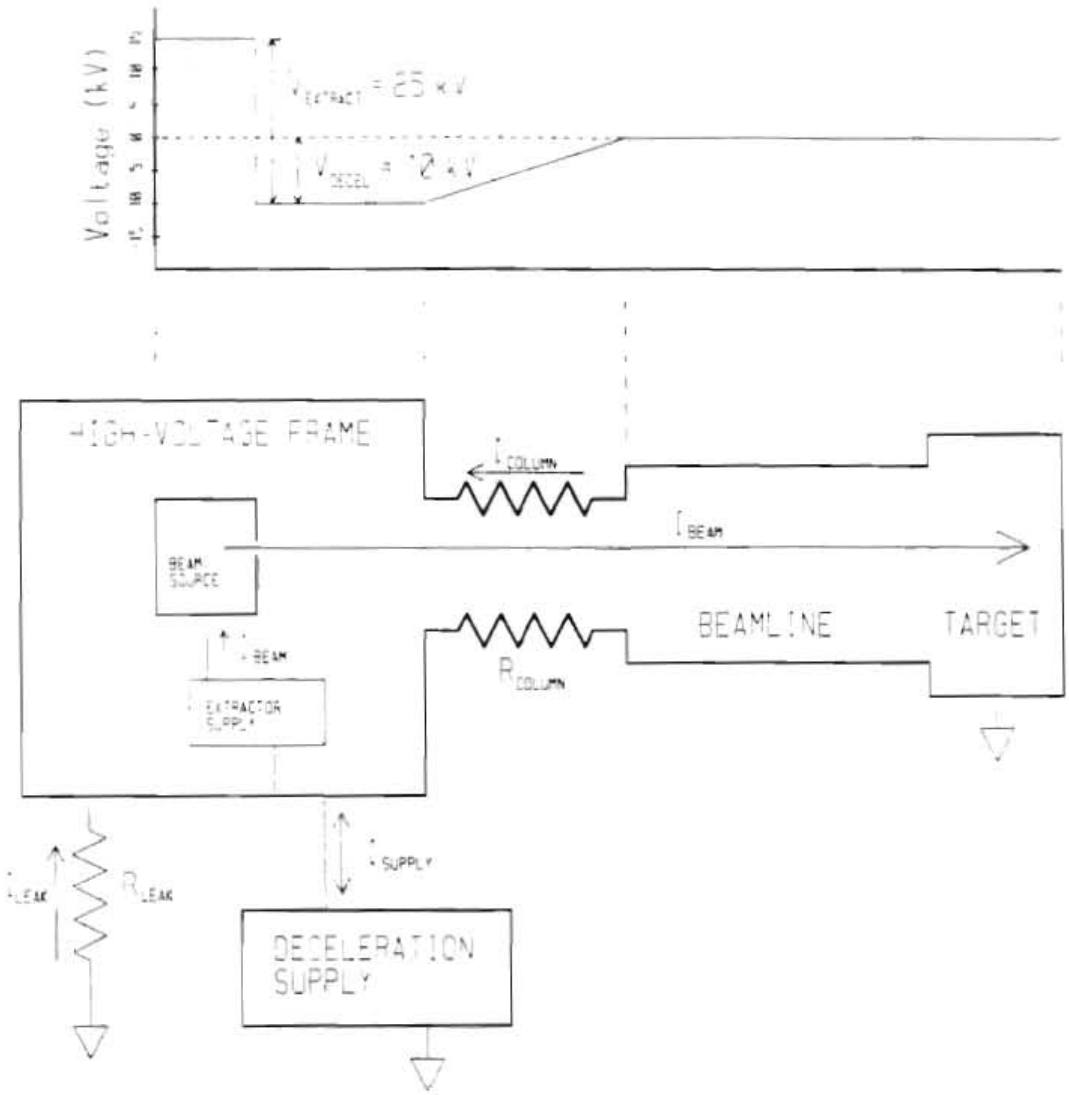


Figure 2.16 Schematic view of voltages and charge paths in the ion implanter.

With the high-voltage frame fixed at -10 kV, a fixed current $I_{column}$ flows from ground into the frame through the fixed resistance $R_{column}$, and a variable current $I_{beam}$ flows from the frame to ground (at the target) in the form of a 15-keV beam of Ne ions. Any difference between these currents must be made up by the decelerating-voltage power supply. If $I_{beam}$ is smaller in magnitude than $I_{column}$, there is no problem. The deceleration supply pumps a balancing positive charge from the frame to ground to maintain the negative frame voltage; this is the job the supply was designed to do. If, however, $I_{beam}$ is greater than $I_{column}$, the deceleration supply must pump positive charge *into* the frame to prevent its voltage from becoming more negative than -10 kV. The unipolar, negative voltage supply was not designed to do this.

An additional modification was made to the implanter that provided a return current $I_{leak}$ to supplement $I_{column}$ so that $I_{beam}$ would never be greater than their sum. This was accomplished by connecting the high-voltage frame to ground through a 1000 MΩ resistance.

# 3. Experimental work

## 3.1 Low-resolution excitation functions (T = 1/2 states)

### 3.1.1 Motivation for the measurement, previous results

One source of isospin impurity in the nominally T = 3/2 states of $^{21}$Na is the quantum-mechanical mixing of these states with T = 1/2 states (which are by far the majority of $^{21}$Na excitations in the energy region of interest here). This mixing could arise from an isospin-non-conserving component of the strong interaction, as well as from the Coulomb interaction. Both sources of mixing are interesting, the first for what it might imply about the mechanisms underlying the nuclear force, and the second for the nuclear-structure information that might be gleaned from detailed analysis of the mixing.

To study mixing, one needs information about the states that mix. In a previous calculation [Orm86] of isospin mixing, the information comprised shell-model calculations of the T = 1/2 wave functions and their excitation energies, shell-model calculations of the T = 3/2 wave functions, and measured excitation energies of the T = 3/2 states. Since this calculation was to be compared with the results of a scattering experiment, isospin impurity of the target nuclei was also addressed. The results are somewhat less precise than one would like:

error bars on the calculated quantities (resonance reduced widths) are much larger than those on the experimentally determined quantities, greatly reducing the significance of any agreement-within-errors between the two. The uncertainties in the mixing calculation stem principally from large (~500 keV) uncertainties in the calculated excitation energies of the T = 1/2 states; the energies can, in principle, be measured with much greater precision than this. One motive for studying these states, then, is the hope that measured excitation energies will yield more precise calculations of isospin mixing.

There is another way the study of T = 1/2 states can provide useful input to calculations of isospin mixing. Errors in the calculated wave functions of these states contribute to errors in the calculated reduced widths of the T = 3/2 resonances, but the contribution is extremely difficult to quantify. This difficulty suggests the disturbing possibility of an uncertainty that is not demonstrated by the error bar assigned to the calculation result. One would like to know how nearly correct the wave functions are, or at least to know that the wave functions demonstrate observed properties of the states. Study of $^{21}$Na excitation functions can yield, for example, spectroscopic factors of the identified T = 1/2 states; since these factors are calculable from wave functions, they provide a "reality check" on those wave functions.

### 3.1.2 General remarks

Cross-section and analyzing-power excitation functions of

$^{20}$Ne(p,p)$^{20}$Ne scattering were measured at eight angles, in steps of approximately 7 keV, over the incident energy region from 6.4 to 7.7 MeV. (This energy region includes the T = 1/2 states within ~600 keV of the lowest-energy T = 3/2 state in $^{21}$Na.) The data were taken with polarized beam incident on a gas-cell target filled with chemically pure (99.9%) neon in its natural isotopic abundance: 90.5% $^{20}$Ne, 9.2% $^{22}$Ne. The beam polarization was monitored continuously throughout the experiment with a $^{4}$He polarimeter mounted in the beamline downstream from the scattering chamber.

Polarized protons from the TUNL Polarized Ion Source [Cle74] were directed to target through the dual-90-degree energy-analyzing system. This high-energy-resolution analyzing system was used (in what is otherwise a low-resolution experiment) because it has a good absolute energy calibration and so that the beam energy resolution would contribute negligibly to the total resolution function.

### 3.1.3 Use of the polarization monitor

From previous experience with the polarimeter and knowledge of the approximate cross section for $^{20}$Ne(p,p)$^{20}$Ne in this energy region, it was clear that the counting-time limitation for this experiment would result from the polarimeter. That is, at each energy step, data acquisition would continue until sufficient scattering events had been recorded by the polarimeter so that statistical errors in the extracted beam polarization would be less than 3 percent. This fact allowed considerations other than count rate, such as minimization of the

target-resolution function and the need for data from many scattering angles, to dictate the detector configuration and target-gas-cell pressure.

The polarimeter counting-time limitation was minimized by mounting the polarimeter "backwards" so that its detectors monitored $^4$He(p,p)$^4$He scattering at a laboratory angle of 68 degrees, rather than the usual 112 degrees. While this change reduced the magnitude of the polarimeter analyzing power, the increased cross section at 68 degrees resulted in a figure-of-merit (cross section times the square of the analyzing power) of 52.4 at $E_p$ = 7.0 MeV, a 16 percent improvement over the usual configuration. Cross-section and polarization data used in this determination are from [Sch71].

### 3.1.4 Scattering chamber geometry

The gas cell used in the main scattering chamber was a 2.54 cm diameter cylinder with 2.5 micron (.099 mil) Havar-foil walls. Pressure in the cell was monitored electronically and maintained at a constant value of 0.34 Atm., with an error estimated at less than 5 percent, throughout the experiment.

Eight surface-barrier detectors, at laboratory scattering angles of 38.0, 52.4, 64.0, 75.5, 87.15, 107.2, 138.9, and 155.0 degrees were employed in an "unpaired" configuration (see fig. 3.1). This differs from the arrangement normally used for measuring analyzing powers, in which pairs of similar detectors are placed symmetrically about the

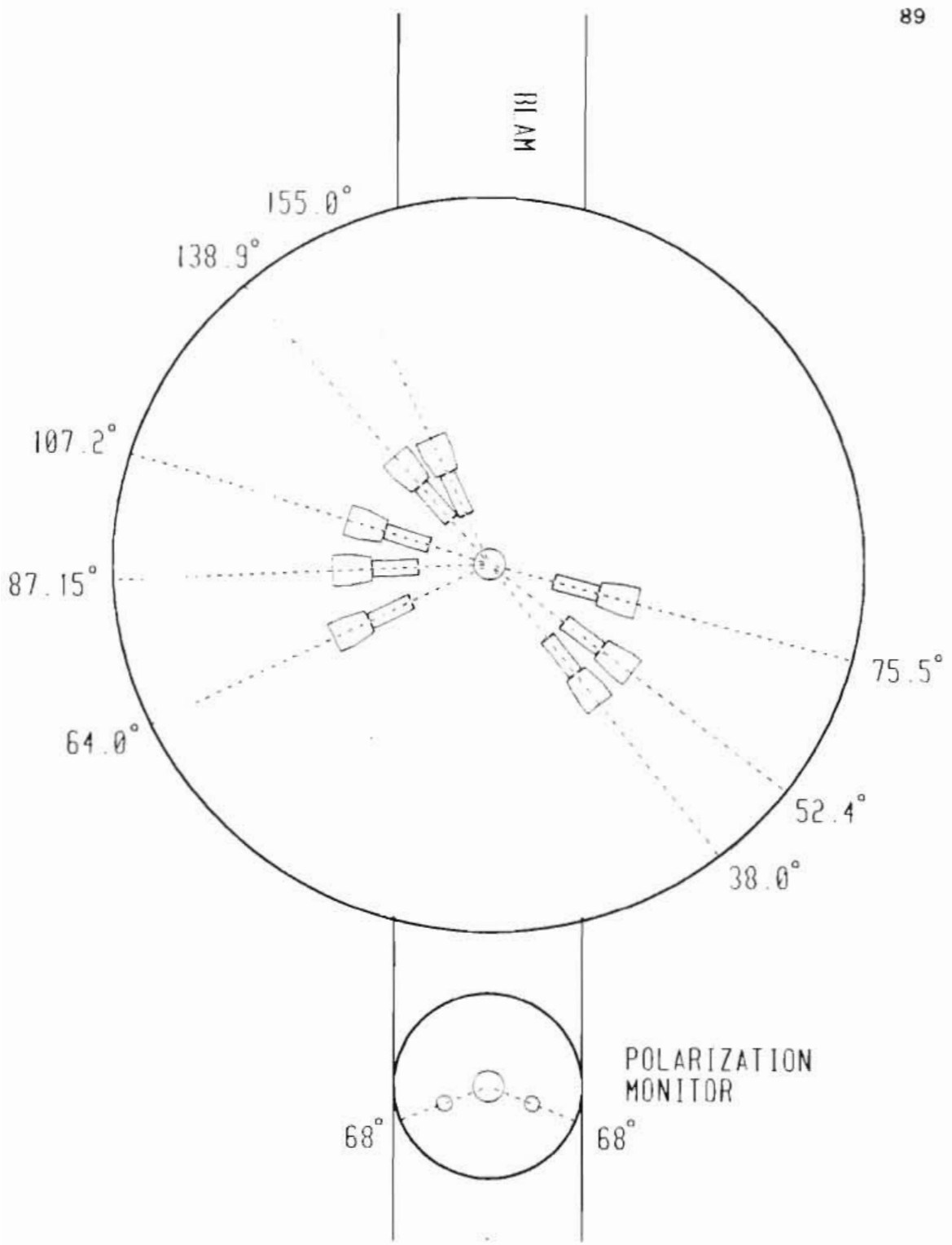


**Figure 3.1** The chamber configuration for low-energy-resolution excitation functions.

axis defined by the beam direction. The symmetric arrangement can lessen the effects of errors in scattering geometry on the extracted analyzing power by gathering information which would be redundant in the absence of those errors. It can also halve the counting time required to reach a given statistical precision by effectively doubling the detector solid angle at each scattering angle. For this experiment, the doubled solid angle would yield little advantage since the counting-time limitation was imposed by the polarimeter.

The scattering angles of 38.0, 52.4, 87.15, 107.2, and 138.9 degrees were chosen to correspond with zeros of low-order Legendre polynomials. This was done to help determine the L values of resonances identified in cross-section data. (Only L = 0, 1, or 2 scattering is expected in this mass and energy range.)

Detector-slit widths, collimator lengths, and distances from the target (see table 3.1) were such that a centered region approximately one cm in length along the path of the beam through the gas cell was visible to all detectors (see fig. 3.2). This constraint on detector geometry was accepted so that the target energy-resolution function would be the same for all detectors, and to insure that the detectors could not view scattering from the cell walls.

Beam current was monitored by grounding the Faraday cup through an integrating current meter. Electron suppression of the Faraday cup was accomplished by applying -60V to an electrically

isolated cylinder placed upstream from the Faraday cup. (See fig. 3.3.)

| angle | slits (mm) | distance (cm) |
|---|---|---|
| 38.0 | 1.587 | 7.62 |
| 52.4 | 1.587 | 7.62 |
| 64.0 | 2.381 | 6.98 |
| 75.5 | 3.175 | 5.40 |
| 87.15 | 3.175 | 5.71 |
| 107.2 | 2.381 | 5.08 |
| 138.9 | 2.381 | 4.76 |
| 155.0 | 1.587 | 4.44 |

Table 3.1 Detector angles, slit widths, and distances from center of target to front slit.

The absolute normalization uncertainty in low-resolution cross-section data is estimated to vary slightly with scattering angle from a low of 11 percent at 90 degrees to a high of 12 percent at 155 degrees. These figures result from addition-in-quadrature of the following estimated uncertainties: 5 percent in measurement of the target gas-cell pressure; 10 percent in beam integration; 2 percent in measurement of slit-widths and -distances; and 0 (at 90 degrees) to 4 (at 155 degrees) percent due to a .5-degree uncertainty in the scattering angle. The dependence on scattering angle ($\theta$) stems from the

appearance of $1/\sin(\theta)$ in the expression for the $G_{0\,0}$ *factor* [Sil59]--loosely, the effective detector solid angle.

The absolute normalization uncertainty in analyzing power data is estimated to be 10 percent and attributable largely to uncertainty in spectrum background subtraction.

### 3.1.5 Step excitation functions

Excitation functions were acquired by manually stepping the field in the energy-analyzing magnet. The TUNL automatic stepping system discussed in chapter 2 was not used because that system sacrifices stepping speed for precision--opposite to the priority required for this experiment. Also, that system cannot automatically adjust the tandem accelerator voltage by the amount required to span the energy region studied.

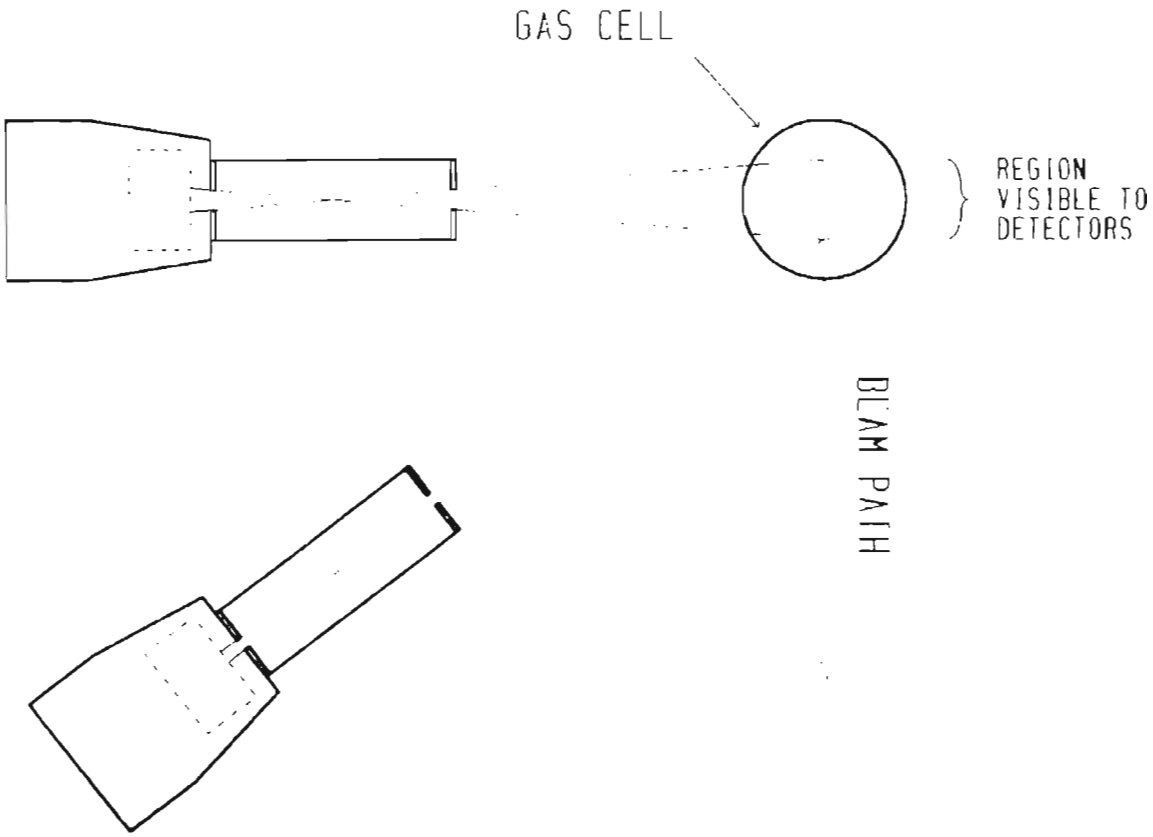


Figure 3.2 The visible region of the gas-cell target.

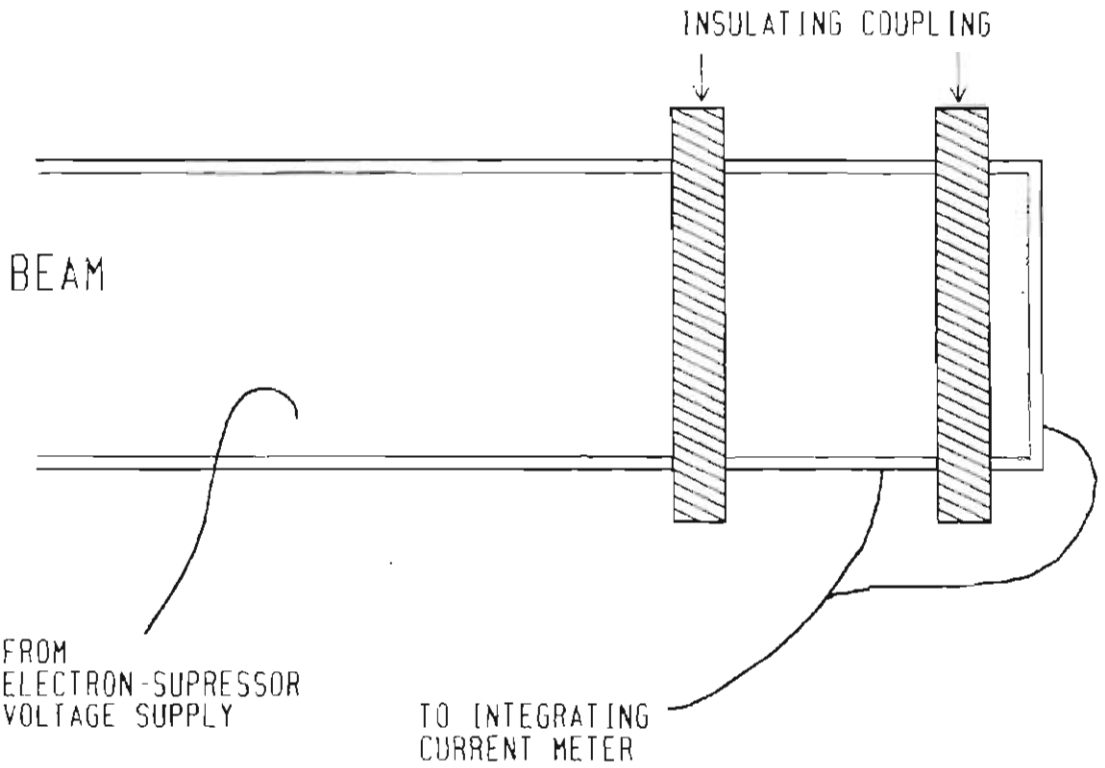


Figure 3.3 The Faraday cup and electron suppressor.

### 3.1.6 HSYS: online calculation of scattering observables

The first step in the extraction of physically significant quantities from raw scattering data is the conversion of scattering yields to cross section and analyzing power as functions of angle and energy. It is a great convenience to have results of this preliminary data analysis available online while new data are being acquired, since the results can call attention to and help diagnose problems in the data-acquisition procedure or equipment, and they can help in optimizing use of the remaining accelerator time.

In previous work [Var86] at TUNL, a package of programs in the DEC Command Language (DCL) and in Fortran was written to perform online and offline calculation of cross section and vector analyzing power; an overlapping set of programs was written [Kar85] for calculation of tensor analyzing powers. The packages--dubbed VSYS and TMOM--were intended primarily for analysis of angular-distribution data and are well suited in execution speed to the schedule typically followed in acquiring such data: runs of several hours followed by pauses of several minutes for changes in scattering angle. In this schedule, the three minutes or so required by VSYS--the speedier of the two packages--for calculation between runs poses no problem.

Acquiring an excitation function is different: runs and the pauses between them are short. In the low-resolution excitation function described here (an extreme example), the following schedule was planned: 3 1/2 minutes of data acquisition, followed by twenty seconds

of dead time for calculations and a spin flip or energy change. A faster calculation package than VSYS was required to make efficient use of accelerator time.

The calculations and computational housekeeping required for preliminary analysis of a single run's data can be done by the VAX in less than one second. By simple time trials, it was discovered that much of the additional time VSYS used for this task was attributable to the launching of some 70 separate Fortran programs. Since no simple modification of VSYS could change its behavior in this regard, a new package, called HSYS, was written.

For the most part, HSYS is simply a recoding of the separate VSYS Fortran and DCL programs into Fortran subroutines called by a single main program. An advantage of VSYS is lost in this recoding: since DCL is interpreted, rather than compiled, VSYS can be quickly modified on the fly to conform with, for example, different detector arrangements. To minimize this loss, HSYS is configured in part from text files that describe to it the data-acquisition setup. The required flexibility in HSYS' internal workings was obtained by implementing one level of indirection in its referencing of data structures; rather than directly accessing memory locations as, e.g., "DATA(1)", HSYS routines access memory through an array of indices as "DATA(LOCATOR(1))", where the LOCATOR() index array is initialized according to information in the configuring text file.

HSYS performs all online calculations on a single run's data in approximately three seconds, imposing a negligible delay in acquisition of excitation-function data. Also, HSYS cooperates with the TUNL automatic energy-stepping system by shifting the XSYS gates in response to a change in beam energy. (The stepping system was not used in this run, but gate shifting was done by HSYS nevertheless.)

## 3.2 Location of T = 3/2 states

### 3.2.1 General remarks

To study T = 3/2 states in $^{21}$Na, one must locate those states. The theory of isospin guarantees that for every state in $^{21}$F there are corresponding states in $^{21}$Ne, $^{21}$Na, and $^{21}$Mg (see fig. 1.2), but it does not specify the excitation energies of those states. (Nor, for that matter, does it specify their isospins although it places the lower limit T = 3/2.) In addition, the states are expected to occur at roughly 8 MeV in excitation energy and are therefore expected to be surrounded by a large number of T = 1/2 states. Consequently, while knowledge of the level structures of the parent nuclei $^{21}$Mg and $^{21}$F can help direct the search for T = 3/2 states in $^{21}$Na, additional information is required to locate candidate states and verify their isospins.

It is possible to infer approximate locations of T = 3/2 states, from known locations of corresponding states in the parent nucleus and assumptions about the isospin-non-conserving part of the nuclear Hamiltonian, using the Isospin Mass Multiplet Equation (IMME) [Jan69]. This equation gives the energy splitting of the various members of an isospin multiplet due to two-body charge-symmetry breaking effects in the approximations of first-order perturbation theory. In view of the approximations, the IMME is not expected to be able to pinpoint the locations of T = 3/2 states with great accuracy. Since, in addition to the energy locations of higher-lying T = 3/2 states, we required some

verification of their isospin, we did not rely exclusively on the IMME in locating the states.

In sec 1.2 it was argued that $^{20}Ne(p,p)^{20}Ne$ scattering through T = 3/2 compound-nucleus states occurs only over narrow ranges of incident-proton energy. The argument is not reversible: a narrow resonance observed in a $^{20}Ne(p,p)^{20}Ne$ excitation function indicates a long-lived state in $^{21}Na$, but additional information is needed to attribute that state's long life to its isospin. However, if other reasons for that long life seem implausible, a narrow resonance in $^{20}Ne(p,p)^{20}Ne$ strongly suggests the existence of a T = 3/2 state.

But studying resonant scattering is not an ideal way to search over a wide energy range for T = 3/2 states. Since the resonances are typically of energy-width less than 1 keV, data points must be closely spaced (say, 300 eV) in energy. Therefore a great many data points must be acquired to search a wide energy region. Worse, since formation of the resonances is isospin forbidden, the resonances are expected to be relatively faint and good statistical precision is sometimes needed to see them. So, ironically, the most obviously distinctive feature of T = 3/2 states as viewed in excitation functions, their narrowness, is a hindrance in locating them.

Also, because of the manner in which wide-range step-excitation functions are acquired, one must know in advance what statistical precision is needed to discriminate the searched-for resonances from

background scattering. For high-resolution step-excitation functions particularly, it is impossible to increase statistical precision by scanning an energy region more than once because the required energy step size is smaller than the beam-energy reproducibility. Ideally, one would like to investigate a broad range of excitation energies simultaneously--as can be done, for example, with a spectrograph that analyzes the energy of a particle after it has scattered.

Therefore, in at least the initial search for T = 3/2 states, one wants a scattering mechanism that is isospin-allowed to populate those states, that nevertheless discriminates according to isospin, and for which the excitation energy of the populated states is reflected in the energy of the exiting particle. One also wants a data-acquisition system that can span a broad energy range with good energy resolution and calibration.

### 3.2.2 Previous work

Some of the T = 3/2 states in $^{21}$Na have already been located and verified. The lowest two T = 3/2 states were observed [But68] in $^{23}$Na(p,t)$^{21}$Na and $^{23}$Na(p,3He)$^{21}$Ne angular distributions, and were assigned spins and parities $5/2^+$ and $1/2^+$, respectively. The spin assignments, which agree with those of ground and first excited states in $^{21}$F, were subsequently verified in a study of $\gamma$ decay [Bea70] from them.

McDonald [McD69] measured cross-section excitation functions of

$^{20}$Ne(p,p)$^{20}$Ne over an energy region including the lowest two T = 3/2 states in $^{21}$Ne with sufficiently high energy resolution to see clearly resonances from the isospin-forbidden decay of these states and assigned the excitation energies 8.973 MeV and 9.219 MeV.

In previous work [Wil82], the (p,t) and (p,$^{3}$He) reactions have been used to locate T = 3/2 states in A = 4n+1 nuclei. Both of these reactions populate T = 1/2 and T = 3/2 states in the residual nuclei; the relative cross sections differ in part because of a correlation, imposed by the Pauli Exclusion Principle, between isospin transfer and angular momentum transfer.

In the (p,t) reaction, a pair of neutrons is transferred from the target nucleus to the projectile; in the (p,$^{3}$He) reaction, a neutron-proton pair is transferred. The isospin transferred in the nn pair can't be other than T = 1, while the isospin transferred in the np pair can be either T = 1 or T = 0. This is the essential difference between the two reactions that bears on their abilities to populate differentially T = 1/2 and T = 3/2 states.

Ignoring the spectator proton, the isospin equation that describes the $^{23}$Na(p,t)$^{21}$Na reaction populating a T = 1/2 state is the following:

$$^{23}\mathrm{Na} \text{ ---> } ^{21}\mathrm{Na} + \mathrm{nn},$$

$$[T: \quad 1/2 \quad = \quad 1/2 \quad \dagger \; 1],$$

where the "$\ddagger$" operator describes the vector coupling of component isospins into total isospin, and does so entirely in terms of the norms of those isospin vectors. (The expression "A $\ddagger$ B" can equal any of the following quantities: |A-B|, |A-B|+1, ..., |A+B|-1, |A+B|. By this definition, 1/2 $\ddagger$ 1 can equal either 1/2 or 3/2.) The corresponding equation for the $^{23}$Na(p,$^{3}$He)$^{21}$Ne reaction is

$$^{23}\mathrm{Na} \text{ ---> } ^{21}\mathrm{Ne} + \mathrm{np},$$
$$[T: \quad 1/2 \quad = \quad 1/2 \quad \ddagger \quad (0,1)].$$

Isospin conservation allows all possible values of isospin of the transferred pair in the two equations above. (1/2 $\ddagger$ 0 can equal 1/2; so can 1/2 $\ddagger$ 1.)

But the situation of the pair of equations describing population of T = 3/2 states by these reactions is different. The $^{23}$Na(p,t)$^{21}$Na reaction populating a T = 3/2 state is described by the equation

$$^{23}\mathrm{Na} \text{ ---> } ^{21}\mathrm{Na} + \mathrm{nn},$$
$$[T: \quad 1/2 \quad = \quad 3/2 \quad \ddagger \quad 1],$$

and the corresponding equation for $^{23}$Na(p,$^{3}$He)$^{21}$Ne is

$$^{23}\mathrm{Na} \text{ ---> } ^{21}\mathrm{Ne} + \mathrm{np},$$
$$[T: \quad 1/2 \quad = \quad 3/2 \quad \ddagger \quad (0,1)].$$

Isospin conservation cannot be satisfied merely by selecting one of the possible values of the isospin coupling expression "3/2 ∓ 0" in the (p,$^3$He) equation since no value of that expression equals 1/2.

### 3.2.3 $^{23}$Na(p,t)$^{21}$Na measurements at Princeton

To search for higher-lying T = 3/2 states in $^{21}$Na, we travelled to Princeton University, planning to use the cyclotron and magnetic spectrograph there to investigate the mass-21 system via the reactions $^{23}$Na(p,t)$^{21}$Na and $^{23}$Na(p,$^3$He)$^{21}$Ne.

As it happened, time constraints resulting from unscheduled maintenance prevented us from acquiring both sets of data. After reviewing previous (p,t) and (p,$^3$He) data (from [Wil82]), we concluded the (p,t) data alone would discriminate more effectively between T = 1/2 and T = 3/2 states than would (p,$^3$He) data alone.

#### 3.2.3.1 Description of Princeton laboratory

The Princeton Azimuthally Varying Field Cyclotron Laboratory and the Quadrupole-Dipole-Dipole-Dipole spectrometer used in our study of $^{23}$Na(p,t)$^{21}$Na are shown schematically in figure 3.4. The system is capable of accelerating protons to 48 MeV with an effective beam resolution $\Delta E/E$ of 1/3000, typically. The spectrometer has a large (14.7 msr) solid angle and focusses accepted particles within a wide energy range ($E_{max}/E_{min}$ = 1.25) on a focal plane roughly one meter in useful width.

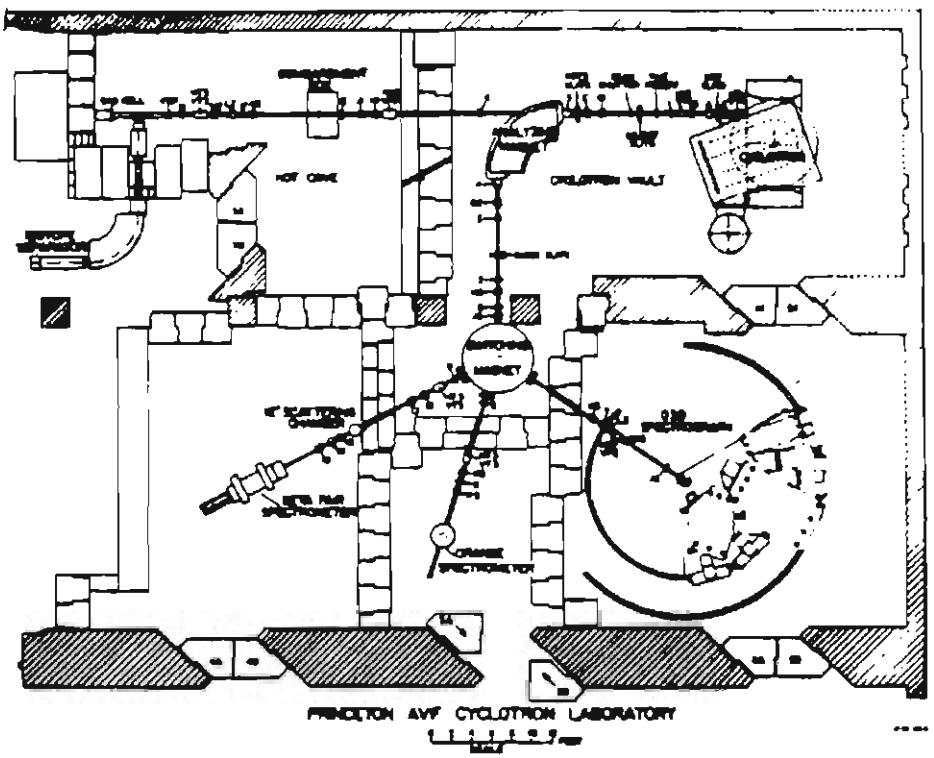


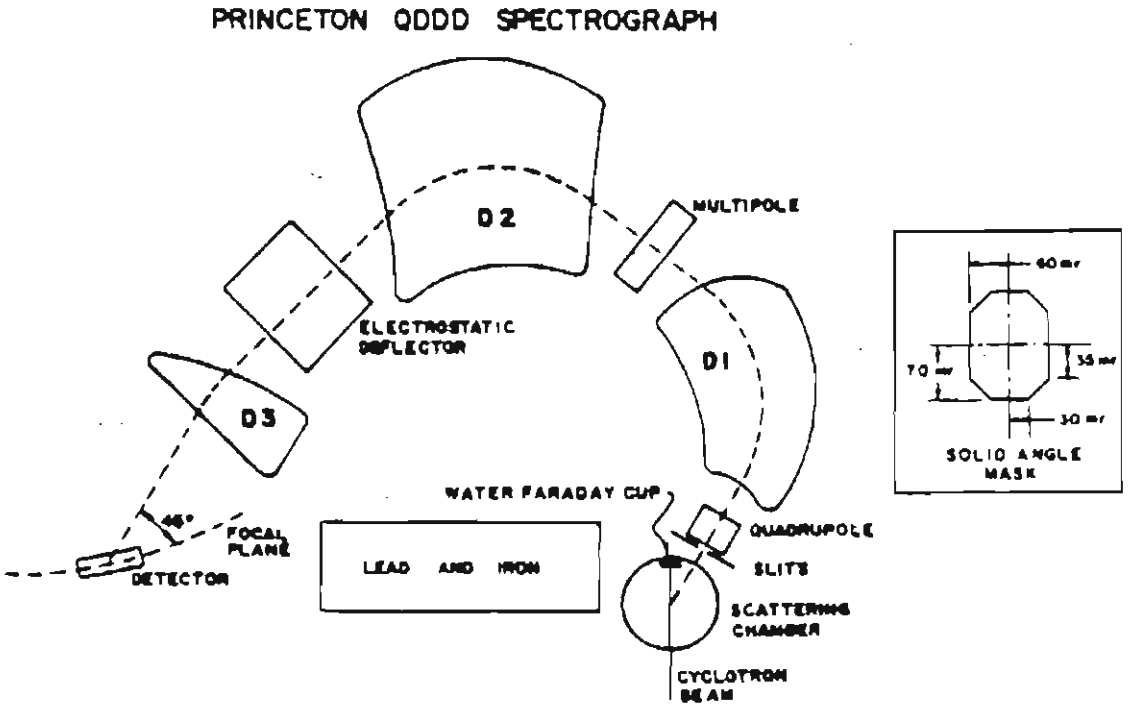


Figure 3.4 The Princeton Cyclotron Laboratory.

Data are acquired from the spectrograph using a position-sensitive detector [Kou74] that also produces information from which the mass and charge of detected particles can be determined. The detector is a resistive-anode gas proportional counter backed by a plastic scintillator coupled to a photomultiplier tube. Particle identification is accomplished by plotting the signal summed from both ends of the resistive anode against the signal from the scintillator. The summed-anode signal is proportional to the square of the particle's mass (and, irrelevantly here, to its energy); the scintillator signal is proportional to $(Z/m)^{2 \cdot 6}$.

### 3.2.3.2 Targets

Targets used in the $^{23}Na(p,t)^{21}Na$ study were of $^{23}Na$ salts evaporated onto carbon backing foils. Pure $^{23}Na$ was not considered for use as a target because Na is unstable under heating in vacuum. Preliminary kinematics calculations with the known states of several halogen isotopes were performed so that the target compound would result in minimal interference from contaminant scattering in the $^{23}Na(p,t)^{21}Na$ spectra. These calculations indicated that the isotope $^{35}Cl$ was the best choice of contaminant given the scattering energies and angles planned for the study.

Target thicknesses were chosen so that the target energy-resolution function contribution to peak broadening would be approximately the same as that of the expected effective beam/spectrometer resolution function: 15 KeV. (This criterion maximizes the count rate

for a given beam intensity while minimizing the additional energy uncertainty caused by energy straggling in the target foil.) Accordingly, targets of thickness between 130 and 190 $\mu g/cm^2$ $^{23}Na^{35}Cl$ were fabricated, bracketing the thickness range indicated by energy-straggling calculations.

In fact, we discovered that the hoped-for effective resolution of 15 KeV could not be reached with our choices of scattering angle and ejectile mass because the required *dispersion-matching* conditions could not be met. Dispersion matching is an arrangement whereby the angle-to-energy correlation that exists in the beam, after it has passed through the analyzing magnet, is mapped onto the target in such a way that the resulting target-position-to-energy correlation just cancels the spectrometer's energy-to-focal-plane-position correlation--i.e., so that it cancels the combined effects of the spectrometer's dispersion and magnification. When dispersion matching is only partially successful, as in our case, the experimental resolution is more vulnerable to the beam resolution than it would otherwise be.

As a result of our oversight, the targets we had made were somewhat thinner than would have been optimal. But there was a more serious problem with the targets. Many more states from $^{35}Cl$ appeared as contaminants in the spectra than those for which kinematics calculations had been performed. Lacking positive identification of a large number of peaks in a spectrum in which we were searching for previously unknown states, we decided to use another target.

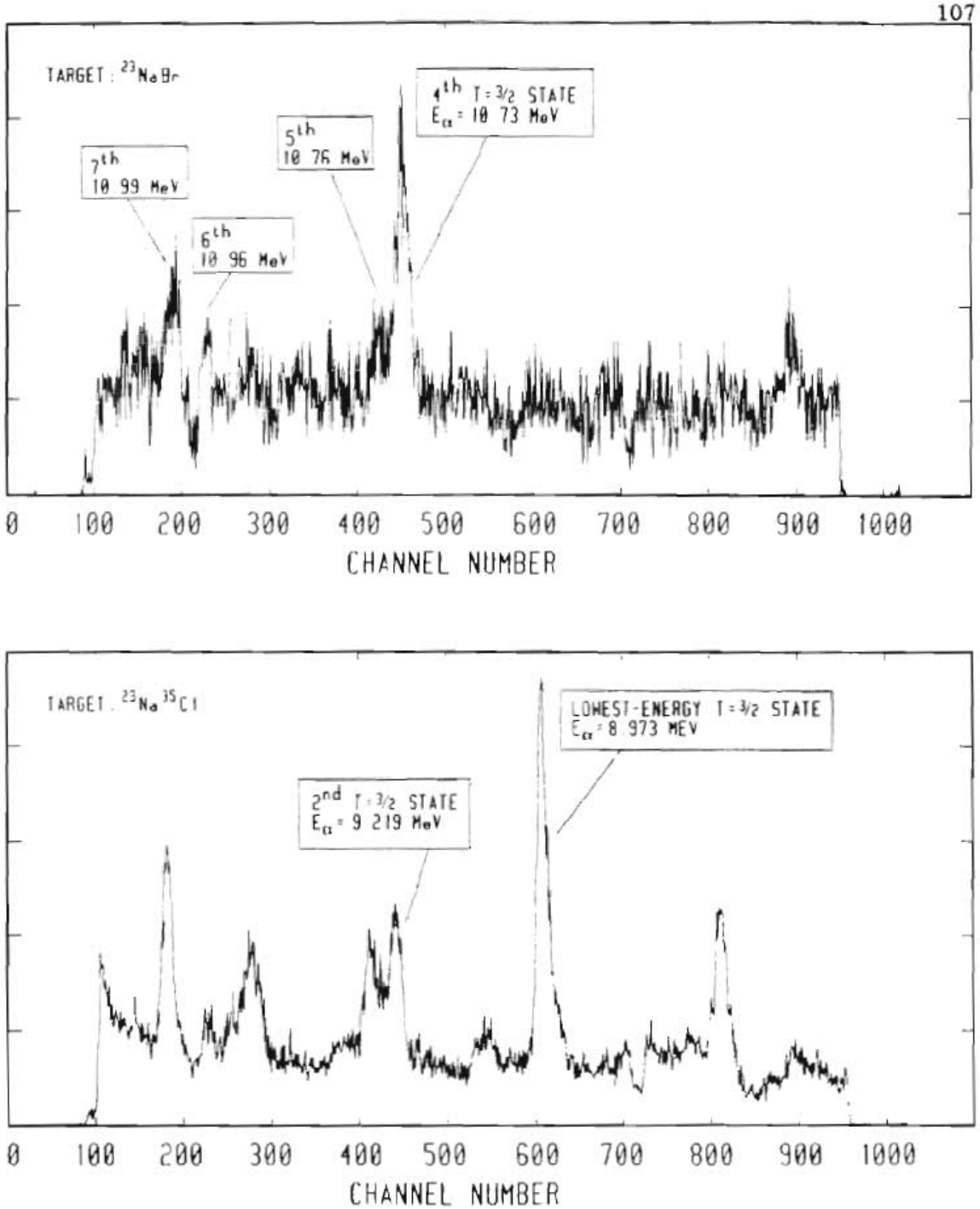


Figure 3.5 $^{23}Na(p,t)^{21}Na$ spectra from the region containing the $1^{st}$, $2^{nd}$ (bottom), and $4^{th}$ – $7^{th}$ (top) T = 3/2 states in $^{21}Na$.

A target of $^{23}$NaBr was provided for our use by Art Champagne, a faculty member at Princeton with whom we collaborated in this study. In the spectra acquired from this target, effects from the Br contaminant took the form of a fairly smooth background, rather than of the many discrete peaks that had contaminated the $^{23}$Na$^{35}$Cl spectra. With this target, we acquired the data shown in the upper spectrum of fig. 3.5: clear $^{23}$Na(p,t)$^{21}$Na peaks and relatively little competing structure in the energy vicinity of the higher-lying T = 3/2 states in $^{21}$Na.

### 3.2.3.3 Data acquisition and spectrum calibration

Data were acquired from the QDDD spectrometer using the computer code ACQUIRE [Kou78], which binned the two signals from the position-sensitive detector into a two-dimensional histogram. Within the two-dimensional histogram, areas within which tritons and deuterons would be binned were specified, after reviewing test-run data, using ACQUIRE's ability to define multiple two-dimensional gates. After the gates had been defined, events landing within them were binned into one-dimensional histograms, or spectra, according to position at the spectrometer focal plane. In this way, separate ejectile-energy spectra were maintained for tritons and deuterons.

To calibrate the spectra, data were acquired from the $^{12}$C(p,d)$^{11}$C reaction populating the 1.999 MeV state in $^{11}$C. This accurately known energy provided the absolute energy calibration of a single reference channel of the spectra. From this energy was calculated the

energy of a triton that would land at the same focal plane position with the same spectrometer settings.

The variation in triton energy with channel number about the reference channel was determined by acquiring $^{23}$Na(p,t)$^{21}$Na data at several different scattering angles and comparing the resulting kinematic energy shifts with the observed channel numbers of the peak centroids. In this way, a point-slope calibration was accomplished across a region approximately one-quarter of the effective width of the detector, in which region the searched-for T = 3/2 states had been located in other runs. An average of 1.31 keV per channel was obtained in the calibrated region by this procedure with a total deviation from linearity of 1.8 percent across the region.

Peaks in the ejectile-energy spectra corresponding to the higher-lying T = 3/2 states in $^{21}$Na (T = 3/2 states numbered four through seven in order of their excitation energies) were identified by comparing their energy differences to those in the parent nucleus $^{21}$F (from [End78]) and in $^{21}$Ne (from [Hin84]). Relative energies of the states calculated from the IMME coefficients given in [Hin84] were also used. The fact that these peaks occur as two barely resolved doublets in the spectra of figure 3.5 agrees well with the energy assignments of both [End78] and [Hin84]. No peak corresponding in energy to the third T = 3/2 state was seen. In view of the assignment [Mai81] of 1/2$^-$ to that state (seen in $^{22}$Ne(d,t)$^{21}$Ne and $^{22}$Ne(d,$^3$He)$^{21}$F), this seems a plausible result: one expects less efficient stripping from the $p_{3/2}$

core shell than from the $s_{1/2}$ and $d_{5/2}$ valence shells, and to form a negative-parity state by $^{23}Na(p,t)^{21}Na$, one must strip from the core.

From these identifications and the energy calibration described, we tentatively assign the excitation energies listed in table 3.2 for the fourth through the seventh T = 3/2 states in $^{21}Na$.

| $E_{EX}$ in $^{21}F$ | $E_{EX}$ in $^{21}Na$ (expected) | $E_{EX}$ in $^{21}Na$ (assigned) |
|---|---|---|
| 0.0 | 8.973 a) | 8.974 a) |
| 0.2799 | 9.220 b) | 9.215 a) |
| 1.101 | 10.05 b) | - |
| 1.730 | 10.70 b) | 10.73 |
| 1.755 | 10.72 b) | 10.76 |
| 2.040 | 10.99 b) | 10.96 |
| 2.071 | 11.02 c) | 10.99 |

Table 3.2 Comparison of T = 3/2-state excitation energies in $^{21}F$, expected $^{21}Na$ excitation energies and current, tentative $^{21}Na$ excitation-energy assignments. (All energies are in MeV.)

a) energies assigned from current high-resolution excitation functions--used as calibrants.

b) energies from current 8.973-MeV assignment and IMME derived relative energies from [Hin84].

c) energy from doublet separation in $^{21}F$ and determination (b).

### 3.2.3.4 What(p,t) alone says about T

As mentioned previously, we were not able to acquire both (p,t) and (p,$^{3}$He) data, which together would have provided additional confirmation of the T = 3/2 character of the $^{21}$Ne states we observed. Fortunately, in cases such as ours, the (p,t) reaction alone can be expected to populate (low-lying) T = 3/2 states in light nuclei more readily than it populates many of the nearby T = 1/2 states. No selection rule is necessarily illustrated by this behavior; instead, it is a consequence of the reactions' spectroscopic factors for populating the different states.

Low lying T = 3/2 states in $^{21}$Na--for all their high excitation energy in $^{21}$Na--are isobaric analogues of the ground and first few excited states in $^{21}$Mg. As such they are presumed to have simple structures and, by this, to resemble in structure the ground state of $^{23}$Na, but for the lack of a pair of valence neutrons. That is, the direct products of wave functions of these states with the wave function of a pair of neutrons might be expected to overlap considerably with the $^{23}$Na wave function, yielding an appreciably large spectroscopic factor. The T = 1/2 states in the energy vicinity of the T = 3/2 states, on the other hand, have no analogues in $^{21}$Mg and there are a great many states in $^{21}$Na of lower excitation energy than theirs. One might confidently expect many of these T = 1/2 states to exist in complicated nuclear configurations that aren't formed with high probability by the stripping of two neutrons in the (p,t) reaction.

## 3.3 High-resolution excitation functions

### 3.3.1 Previous work

The two lowest-energy T = 3/2 states of $^{21}$Na were previously studied by A. B. McDonald [McD69] in a high-energy-resolution experiment using unpolarized protons on a differentially pumped gas-cell target. Natural neon gas at a pressure of about 3 Torr was used, producing a maximum target thickness of 700 eV, with an additional 300 eV due to the Doppler effect. Excitation functions of cross section were taken in 1-keV steps with a beam whose resolution was less than 1.5 keV, but otherwise unknown. For the T = 3/2 state at $E_p$ = 6.872 MeV, a resonance width ($\Gamma$) of less than 1.2 keV, and a partial width ($\Gamma_p$) of 0.1 $\pm$ 0.05 keV were inferred from analysis of the data. For the state at $E_p$ = 7.128 MeV, $\Gamma$ = 2.3 $\pm$ 0.5 keV and $\Gamma_p$ = 1.1 $\pm$ 0.3 keV were found.

Subsequently, the lowest energy T = 3/2 state data from [Mcd69] were re-analyzed by P. G. Ikossi [Iko75] in light of a branching-ratio ($\Gamma_p/\Gamma$) measurement [Gou73] that had been made in the interim. In this measurement of $\beta$-delayed proton decay, the ratio $\Gamma_p/\Gamma$ = 0.20 $\pm$ 0.02 was determined for decay from the lowest-energy T = 3/2 state in $^{21}$Na to the $^{20}$Ne ground state. In Ikossi's analysis, the resonance full width was determined, as $\Gamma$ = 750 $\pm$ 50 eV, by fitting the data. With the value 0.2 for the branching ratio, this implies that $\Gamma_p$ = 150 $\pm$ 12 eV. From $\Gamma_p$, the reduced partial width, $\gamma_p^2$ = 165 $\pm$ 13 eV, was calculated.

### 3.3.2 General remarks

Our decision to study the low-lying T = 3/2 states in $^{21}$Na was not motivated by any perceived inconsistency between the results of [Mcd69], [Iko75], and the results of recent isospin-mixing calculations [Orm86]. Rather, we observe that the general agreement-within-errors between these experimental and theoretical results could be rendered more meaningful if error bars and calculational uncertainties were reduced. Another motive was the hope that a new measurement, using our polarized-proton beam, of the second T = 3/2 resonance might more precisely determine its partial width, $\Gamma_{p1}$, as the branching-ratio measurement did in the case of the elastic decay. Finally, we hoped to extend measurements to higher-lying T = 3/2 states in $^{21}$Ne.

Wilkerson [Wil82] found that fitting high-resolution excitation functions of both analyzing power and cross section applies a powerful constraint on the value of the partial width $\Gamma_p$ (a fit parameter) that fitting cross-section data alone does not apply. Since TUNL has the rare and valuable capability--producing a highly polarized beam with good energy resolution--required to wield this constraint, we have reason to hope that a polarized-beam study, at TUNL, of the isospin-forbidden, resonant decay of T = 3/2 states in $^{21}$Na can yield more reliable indications of the isospin mixing in that nucleus and in the $^{20}$Ne ground state than have previously been available.

### 3.3.3 Targets

Ion-implanted targets of isotopically enriched $^{20}Ne$ were used in all of our high-energy-resolution studies of $^{20}Ne(p,p)^{20}Ne$. These targets and the means by which they were made are described at length in section 2.2. For purposes here, the targets were 20- to 50-$\mu g/cm^2$-thick foils of carbon and aluminum with a tiny amount (.3 to 2.4 $\mu g/cm^2$) of $^{20}Ne$ concentrated near the aluminum surface, which faced the incident beam. The foils were mounted on target rings which were affixed to a target rod that lowered through O-ring seals into the scattering chamber.

Target thicknesses were measured by performing forward-angle proton and/or $\alpha$-particle scattering at low energy, and comparing the scattering yields with calculated Coulomb cross sections. The targets used for acquisition of the data presented here had $^{20}Ne$ thicknesses of 2.3 and 2.4 $\mu g/cm^2$.

The absolute normalization uncertainty in high-resolution cross-section data is estimated to be 14 percent. This figure results from addition-in-quadrature of a 10 percent uncertainty in the determination of target thickness and a 10 percent uncertainty in beam integration during scattering experiments.

The absolute normalization uncertainty in analyzing-power data is estimated to be 10 percent and attributable largely to uncertainty in spectrum background subtraction. During data acquisition, the beam

polarization was found to vary by, at most, $\pm$ 3 percent. This variation has a negligible effect on ramp-excitation data, however, since it is averaged, in those data, over all data points equally, and since the average beam polarization was determined by integrating beam scattered in the polarimeter during the entire run.

During early test runs with a preliminary batch of targets, we encountered problems with carbon buildup, which presumably resulted from the cracking of oil vapors in the beamline and scattering chamber under beam heating of the target foil. We installed a liquid-nitrogen trap in the beamline between the scattering chamber and the nearest diffusion pump. Subsequently, we found only very minor visible evidence of carbon buildup on foils when the chamber was opened after an experiment. (The scattering chamber was evacuated by a turbo-molecular pump and the direct roughing-pump line was equipped with a liquid-nitrogen trap. We therefore expected, and evidently got, very little oil vapor from pumps local to the chamber.)

### 3.3.4 Chamber configuration

The chamber configuration used in acquiring both step- and ramp-excitation data is shown in figure 3.6. Pairs of similar detectors were placed symmetrically about the axis defined by the beam direction to lessen the effects of geometrical errors on the analyzing power extracted from scattering yields in those detectors. Detector pairs were placed at laboratory angles of 52.4, 122.9, 145, and 165 degrees (see table 3.3).

| angle (deg) | slits (mm) horiz. | slits (mm) vert. | distance (cm) |
|---|---|---|---|
| 52.4 | 6.35 | 12.7 | 12.7 |
| 122.9 | 6.35 | 12.7 | 10.2 |
| 145.0 | 6.35 | 12.7 | 7.62 |
| 165.0 | 6.35 | 12.7 | 7.62 |

Table 3.3. Detector (laboratory-frame) angles, slit sizes, and distances from target to front slit.

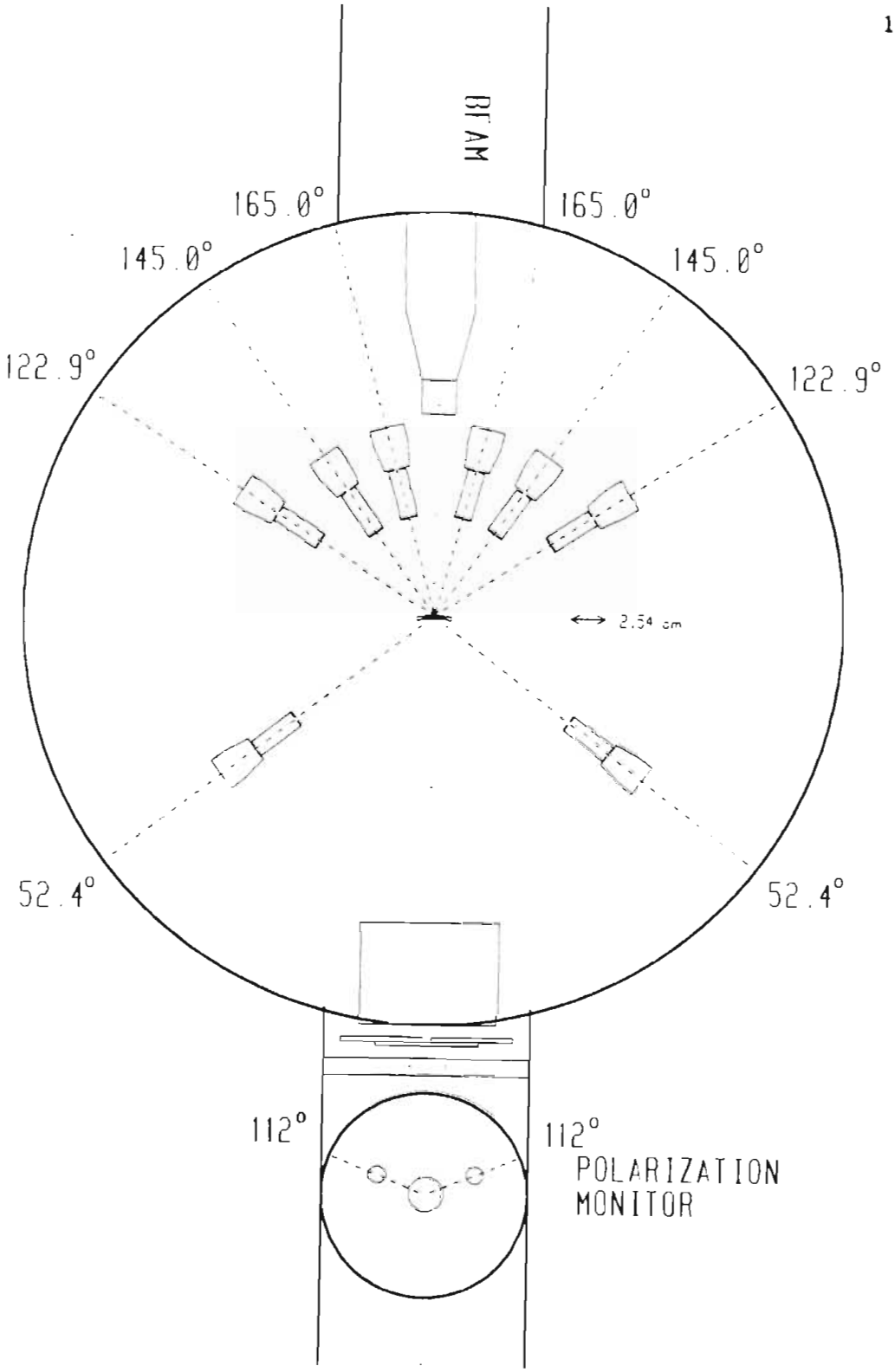


Figure 3.6 The chamber configuration for high-energy-resolution scattering experiments.

The detector angles of 52.4 and 122.9 degrees were chosen to correspond with zeros of Legendre polynomials. The angle of 165 degrees was the most backward angle practical with the chosen detector solid angles: at more backward angles, an unacceptable amount of scattering from chamber and beamline surfaces far downstream from the target rod was intercepted by the detectors.

Detector solid angles were chosen to minimize differences in the count rates of detector pairs at different angles so that the larger yields from detectors at more forward angles would not swamp the data-acquisition electronics and data-sorting software. In effect, this choice places a higher priority on data from detectors at more backward scattering angles.

There is some theoretical and practical justification for this placement of priority. For scattering of spin-1/2 particles on a spin-0 target, the differential cross section $\sigma$ for scattering at any particular angle can be written [Wil82]

$$\sigma = |a_{nr}|^2 + |b_{nr}|^2 + |a_R|^2 + |b_R|^2 + 2 \cdot \mathrm{Re}[a_{nr} a_R^* + b_{nr} b_R^*]$$

where the subscripts "R" and "nr" denote resonant and non-resonant quantities, respectively; and "a" and "b" are, respectively, the spin-flip and non-spin-flip scattering amplitudes. Even though the resonant contributions to $\sigma$ are enhanced by interference with non-resonant scattering amplitudes, the resonant amplitudes can never dominate $\sigma$ unless they are larger than the non-resonant amplitudes. For cross-

section data, the term to beat is $a_{nr}$, which contains the Coulomb amplitude and which falls off quickly at backward angles. Thus, at backward angles, resonant amplitudes typically constitute a larger fraction of the total cross section.

Given this, a practical reason for preferring step-excitation data from backward angles is that such data are typically less severely affected, than are forward-angle data, by errors in normalization that vary from energy to energy in an excitation function. A variation in scattering yield of a few percent--due, for example, to beam wandering on a slightly nonuniform target--makes a small difference in the resonance shape observed at an angle where the scattering is mostly resonant, but utterly destroys the shape observed at another angle where resonant scattering is only a small fraction of the total scattering.

The above arguments apply also to analyzing-power data, but with less force since there is no purely resonant contribution to the analyzing power: resonance effects in the analyzing power are entirely due to interference between resonant and non-resonant amplitudes as can be seen from the following expression [Wil82] (in which $a_R b_R^*$ is purely real and therefore makes no contribution).

$$\sigma \cdot A_y = 2 \cdot \mathrm{Im}[a_{nr} b_{nr}^* + a_{nr} b_R^* + a_R b_{nr}^* + a_R b_R^*]$$

Also, the arguments in favor of backward-angle data are much less applicable to ramp excitations (of either cross section or analyzing

power) than to step excitations since most time-dependent normalization errors are averaged over all points of an excitation function by the ramp. (However, as discussed in section 2.1.5, effects due to normalization errors that are correlated in time with the target ramp are not distributed equally among the data points.)

### 3.3.5 Step excitations

Using the TUNL energy-stepping system described in chapter 2, step excitations of cross section and analyzing power were acquired over energy regions some 50 keV in width that included the two lowest-energy T = 3/2 resonances. These data precisely located the resonances for application of the target-ramping system and also provided a normalization check for ramp-excitation data. In addition, step-excitation data from nearby non-resonant energy regions above and below the resonance were to be used in the analysis of ramp-excitation resonance data.

### 3.3.6 Ramp excitations

Ramp excitations were acquired by holding the beam energy fixed and varying the voltage applied to the target rod, as described thoroughly in section 2.1.5. The procedure typically employed follows: the resonance of interest was located in a step excitation; the analyzing-magnet system was recycled to remove hysteresis effects from its energy calibration; the magnet was set for a beam energy several keV below the resonance energy and the target voltage ramp was turned on; and the resonance was centered in the ramp scan by varying the

setting of the analyzing magnet.

After centering the resonance, scattering data were simply accumulated until the desired statistical precision had been reached. If several hours were required for this, data were dumped periodically to permanent storage to defend those data from the next computer crash.

Since, in a ramp-voltage excitation, scattering events with many different effective beam energies are acquired in a single run, the data structures used by event-sorting software are more complex than those used in acquisition of step-excitation function data. As in step-excitation-function event sorting, scattering events are binned according to ejectile energy into one-dimensional histograms, or spectra, which consist of peaks corresponding to the various excitations of the residual nucleus. But with ramp-excitation data, this is only the first step in the event-sorting process.

In the ejectile-energy spectrum, an energy region of interest is specified by the experimenter, using an XSYS one-dimensional gate. Scattering events that are binned into this region of interest are also binned into two-dimensional histograms, the additional dimension corresponding to effective beam energy as parameterized by the target-voltage-ramp step number. (See section 2.1.5.) The result of this portion of the event sorting is a set of "bites" of the ejectile-energy spectrum, one for each ramp step, that corresponds to the many XSYS data areas that would be collected in many different runs

with the ordinary, step-excitation, event-sorting software.

In practice, the binning of scattering events into both one- and two-dimensional histograms is conditional: normally, the experimenter will have one or more additional histograms allocated to event parameters used to reject scattering events that occurred, for example, when the NMR-magnetic-field error signal was outside of a preselected range. In a typical use of this feature, the NMR error signal is binned periodically (at the rate of a few hundred Hz., triggered by an external oscillator) into its histogram, and the experimenter has set an XSYS gate in this histogram specifying the allowable range of the error signal. The event-sorting software checks the most recent NMR "event" against this range before binning a scattering event.

Conditional event sorting was used extensively in the early stages of this research project, especially during development of the Beamline Monitor System (described in section 2.1.3), to determine the source of suspected energy deviations. (See section 2.1.2.) Of the signals tested, only the NMR-error signal was found consistently to be useful as an indicator of beam-energy deviations. However, the recently acquired Scanditronix NMR is stable enough that, in normal operation, conditional sorting on its value yields a negligible improvement in observed resonance widths. However, conditional event sorting on the NMR error signal is helpful during the "ramp-ramp" measurement of the beam resolution function, described in section 2.1.6, since that system perturbs the analyzing-magnet power supply as it steps the

field in the downstream magnet--a perturbation that shows up in the error signal.

### 3.3.7 HSYS: offline calculations

Preliminary data analysis, the conversion of scattering yields to cross section and analyzing power, is performed by HSYS, a package of private XSYS programs described in section 3.1.6. Although the calculations described in that section apply specifically to step-excitation data, and although ramp-excitation data structures are different from those used for step-excitation data, the manner in which HSYS is used to calculate scattering observables from ramp-excitation function data is quite similar.

In applying HSYS to ramp-excitation data, advantage is taken of the XSYS' low-level implementation of a two-dimensional data area, or histogram, as a simple linear array. When viewed in this way, the two-dimensional histogram, which contains M instances (one per ramp step) of an N-channel-wide spectrum "bite", is seen simply as M one-dimensional data areas, each N channels wide, laid end to end. HSYS is used, on this extremely long spectrum, exactly as it was used on the individual spectra in section 3.1.6.

# 4. Data analysis

## 4.1 General remarks

Preliminary data analysis--the calculation of cross section and analyzing power from raw scattering yields--having been performed by the HSYS routines, we are left with excitation functions exhibiting the interference between resonant scattering amplitudes and the constant or slowly varying nonresonant amplitudes. In the analysis of the $T = 1/2$ resonances, the nonresonant amplitudes are viewed as the result of scattering from the nuclear potential without significant compound-nucleus formation. In the analysis of the relatively very narrow $T = 3/2$ resonances, compound-nucleus scattering through $T = 1/2$ states is seen over such a narrow energy range that it may be approximated as constant and lumped together with the nonresonant potential scattering. In both cases, we are concerned primarily with determining, from the data, parameterizations of the resonances that produce local excursions in the data.

The quantities in which we are most keenly interested are essentially energy widths: the resonance width $\Gamma$, and the related partial width $\Gamma_p$. For this reason, limitations of our measuring instrument that spread the observed effect of the resonance over a wider energy range than it naturally occupies must be accounted for in the analysis.

In short: knowledge of the energy resolution function is critically important in the analysis because its effect mimics the effect we seek to quantify.

However, the resolution function's effect does not mimic the resonance perfectly, but differs in two significant ways: it has, generally, a different shape than the (Breit-Wigner approximation of a) compound-nucleus resonance, which is Lorentzian; and its normalization is fixed, while the normalization of the Lorentzian distributions that represent the resonance depends on the parameter $\Gamma_p$ which we hope to determine.

## 4.2 Energy-loss and -straggling calculations

In the analysis of both low- and high-resolution excitation-function data, the energy loss suffered by incident-beam particles prior to their scattering in the target is significant. Energy-loss effects for the analyses summarized in this thesis were calculated using the computer program STRAGL [Cla71], and the routine ENLOSS (called "ELOSS" in [Cla71]), which is included in STRAGL but also used separately of it.

There are two effects of energy loss in the target that are important in the analysis of resonance data: the mean energy loss, and the straggling about that mean. Straggling always contributes to the target energy-resolution function, while the mean energy loss may or may not contribute, depending on whether or not it occurs within view

of the detectors. If the beam suffers an energy loss before arriving at the target, for example, the effect of the mean energy loss on any observed resonance is simply to change the apparent resonance energy, while the effect of the accompanying energy straggling is to broaden the observed resonance. But if the beam suffers an energy loss in a region containing target nuclei that is visible to the detectors, the incident energy of beam particles scattered from the upstream end of the target will differ systematically from that of beam particles scattered from the downstream end. Therefore, in this case, the mean energy loss acts together with energy straggling to broaden the observed resonance, and both effects must be accounted for in the target resolution function.

STRAGL calculates the energy-loss distribution (the mean energy loss as well as the straggling about the mean) of an initially monoenergetic beam that has completely traversed an absorber; ENLOSS calculates the mean energy loss for the same case. While, in principle, the calculations can be done independently, STRAGL uses the results of ENLOSS both for mathematical convenience and for greater accuracy: ENLOSS calculates only a single moment of the energy-loss distribution and, freed from the mathematical baggage required to calculate several moments at once, can practically use more correct approximations than are used in STRAGL.

ENLOSS calculates the rate dE/dx of projectile energy loss as a function of distance travelled through an absorber, and numerically

integrates this function, dividing the absorber into regions of small energy loss. The rate is calculated using the relativistically correct Bethe formula [Bet53] which describes energy loss caused by collisions with absorber electrons modelled by the continuous electron distribution of the Thomas-Fermi atom. In the Bethe formula, electron binding-energy corrections to the energy loss are calculated using a mean ionization potential.

STRAGL implements the Landau [Lan44] and Vavilov [Vav57] formulas for the energy-loss distribution of a monoenergetic beam of particles completely traversing a thin absorber, and includes the modification to the Vavilov formula by Schulek et al. [Sch67], which addresses the fact that electrons in the absorber are bound.

The Landau and Vavilov formulas are derived from analytic solutions of a transport equation, solutions which are mathematically complicated and the discussion of which would be correspondingly involved. However, the underlying physics can be isolated for discussion in relatively simple terms by noting that the transport equation serves essentially as a vehicle for the function w(E), the differential cross section for collisions with an energy loss E (i.e., between E and E+dE). The approximations that facilitate analytic solution of the transport equation are made, for the most part, to w(E), or to the limits of definite integrals involving it. The difference between the Landau and Vavilov solutions stems entirely from a difference in the function w(E) used. The Shulek modification, however, although it attempts to

correct a defect in the w(E) used by Vavilov, cannot be discussed in these terms.

Both Landau and Vavilov assumed that all electrons in an absorber are free and at rest. Both implemented a cutoff in the function w(E) at the energy $E_M$, the maximum energy transferable kinematically to an electron in a single collision, using an approximate $E_M$ valid for beam particles much more massive than electrons. Vavilov's w(E) is continuous across $E_M$ (in the limit v/c -> 1, where v is the projectile velocity); Landau's is not, but drops from a finite value to zero at $E_M$. Finally, although an arbitrarily small energy transfer to bound electrons is unphysical, since neither Landau nor Vavilov considered bound electrons, neither implemented a low-energy cutoff in w(E).

Limits of validity of the Landau and Vavilov formulas, of the modifications made to them, and therefore of STRAGL are difficult to determine exactly [Cla71], since they depend in a complicated way on the thickness, bombarding energy, and atomic number of the target. More exact calculation of straggling distributions has been done ([Bic74], [Jar77]) for aluminum and silicon absorbers. Comparison of these distributions with those calculated by STRAGL indicates that STRAGL fails badly when the quantity ($K E_M$) (see below) that it calculates is very small compared to the K-shell binding energy of the absorber. An approximate inequality for validity at the 25 percent level is given by [Jar77]:

$$K\,E_M > 1/6\,I_K, \qquad (4.1)$$

where K is the value KAPPA, which is printed by STRAGL; $E_M$ is the maximum kinetic energy transferred to an electron in a single collision, also printed by STRAGL; and $I_K$ is the K-shell ionization energy of the absorber. The following approximations (from [Jar77] and [Bic74]) may be helpful in applying formula (4.1) to a particular beam/target combination:

$$K = 33076\ \frac{z^2}{A}\frac{Z}{E^2}\frac{t}{} \quad \text{(dimensionless)}; \qquad (4.2a)$$

$$E_m = \frac{2\,mc^2\,\beta^2}{1-\beta^2} \quad \text{(MeV)}; \qquad (4.2b)$$

$$I_K = 13.6\ Z^2 \quad \text{(eV)}; \qquad (4.2c)$$

where z is the projectile charge number, A and Z are the target atomic mass and charge numbers, t is the target thickness in $g/cm^2$, E is the kinetic energy of the projectile in MeV, $mc^2$ is the electron mass in MeV, and $\beta$ is the projectile speed as a fraction of c.

Application of formula (4.1) indicates that STRAGL fails in every case of interest for the analysis of low-energy, high-resolution scattering data, since these data are acquired using very thin targets. But the way STRAGL fails for thin absorbers is interesting and suggests that the failure does not pose a wholly insurmountable problem in the analysis of thin-target data. In the more exact straggling calculations of [Bic74], the predominant energy-loss mechanism for thin absorbers is plasmon excitation--collective excitation of valence electrons in

which an approximately quantized energy, the plasmon energy, is transferred. As a result, the straggling distribution consists of a spectrum of peaks of varying heights at multiples of the plasmon energy. For thin targets, STRAGL calculates a Landau function which fails utterly to reproduce the spectrum of peaks, but which fails in a much milder way to reproduce grosser details of the distribution, notably the mean energy loss.

That STRAGL produces a smooth straggling distribution, rather than a spectrum of peaks, for thin targets does not by itself imply that STRAGL cannot contribute to meaningful calculations of the *total* resolution function required to analyze thin target, excitation-function data; the peaks would not, in any case, survive convolution with any realistic beam-resolution function. Also, the target resolution function by itself is dominated by the mean energy loss (see section 4.5.1), which is calculated by STRAGL in much more nearly correct a fashion than are the higher moments of the energy-loss distribution. This is true approximately to the extent that the FWHM of the energy-loss distribution is less than its mean. A rule-of-thumb is given in [Jar78]: "The full-width-half-maximum (FWHM) energy spread is 10% to 20% of the mean energy loss in the Gaussian region (fairly thick targets) ... and rises to 20% to 30% FWHM for thin targets (Landau region)."

STRAGL is clearly not the ideal calculational tool with which to estimate energy straggling for the high-resolution scattering experiments described in this thesis. More exact straggling calculations can

be made in specialized cases, such as the case [Bic74] of a simple, one-element target of a well-studied material. But such calculations cannot, as yet, be made for the more complicated ion-implanted targets used in the experiments described here. Accordingly, we use STRAGL simply because it is the best tool available.

By accepting STRAGL's limitations, we introduce error into the calculation of the total resolution function. We are most concerned with the error introduced into the analysis of narrow-resonance data because they are acquired with thin targets and (for us) it is with thin targets that STRAGL's calculation is suspect. Some feeling for the seriousness of this error can be had by comparing the width (FWHM) of the energy-loss contribution, calculated using STRAGL, with the width of the beam-resolution function and with the natural width of the resonances to be studied. We will see that the energy-loss contribution is approximately of width 200 eV; the beam-resolution function is unlikely to be much less than 500 eV in width; and the natural width of the narrowest observed resonance to be studied here has been determined previously to be in the vicinity of 750 eV. Since these widths add, roughly, in quadrature to produce the observed resonance width, the effect of even a substantial error in STRAGL's calculation has relatively minor consequences for the analyses of data in this thesis.

## 4.3 Analysis of low-resolution resonance data

The energy-resolution function used in analysis of the relatively

low-resolution gas-cell data is dominated by energy loss in the target: in this case the beam and Doppler-broadening resolution functions are of relatively negligible width (approximately 1000 eV and 300 eV, respectively, while we'll find the energy-loss width to be approximately 10 keV). However, in this case we are not concerned with the limitations of the STRAGL calculation discussed in the last section because STRAGL has been shown to produce accurate straggling distributions in cases similar to this one. Also, we'll see that the energy-loss contribution to the resolution function is dominated by the mean energy loss, rather than by straggling about the mean.

### 4.3.1 The gas-cell resolution function.

For the purpose of calculating the resolution function, the beam path through the cell can usefully be divided into three regions: the entrance foil; the first 0.5 cm of gas encountered by protons traversing the cell; and the next 1 cm of gas--from which scattered beam can enter the detectors (see fig. 4.1). In the first two regions, contributions to the resolution function come entirely from energy straggling and are independent of mean energy loss as a function of distance along the beam path. In the third region, the mean energy-loss function also contributes because this region is visible to the detectors.

Energy straggling in the first two target regions was calculated using the computer program STRAGL [Cla71], described above, which calculates the energy-loss distribution of an initially monoenergetic

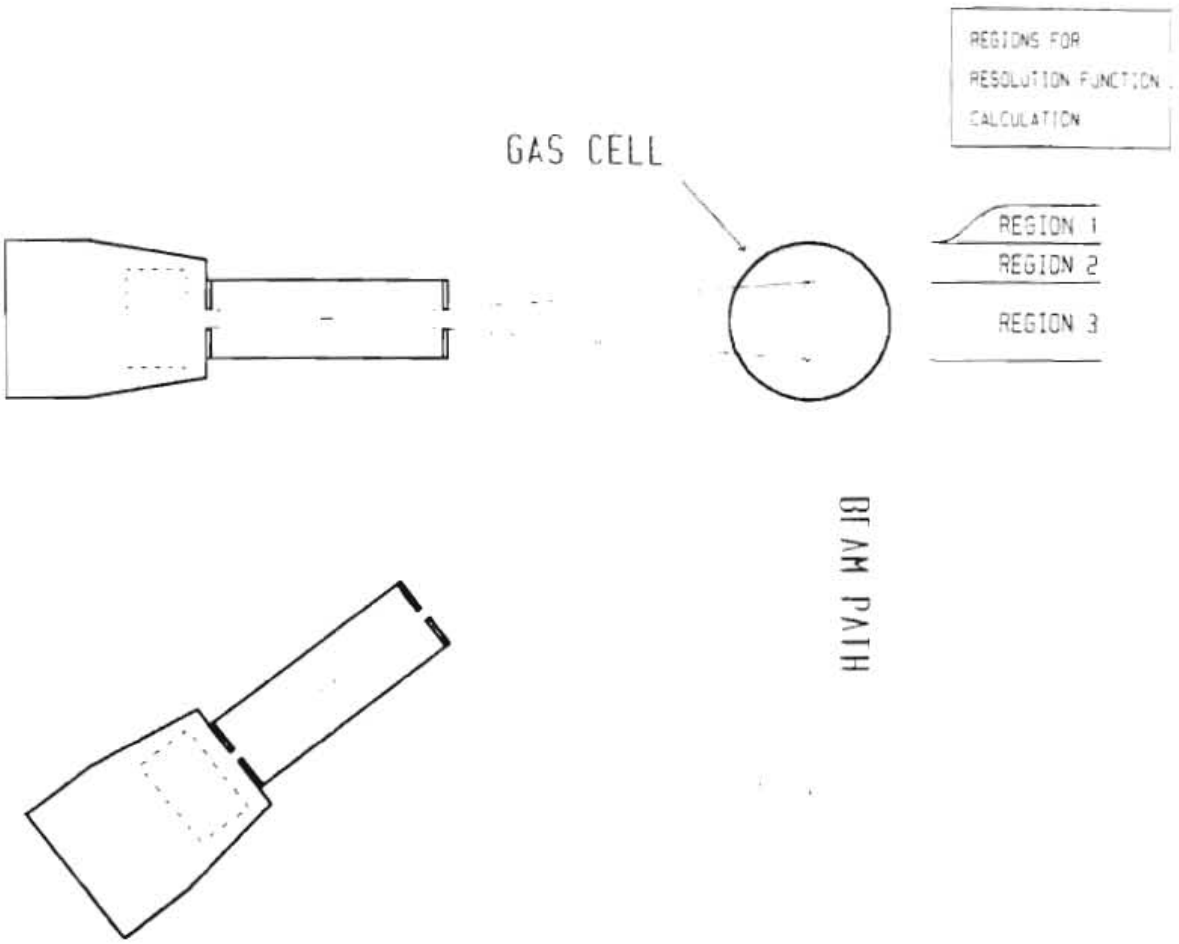


Figure 4.1 The region of the gas-cell target that is visible to the detectors.

beam after completely traversing an absorber.

For region 1, the straggling distribution calculated by STRAGL was nearly Gaussian, with a FWHM of 29.5 keV. For region 2, STRAGL yielded a strongly asymmetric distribution for which the FWHM of 2.85 keV conveys little more than a sense of scale (see fig. 4.2). The energy-loss distributions for the two regions were convoluted together yielding, in the approximation of an initially monoenergetic beam, the beam-energy distribution at the upstream end of region three of the target, the region visible to the detectors.

The calculation that yields an energy-resolution-function contribution from region 3 of the target begins by dividing this region into equal "slices" normal to the beam direction (see fig. 4.3). One assumes the scattering probability is the same in all slices, carefully ignoring variations in scattering probability with energy because it is an *energy* resolution function that is desired as an end product. (Greater accuracy can be attained by replacing this assumption with a calculation of the detector solid angle as a function of beam-path length through the gas cell. The normalized solid-angle function, evaluated at a representative point within each target slice, is the relative efficiency with which the slice is seen by the detectors. This efficiency can be folded into the resolution-function calculation by renormalizing the representative energy-loss distributions.) A representative energy-loss distribution is calculated for each slice assuming an initially monoenergetic beam which has travelled from the upstream end of the

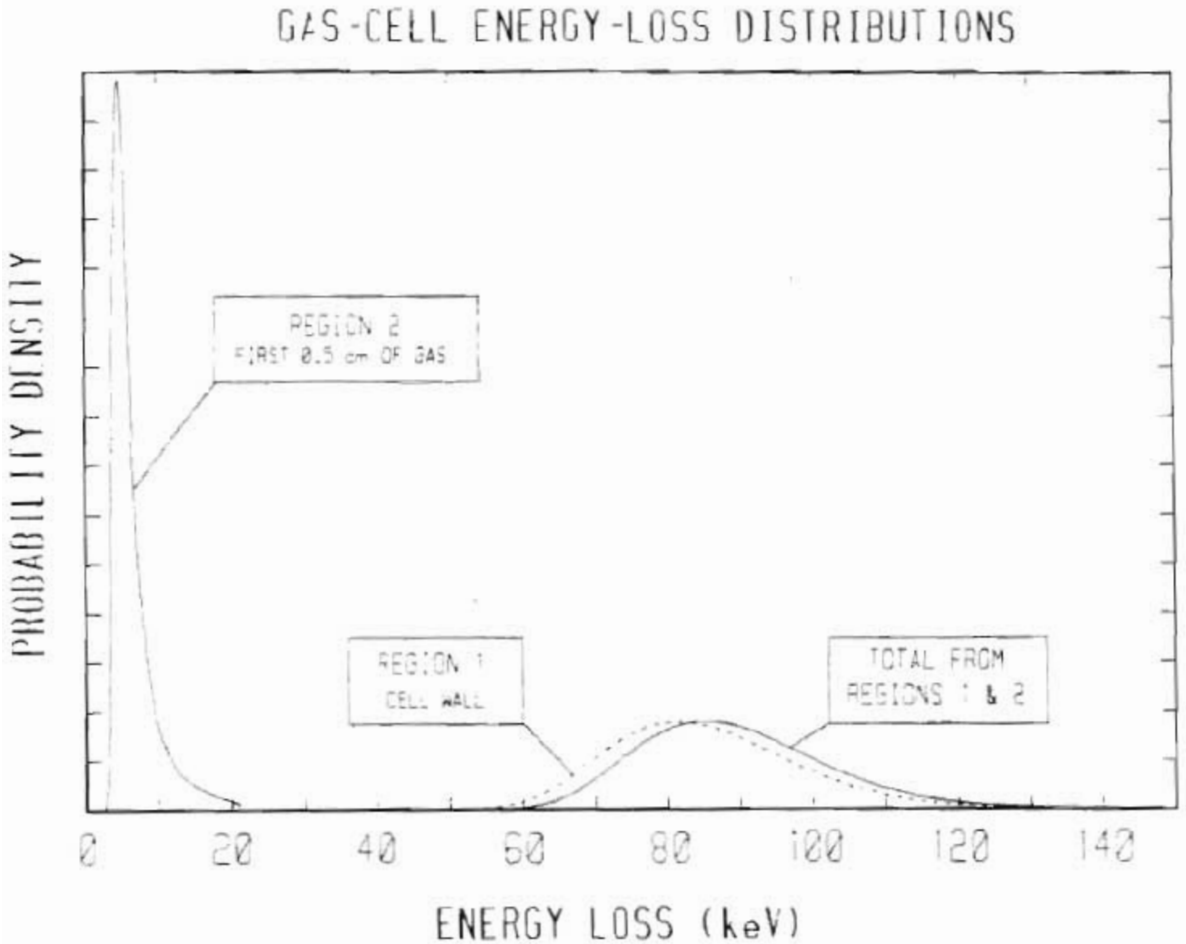


**Figure 4.2** Gas-cell straggling/energy-loss distributions.

region to the midpoint of that slice. Here, one assumes that all scattering from a given slice is scattering of incident particles drawn from the representative distribution; in principle, this assumption can be made as valid as one would like by dividing the region into fine enough slices.

Given a representative energy-loss distribution for each slice of the region, the resolution-function contribution is the simple sum of the distributions. The computer program TS, which performs the calculations described above, has been written for the Amiga computer. The program borrows heavily from the programs STRAGL and CSTRAGL [Wil82]. Results of the actual calculation are shown in the inset of figure 4.3.

The total target resolution function is calculated by convoluting together the contributions from all three regions. Figure 4.4 shows the contributions from the visible and non-visible regions of the target along with the total target resolution function. This last is also the total resolution function since the beam resolution function is relatively negligible (estimated width: less than 1.2 keV).

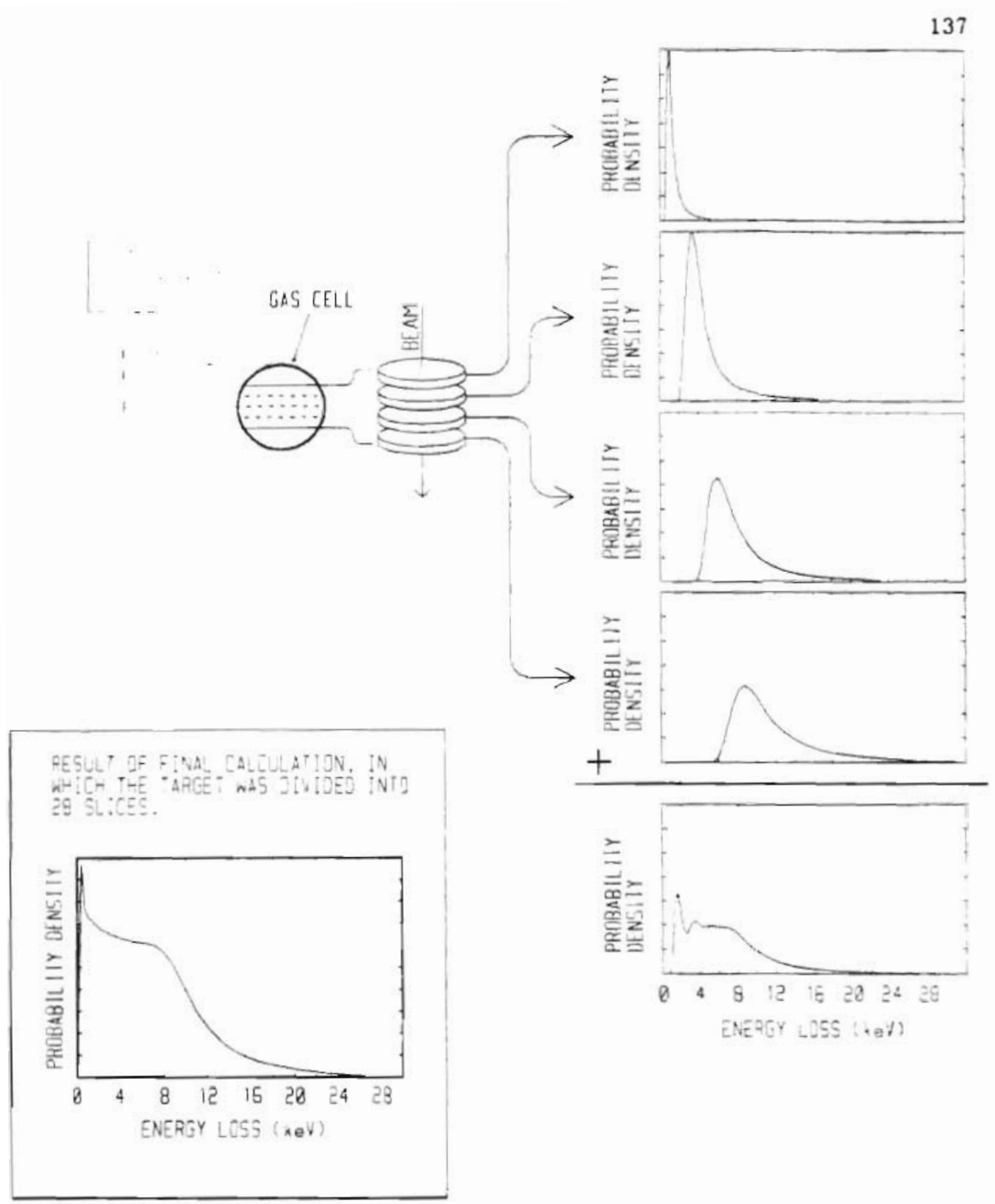


Figure 4.3 Sample calculation of the target resolution function contribution from the region visible to the detectors.

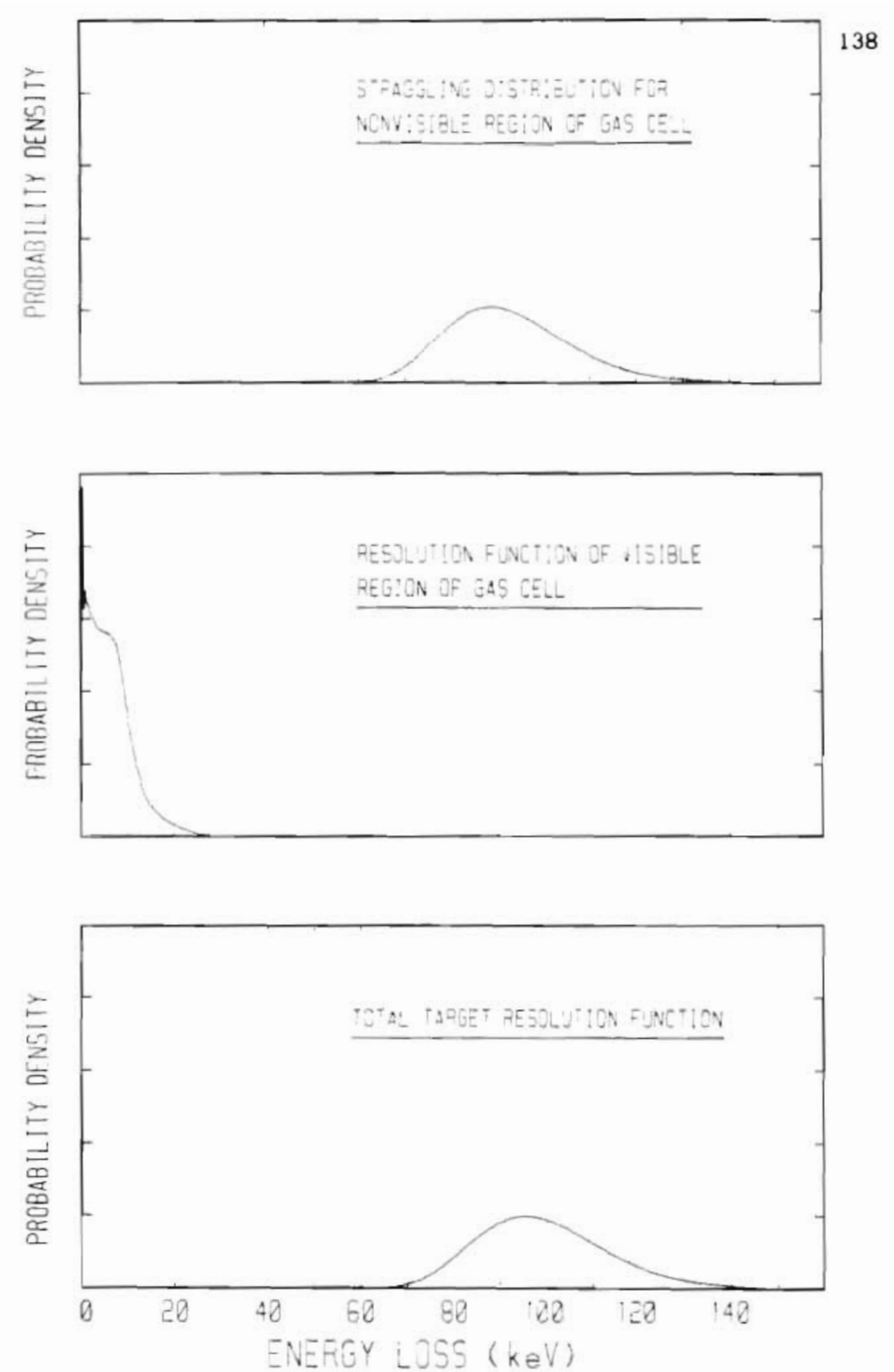


Figure 4.4 The total gas-cell target resolution function.

### 4.3.2 Theory

The differential cross section and analyzing power for elastic nuclear scattering of a spin-1/2 projectile on a spin-0 nucleus can be written [Tho68]:

$$\frac{d\sigma}{d\Omega} = |a|^2 + |b|^2 \qquad (4.2a)$$

$$\frac{d\sigma}{d\Omega} A_y = 2\ \mathrm{Im}(ab^*) \qquad (4.2b)$$

where a and b are the non-spin-flip and spin-flip nuclear scattering amplitudes, respectively. The amplitudes a and b, functions of the scattering angle $\theta$ and projectile energy E, can be seen as resulting from several conceptually distinct elastic-scattering processes: scattering of a plane wave, representing the beam, from the Coulomb ("a" only) and nuclear potentials of the target nucleus; and absorption of the projectile by the target nucleus--formation of a compound nucleus from which the projectile, or a particle identical to it, is later emitted.

The compound-nucleus process is of particular interest here; indeed, the purpose of the scattering experiment is to discover in what states the compound nucleus can exist. We hope to discover this by analyzing the angle and energy dependence of the cross section and analyzing power--playing "What if...?" by positing different combinations of states, modelling the scattering from those states, and comparing results of the model calculations with observed data.

Expressions for the scattering amplitudes a and b are given by the following formulas from [Tho68] and [Ada66]:

$$a = f_c + \frac{1}{k} \sum_L \sum_J [(j+1/2)\ \alpha^L_{J-L}\ e^{2i\omega_L}\ P_L(\cos\theta)] \qquad (4.3a)$$

$$b = \frac{1}{k} \sum_L \sum_J [(-1)^{J-L-1/2}\ \alpha^L_{J-L}\ e^{2i\omega_L}\ P^1_L(\cos\theta)] \qquad (4.3b)$$

where $f_c$ is the Coulomb scattering amplitude, k is the wave number, L and J are respectively the orbital and total angular momenta, $\omega_L$ is the relative Coulomb phase, $P^m_L$ are associated Legendre polynomials, $\theta$ is the C.M. scattering angle, and $\alpha^L_{J-L}$ are nuclear scattering amplitudes which contain the effects of both nuclear-potential and compound-nucleus scattering. The sum over L runs from zero to the maximum orbital angular momentum, about the center-of-mass of the target-projectile system, consistent with a collision involving the two nuclei. The index J runs over $J = L \pm 1/2$, with the restriction that it be positive.

If a single, isolated compound-nucleus state of angular momentum J contributes to L-wave scattering from the nucleus, the nuclear scattering amplitude for that channel can be written as follows ([Tho68], [Ada66]):

$$\alpha^L_{J-L} = \alpha^{0L}_{J-L} \left[1 + ie^{2i\phi^R_c} \frac{\Gamma_p}{E_r - E - i\Gamma/2}\right] + \frac{1}{2} e^{2i\phi^R_c} \frac{\Gamma_p}{E_r - E - i\Gamma/2} \qquad (4.4)$$

where $\alpha^{0\,L}_{J,L}$ would be the amplitude in the absence of compound-nucleus formation; $E_r$, $\Gamma$, and $\Gamma_p$ parameterize a Breit-Wigner approximation of the compound-nucleus scattering amplitude; and $\phi^{R}_{c}$ is the relative phase between the two scattered waves. (This equation ignores the possibility that two or more compound-nucleus states of the same spin and parity can contribute to scattering in overlapping energy regions.)

Each of the scattering amplitudes (the $\alpha$'s) can be rewritten in terms of a complex phase shift or, as shown below, in terms of the real part $\delta$ of that phase shift, and a real parameter $\gamma$ related to the imaginary part $i\eta$.

$$\alpha^{L}_{t\,1/2} = \frac{1}{2i}\left[\gamma^{t}_{L}\ e^{2i\delta^{t}_{L}} - 1\right]; \qquad \gamma^{t}_{L} = e^{-2\eta^{t}_{L}} \tag{4.5}$$

The quantities $\delta$ and $\gamma$ are called *phase-shift parameters*; as search parameters they are preferable to scattering amplitudes because it is easy to specify the range of values for them that are consistent with unitarity and to constrain them within that range. Any complex phase shift is physically admissible; therefore, $\delta$ needs no constraint at all, and $\gamma$ must be constrained to the [0 ... 1] range of the exponential function. In contrast, the equivalent constraint on, e.g., the real part of the scattering amplitude $\alpha$ is an equation also involving the imaginary part of that amplitude. Such a coupled constraint would be difficult to implement with the parameter-search program we have chosen to use.

### 4.3.3 Modelling the scattering process

The essential quantities necessary to model the scattering of a spin-1/2 projectile of energy E from a spin-0, stationary, isolated target nucleus have now been related to observables of an actual scattering experiment (ignoring, for the moment, such nasty realities as resolution functions). The remaining task is to choose values, for the various quantities described above, that are physically admissible and that reproduce the data.

The task of choosing those values is computationally very expensive: there are a *lot* of choices to be made and evaluated. Some numbers: assuming that only scattering channels characterized by orbital angular momentum L of 4 or less need be considered, 7 complex phase-shift parameters (the $\alpha$'s) are required to describe nuclear-potential scattering (at each energy, but let's assume nuclear-potential scattering is "locally" energy independent); for each contributing compound-nucleus state, 6 additional real parameters ($E_r$, $\Gamma$, $\Gamma_p$, $\phi$, $L_r$, and $J_r$) are required. A set of data that includes three resonances, then, is fit with 32 real parameters. If only 3 values for each parameter were possible, $3^{32}$ evaluations would be required to exhaustively search the parameter space. At the optimistic rate of 1000 evaluations per second, such an exhaustive search would require some 58,000 years.

Traditionally, the number of parameters simultaneously considered is minimized by initially fitting angular-distribution data from a single

energy using the total nuclear amplitudes (i.e., by not separating nuclear-potential scattering from compound-nucleus scattering). When a set of these amplitudes that fits the data has been found for each energy, the amplitudes that exhibit resonant behavior are fit, as functions of energy, using Breit-Wigner parameterizations. In this way, the fitting problem is divided into two simpler problems, the first of which is referred to as a *phase-shift analysis* because phase shifts, rather than the equivalent amplitudes, are normally used as search parameters. This two-step approach was used, e.g., in [Mos65], [Mey76], and in a previous analysis [Fer81] of $^{20}$Ne(p,p)$^{20}$Ne data.

The two-step process is very well motivated by the daunting prospect of minimizing in a parameter space of very many dimensions (in the naive example given earlier, a reduction from 32 parameters to 14 would decrease the "exhaustive-search" time from 58,000 years to 80 minutes). However, the method has a problem whose effect on extracted resonance assignments is unclear: at no time in the analysis are resonance parameters actually fit to data. Phase shifts are fit to data--a fit which normally is very good, possibly because the number of parameters (typically 14 or so) approaches the number of data points (typically 30 or so); resonance parameters are fit to those phase shifts.

Since phase-shift parameters are the only quantities that ever "see the data" in the two-step method, one would like somehow to constrain them so that they behave always in ways not only physically

admissible, but also consistent with their describing resonant-plus-nuclear-potential scattering. That is, one would like to constrain their energy-dependence in some physically meaningful way--without introducing additional parameters. This may not be possible; certainly I have found no way of doing this.

### 4.3.4 The program PSF

#### 4.3.4.1 General remarks

The program PSF implements the equations described above to calculate cross section and analyzing power from a set of phase-shift and resonance parameters, and compares the calculated results with scattering data. As noted above, much more is involved in fitting data with a set of parameters: to determine the set of parameter values that best fits the data is the task of a minimization program called MINUIT [Jam75].

#### 4.3.4.2 MINUIT

MINUIT is a package of Fortran routines that, as a whole, attempts to minimize the value of the function of a user supplied set of parameters by trial-and-error variation of the values of those parameters. One routine is special and customizes MINUIT to a particular application: the MINUIT user writes a routine, called FCN, that accepts an array of parameter values from MINUIT and returns a single number by which MINUIT judges its success in selecting parameter values.

As might be expected, much of the code in MINUIT is given over to the relatively uninteresting "housekeeping" tasks involved in accepting and manipulating the sets of parameter values. Also, much of a MINUIT user's attention is directed at the set of commands by which MINUIT is driven, and at the interaction between MINUIT proper and the routine FCN. Neither of these subjects will be discussed here at length. The interested reader is referred to [Jam75] and [Var86].

From MINUIT's point of view, our problem of fitting data with a set of parameters is an equivalent problem of discovering the lowest point on the hypersurface that is a function of those parameters. This function is returned to MINUIT by the routine FCN as a single value for each set of parameter values passed from MINUIT to FCN. In our case, the value returned by FCN is the chi-square goodness-of-fit $\chi^2$ between experimental data and the curve(s) generated from the passed parameters. The goodness-of-fit function is defined as follows:

$$\chi^2 = \frac{1}{N_d} \sum_i \frac{(d_i - g_i)^2}{(\Delta d_i)^2}, \qquad (4.6)$$

where $N_d$ is the number of data points compared with calculation, $d_i$ is the $i^{th}$ data point, $g_i$ is the corresponding calculated value, and $\Delta d_i$ is the uncertainty in the value--the error bar--of the $i^{th}$ data point. The complicated, nonlinear dependence of $\chi^2$ on the fit parameters is not evident here; it derives, of course, from the dependence of $g_i$ on those parameters.

MINUIT uses one of three different algorithms in attempting to find the lowest value of $\chi^2$: a Monte Carlo search ("SEEK"), a simplex minimization ("SIMPLEX"), and a variable-metric, gradient minimization ("MIGRAD"). In SEEK, parameter values are varied (within their user-specified limits) pseudorandomly about the best-fit parameter set, which is continually updated as better fits are found. The other two algorithms, SIMPLEX and MIGRAD, are similar to each other, and different from SEEK, in that they attempt to better the current best-fit parameter set by searching locally around it. However, SIMPLEX and MIGRAD differ from each other in the way they perform this local search.

The simplex method can probably be more efficiently explained by analogy than by definition. In a two-dimensional parameter space, a simplex moves as a three-legged beast, each of whose legs can swing completely through the plane defined by the other two, would walk through uneven terrain. The beast has no notion of where it has been, nor to where it is going; it knows only that, at each point, one leg swings more nearly in the direction that takes it downward than do the other two. The simplex "beast" always steps with this leg, whichever it may be.

The more highly evolved three-legged beasts adaptively adjust the spacing of their feet and the length of their strides to the conditions on the ground beneath them. On smoothly sloping terrain the beasts take giant steps; in close quarters they tiptoe. Nevertheless, even

highly evolved simplex beasts are clumsy almost beyond belief. Moving down long, sloping corridors they would continually crash into walls, for a three-legged beast cannot go straight without very careful planning.

In many-dimensional parameter spaces simplexes have more than three legs. (They always have one more leg than there are dimensions in the parameter space.) But their behavior in these spaces follows the same pattern, and the cartoon of three-legged beasts lumbering across a two-dimensional surface, embedded in a three-dimensional space, is a reasonable aid to the intuition.

In MINUIT, the simplex algorithm is of the "highly evolved" type. It adapts to local conditions on the $\chi^2$ hypersurface by varying the errors assigned to current values of the parameters. These errors are used in the algorithm to control the sizes of steps the simplex takes in parameter space. SIMPLEX moves toward the bottom of a valley on the $\chi^2$ hypersurface much more efficiently than does the Monte Carlo algorithm SEEK. But, once within a valley, SIMPLEX is less capable than SEEK of abandoning it in favor of a different and possibly deeper one.

The variable-metric, gradient minimization, "MIGRAD", is the most intelligent of the three algorithms used in MINUIT, in the sense that it gathers and uses the most information about the local $\chi^2$ hypersurface, as it travels through the parameter space. MIGRAD is

also the least robust algorithm: when the parameter errors mentioned above are inappropriate for the local $\chi^2$ terrain, MIGRAD is easily confused by the information it gathers.

Unlike SEEK and SIMPLEX, which attempt to move downward with every guessed set of parameters, MIGRAD uses most of its calls to FCN simply to gather information, and only when its picture of the local $\chi^2$ hypersurface is reasonably complete does MIGRAD act on this information. MIGRAD systematically calls FCN with sets of parameter values intended to determine locally the first two derivatives of $\chi^2$ as a function of the parameters. From these derivatives, it calculates a parabolic approximation to the hypersurface in its vicinity and moves in the known direction of the minimum value of $\chi^2$ in this approximation. Thus, MIGRAD abstracts, from the information it receives, a simplified view from which decision making is relatively easy.

MINUIT is myopic. It has "knowledge" of the $\chi^2$ hypersurface at the current point and, at best, such knowledge of the immediate vicinity that the first two derivatives of $\chi^2$ with respect to the parameters can give. The parabolic approximation to the $\chi^2$ hypersurface used by MIGRAD is generally only valid in the immediate vicinity of its current location in parameter space. Finally, MINUIT has only a very rudimentary ability to back away from a local $\chi^2$ minimum and ignore it in further searching for lower minima.

Normally, it is neither necessary nor desirable that MINUIT

explore any large area of the $\chi^2$ hypersurface; all one wants is that MINUIT explore its deepest "valley" and locate the bottom. If started at any point in the deepest valley, MINUIT is expert at finding the bottom. However, MINUIT has no way of knowing whether a particular minimum of $\chi^2$ it has found is the lowest possible, and in a parameter space of more than 14 dimensions, there may be many local minima.

4.3.4.3 The FCN routine of PSF

The subroutine FCN, of PSF, performs several different functions depending on the setting of a passed integer flag. By far the vast majority of calls from MINUIT to FCN are simple requests for a $\chi^2$ evaluation. All other types of calls are initiated by the user and are used, for examples, to initialize FCN's local data, to target its $\chi^2$ calculation to specific data points, and to request plots of the data and fit.

The calculation of $\chi^2$ by PSF is configurable by the user for a variety of effects: PSF can calculate cross section and analyzing power at a single energy and many scattering angles, as a phase-shift analysis program would do in fitting angular-distribution data; it can also calculate excitation functions at many angles, and so facilitates the fitting of resonance parameters directly to data. PSF can attend to all or any connected portion of the energy range spanned by the data set it reads in. It can also attend to every $n^{th}$ energy in the data; this feature can be used to speed up the initial stages of a search.

## 4.4 Analysis of beam-resolution data

Beam-resolution data for this thesis were acquired using the "ramp-ramp" method and hardware described in sec 2.1.6; the general data-analysis strategy (see fig. 2.11) was also presented in that section. In this section the implementation of that strategy is described. Two simple determinations are required to transform the raw beam-resolution data into a resolution function: for each beam sample selected by the ramp-ramp system, the relative beam intensity and the relative centroid beam energy must be determined. The relative beam intensity is determined for each beam sample by summing a non-resonant peak in the ejectile-energy spectrum collected using that sample. Determination of the relative centroid beam energy is somewhat more involved.

Determination of the relative centroid energy of the beam samples taken in the measurement is done by comparing target-ramp excitation-function data acquired, from some resonant scattering process, with the various samples. The data are count rates $R_i$ as functions of target voltage V, where *i* indicates with which sample the data were acquired. In the simplest case, $R_i(V) = C_{i,j}\ R_j(V+\Delta_{i,j})$, where $C_{i,j}$ is the ratio $I_i/I_j$ of beam intensities of the two samples, and $\Delta_{i,j}$ is the difference in their centroid beam energies. Ignored here are any differences in the instrument functions (see sec. 2.1.6.2) associated with samples i and j.

Assuming this relationship among $R_i$, the relative centroid energy

of each beam sample can be assigned by picking any particular count-rate function $R_k$ and fitting all other functions $R_i$ to it by calculating the quantities $C_{i,k}$ from the beam-intensity data and varying the centroid-energy differences $\Delta_{i,k}$. This can be done visually with good precision by plotting the functions on a computer screen and translating one along the energy axis to superimpose it on the other--using, e.g., an interactive-graphics or CAD program. It would be difficult to write a computer program that could do a better job than the human eye in this simple pattern-matching task; given the unknown instrument function and other uncertainties in the measurement, the marginal improvement possible would yield little real benefit.

## 4.5 Analysis of high-resolution data

Analysis of the high-energy-resolution data for this thesis is superficially very similar to analysis of the low-resolution data. Both analyses begin with calculation of the target resolution function and estimation of the beam resolution function. The analyses relate observed data to essentially the same equation, which describes resonant plus nonresonant nuclear scattering. In both analyses the parameter variation involved in reconciling parameterized theory with observed data is supervised by the minimization program MINUIT.

In detail, however, the two analyses are quite different. The low-resolution data consist of many resonances which overlap to such an extent that inferring states in the compound nucleus from excursions in the scattering data is problematic; the high-resolution data consist of isolated resonances so narrow in energy that underlying nonresonant scattering may be taken approximately as energy independent. Also, the high-resolution data were acquired from only four scattering angles while the low-resolution data were acquired from eight. For this reason, it would be impractical to fit the high-resolution data from a single beam energy as an angular distribution, since the number of data points would be fewer than the number of fit parameters required.

### 4.5.1 The target resolution function

The target resolution function is the scattering probability as a function of scattering energy that describes a beam/target

combination. That scattering probability should vary with scattering energy is a consequence of three simple facts: projectiles lose energy as they travel through the target; projectiles scatter with a probability that may vary with distance travelled into the target; and target nuclei are not stationary and do not move with constant velocity.

In some previous analyses of high-energy-resolution scattering data, the energy-loss component of the target resolution function was identified with the energy-straggling distribution of an initially mono-energetic beam that had travelled completely through the target. This identification neglects the largest contribution to the energy-loss component--the variation in centroid energy of the beam as it travels through the target--and would only be correct if all projectiles waited until they had passed completely through the target before scattering from it.

Calculation of the resolution-function contribution from the ion-implanted targets used to acquire high-energy-resolution data is nearly identical to the calculation of the gas-cell resolution function described in sec 4.3.1. The following description will parallel that section closely and dwell mainly on the differences between the two calculations. There are two very obvious differences, one of which simplifies and the other of which complicates. In addition, there is the complication that Doppler broadening of the target resolution function is not generally negligible for high resolution targets, as it was for the gas-cell target.

There is no region of the ion-implanted target from which scattered beam cannot enter the detectors, and so there is no need to divide the target into regions whose resolution-function contributions must be calculated separately and then convoluted together. In the language of section 4.3.1, the ion-implanted target is entirely of "region 3"; apart from the Doppler-broadening contribution, its resolution function is calculable by a procedure very similar to that illustrated in figure 4.3 of that section, but for one detail.

For the purpose of calculating a resolution function, the difference between an ion-implanted target and "region 3" of the gas cell is the presence in the implanted target of a nonuniformly distributed contaminant: the substrate into which target nuclei were implanted. This difference is addressed in the implanted-target resolution-function calculation by two simple modifications of the gas-cell calculation: generalization of the depth scale by which progress of the beam through the target is described, and renormalization of the representative beam-energy distributions before they are summed.

The measure of depth used in calculation and expression of the target implant-depth distribution is $\mu g/cm^2$ of substrate material, rather than a length measure such as $\mu m$. Since the substrate is by definition uniformly distributed with respect to this measure, use of it simplifies the resolution function calculation: there is only one nonuniformly distributed target component, with this measure of depth, rather than two.

The implanted-target resolution-function calculation begins, as did the gas-cell calculation, by dividing the target into equal "slices" normal to the beam direction (see fig. 4.5). One does *not* assume that the scattering probabilities are the same for all slices (as was assumed in the gas-cell calculation, and as one normally would assume for an evaporated or sputtered target). Rather, the probability for scattering within a given slice is proportional to the number of implanted atoms in that slice. A representative energy-loss distribution is calculated for each slice assuming an initially monoenergetic beam which has travelled from the upstream end of the target to the midpoint of that slice, and one assumes that all scattering from a given slice is scattering of incident particles drawn from the representative distribution.

Given a representative energy-loss distribution for each slice of the target, the resolution function is assembled by multiplying each distribution by the fraction of the total implant contained in the slice that distribution represents, summing the renormalized distributions, and normalizing the sum. The computer program TS, which performs the calculations described above, has been written for the Amiga computer. Results of the actual calculation are shown in the inset of figure 4.5.

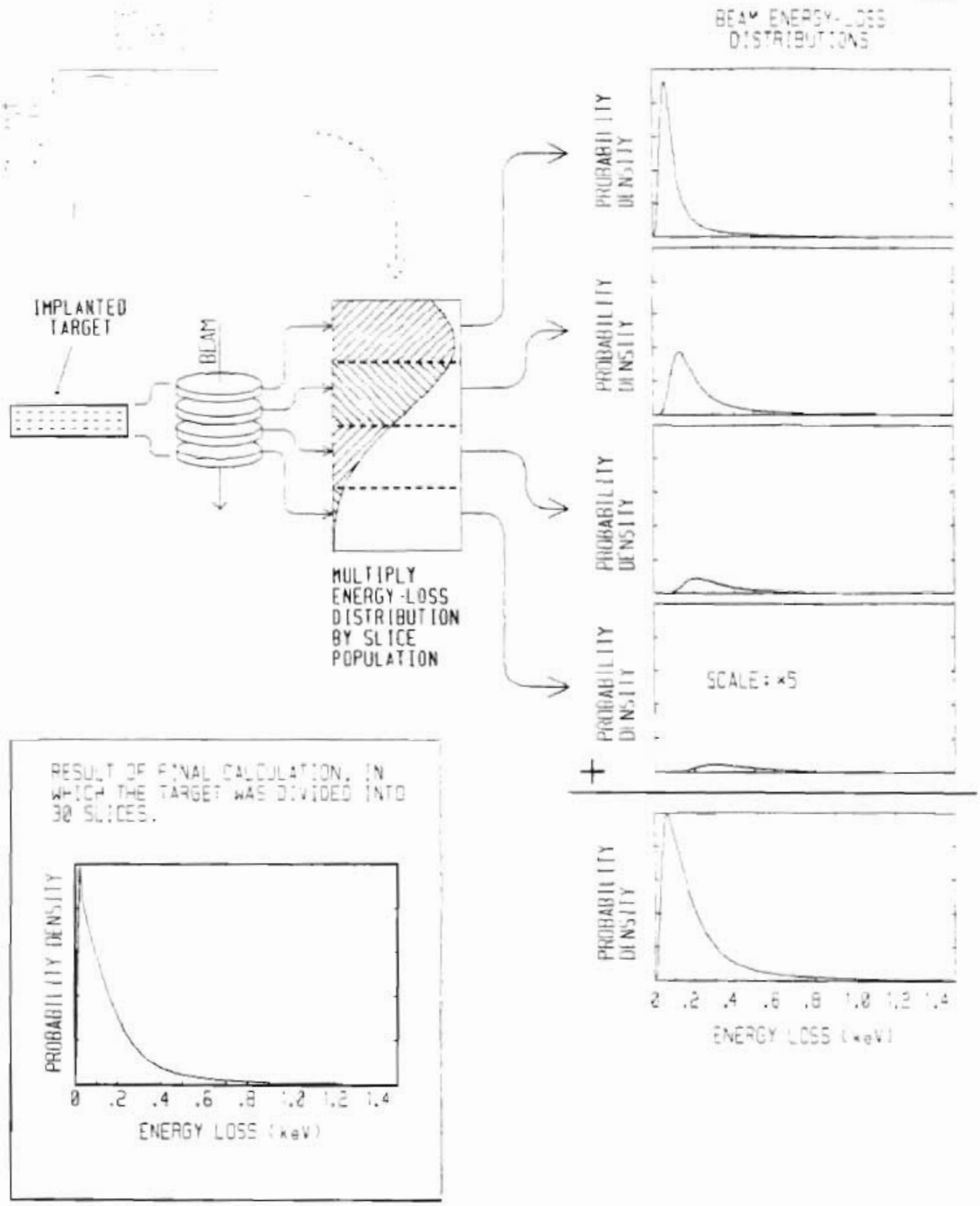


Figure 4.5 Calculation of the energy-loss contribution to the target resolution function.

### 4.5.2 Theory

Analysis of high-resolution scattering data is similar in many respects to the analysis of low-resolution data described in sec. 4.3. As before, equations 4.3a and 4.3b (reproduced below) express the non-spin-flip and spin-flip scattering amplitudes from which the differential cross section and analyzing power are calculable. But, for analysis of the very narrow T = 3/2 resonances in high-resolution data, it is useful to group terms in the scattering amplitude equations according to their energy dependence, rather than according to their angular-momentum dependence.

$$a = f_c + \frac{1}{k} \sum_L \sum_J [(J+1/2)\ \alpha^L_{J-L}\ e^{2i\omega_L}\ P_L(\cos\theta)] \qquad (4.3a)$$

$$b = \frac{1}{k} \sum_L \sum_J [(-1)^{J-L-1/2}\ \alpha^L_{J-L}\ e^{2i\omega_L}\ P^1_L(\cos\theta)] \qquad (4.3b)$$

Such a regrouping yields the following equations for the helicity amplitudes:

$$a = a_{nr} + a_R \qquad (4.7a)$$

$$b = b_{nr} + b_R \qquad (4.7b)$$

where $a_{nr}$ includes the Coulomb-scattering amplitude and a sum over all L and J of the non-spin-flip nuclear amplitudes not attributable to compound-nucleus formation of the T = 3/2 state of interest; where, similarly, $b_{nr}$ includes the spin-flip amplitudes; and where $a_R$ and $b_R$ are the amplitudes for resonant scattering through the T = 3/2 compound-nucleus state. Although the terms $a_{nr}$ and $b_{nr}$ describe resonant scattering through T = 1/2 compound-nucleus states (as well as Coulomb and nuclear-potential scattering), for purposes here they are

regarded as nonresonant since they vary so much more slowly with energy than do $a_R$ and $b_R$.

The angular dependence of $a_{nr}$ and $b_{nr}$ is complicated and unknown since it results in part from a sum of Legendre polynomials with unknown weights, the L-wave, nonresonant scattering amplitudes. Since we are interested solely in isospin-forbidden resonant scattering, we have little to gain from untangling this angular dependence and, in any case, have data from too few angles even to attempt it. Instead, we can view the $a_{nr}$ and $b_{nr}$ for scattering at different angles as unrelated, and vary them independently to fit the data.

The resonant amplitudes $a_R$ and $b_R$, on the other hand, have an angular dependence that follows directly from the spin and parity of the compound-nucleus state the scattering from which they describe. Moreover, this angular dependence is isolated in a Legendre polynomial; the remaining factors of $a_R$ and $b_R$ are angle-independent, single-level resonance amplitudes and can be fit simultaneously to data from all scattering angles.

### 4.5.3 The program RESFIT

RESFIT is similar to the program PSF described earlier. It is organized around the needs of the MINUIT minimization package (see sec. 4.3.4.2) in exactly the same way as is PSF, and it uses resonance and background parameters similarly. But its background parameters are the helicity amplitudes of eqn. 4.7, rather than phase-shift

parameters, and its calculation of $\chi^2$ from parameters is streamlined to eliminate redundant calculations that involve convolution of resonance and resolution-function distributions.

In the analysis of narrow-resonance data, RESMIN replaces the program T32GRD that was used by Wilkerson [Wil82] and Ikossi [Iko75]. Compared with T32GRD, RESMIN has both advantages and disadvantages.

The principal advantage enjoyed by RESMIN is that its parameter search is directed by the MINUIT package, while T32GRD uses a grid search. Thus, RESMIN can minimize $\chi^2$ with essentially no help from the user. Two other advantages are that RESMIN can fit simultaneously data from many scattering angles and that its calculation of $\chi^2$ is more efficient than that of T32GRD. These advantages, together, facilitate investigation of the sensitivity of the data to the parameters: for example, with RESMIN, a parameter can be fixed at a trial value while all other parameters are varied automatically to minimize $\chi^2$. Such an investigation was essentially impossible with T32GRD because that program fits data from a single scattering angle at a time, and would have been impractical even without this limitation because the grid search T32GRD performs demands so much attention from the user that the large number of minimizations required could not be done in a reasonable time.

The principal disadvantage of RESMIN, compared to T32GRD, is that complicated constraints on the parameters are greatly more difficult to apply. This follows directly from the amount of fine control over the parameter variation that must be given up by the user so that MINUIT can operate. In T32GRD, it is relatively easy to apply constraints not only to parameters individually, but also to functions of a number of parameters: to slightly overstate, one simply declines to calculate $\chi^2$ with a set of parameters that violates such constraints. In RESMIN, however, all parameter constraints must be "cleared" in advance with MINUIT, and MINUIT does not support multi-parameter constraints. Instead, the user must find linear combinations of parameters for which all needed constraints involve only a single parameter. (For example, in RESMIN, the real and imaginary parts of background, helicity amplitudes are replaced by the magnitude and phase of the complex amplitude for precisely this reason. But this simple parameter transformation does not allow the imposition of any constraint involving both spin-flip and non-spin-flip amplitudes, and one would like to apply such a constraint.)

# 5. Presentation of results and conclusions

## 5.1 The resolution function

Measurements of the beam-resolution function were performed immediately preceding the acquisition of resonance data for the lowest two T = 3/2 states--at beam energies of 6.872 and 7.125 MeV. The resolution-function data were analyzed using the procedure discussed in section 4.5.

At the lower beam energy, two separate analyses were performed using the data acquired from scattering at 145 and 165 degrees; at the higher energy, only one analysis was performed. All three resolution functions are plotted in figure 5.1, along with a spline fit to the 165-degree data at 6.872 MeV. The spline fit was performed so that points regularly spaced in energy could be extracted for use in the fitting program RESMIN.

The three results resemble one another closely, as can be seen from figure 5.1. Error bars are not included in the figure for the sake of clarity; for all points, there is an energy imprecision of approximately 300 eV or greater, and vertical-scale errors are relatively negligible. The three functions are essentially the same, within errors; this is the expected result for the analyses of 6.872 MeV data.

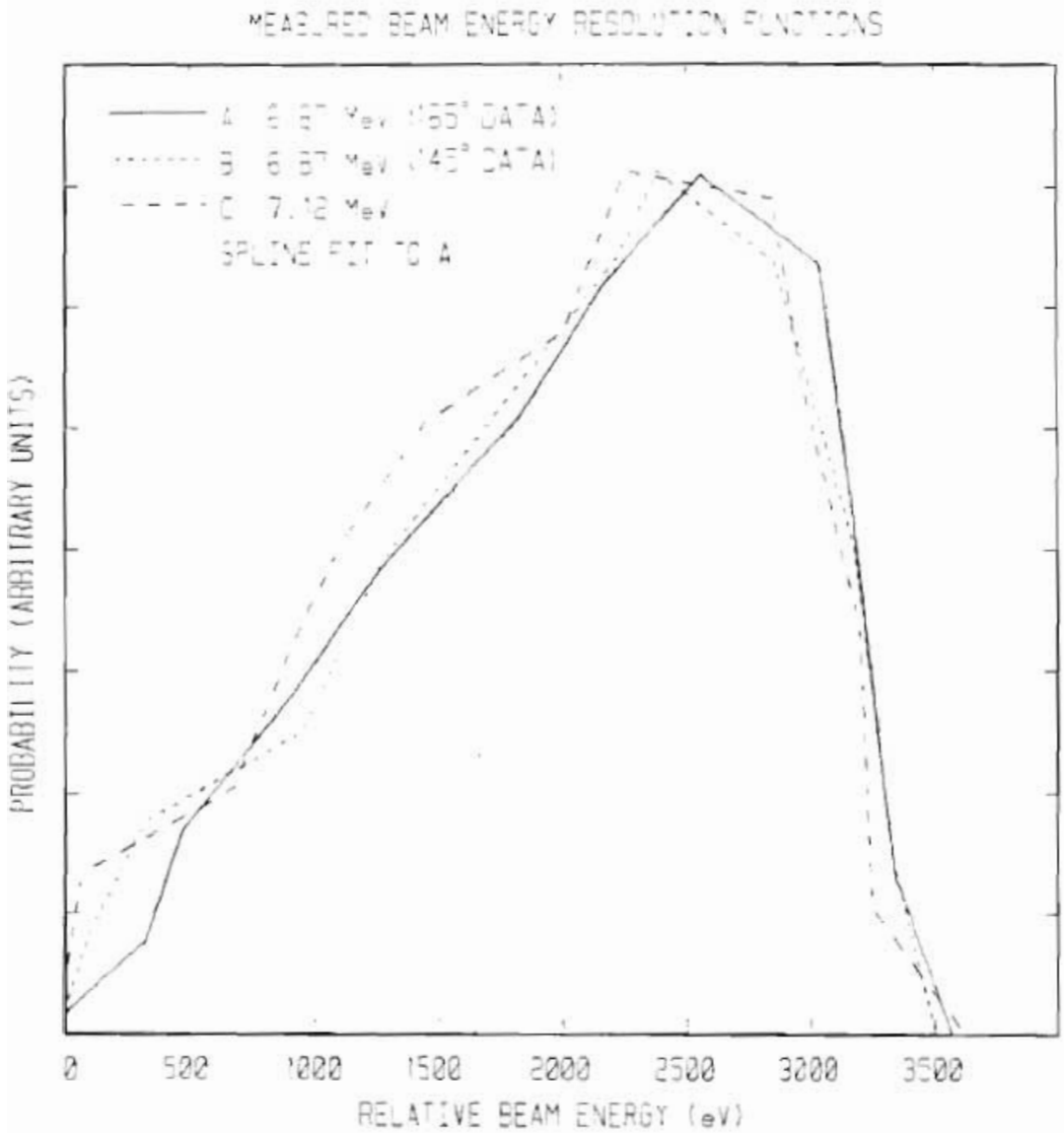


Figure 5.1 Beam resolution functions measured at 6.87 (a, b) and 7.12 MeV (c), along with a spline fit to measurement a.

The result is not unexpected of the analysis of 7.125 MeV data since the two measurements were performed under nearly the same conditions, but for the 253 keV (roughly 3 percent) difference in energy.

The spline-fit resolution function used as input to the resonance-fitting program RESMIN shows a FWHM of approximately 2100 eV. This width is significantly greater than the observed width (approximately 1700 eV) of the $E_p$ = 6.872 MeV resonance indicating that, in this case, the beam resolution at the center 90-90 slits was not the same as the beam resolution at the target. (See discussion in section 2.1.6.4.) This is unfortunate since it limits the usefulness of the measurement in analysis of the resonance data.

The measured beam resolution function clearly cannot be used without modification in resonance fitting. However, it remains the best information available about the shape, at least, of the true beam resolution function. This shape information was salvaged from the measurement result for use in RESMIN in the following way: the resolution function was used in RESMIN with a scaling parameter, AWID, that specified the relative energy separation of the spline-fit distribution points. By varying AWID, RESMIN could vary the width of the resolution function without directly affecting its shape.

However, varying AWID does vary the shape of the *total* resolution function used in RESMIN, since this total is the convolution of the measured, scaled beam resolution function with a Gaussian function

originally intended to represent all contributions other than beam and target resolution functions. With AWID, RESMIN has been given license to construct implicitly a beam resolution function that is a convolution of the measured, scaled distribution with any "piece" of the Gaussian function. (This by virtue of the fact that the convolution of two Gaussians is again a Gaussian.)

The target energy-loss contribution to the total resolution function was discussed in section 4.5.1. This distribution is so narrow (approximately 200 eV in width) compared to other distributions that contribute to the observed resonance width that, if included in the RESMIN calculation, its effect on the generated resonance curves would be negligible. However, inclusion of the distribution would have the effect of slowing the calculation down considerably, since it would require an additional convolution, and convolution is by far the most time consuming part of the calculation. For these reasons, the target energy-loss resolution function was ignored.

## 5.2 Absolute energy calibration

The energy calibration, with which absolute excitation energies are assigned to resonances observed in this work, derives from a set of resonance measurements performed by J. F. Wilkerson [Wil82]. The results of those measurements were encoded by Wilkerson into a computer program that calculates beam energy given the NMR frequency corresponding to the magnetic field in a representative region within the upstream 90-90 magnet. The calibration is believed to be

accurate to ± 2 keV if the magnet system has been recycled (see [Wil82]) and if the locations of the 90-90 system's input and center slits are as they were during the calibration measurements.

Recently, however, the center 90-90 slits were moved slightly in an aborted attempt to realign the 90-90 system. The three resonances studied for this thesis were all observed before the slit move occurred; two of them, those corresponding to the first and second T = 3/2 states, were observed again after the slit move. The pre-slit-move data are of poorer quality than the post-slit-move data: their statistical precision is lower, and, since they were acquired with less sophisticated data-acquisition software than the more recent data, the subtraction of spectrum background from them was less accurately done. But the energy calibration of the pre-slit-move data is much more nearly correct than that of the post-slit-move data.

For the first T = 3/2 state, then, two analyses of scattering data were performed. Both pre-slit-move and post-slit-move data were first analyzed (per discussion in section 4.5) to determine resonance energies. A difference in energy of 14 keV was found between the two data sets. The margin of error in this relative determination is estimated, from the behavior of $\chi^2$ in parameter searches, to be ± 200 eV --much smaller than the accuracy (± 2 keV) of the 90-90 system energy calibration. The post-slit-move data were then translated upward in energy by the 14 keV difference in resonance energies, and analyzed again, as described below, to determine the other parameters.

## 5.3 The 8.974 MeV T = 3/2 state

The 8.974 MeV ($E_{Ex}$) resonance data contained the narrowest observed effect of all of the $^{21}$Na resonances measured in this thesis project. Also, for this resonance only, we have the results of an earlier measurement [Gou73] of the branching ratio, $\Gamma_p/\Gamma$. For these reasons, this resonance was used to determine the value of AWID (from section 5.1) to be used in analysis of both of the lowest two T = 3/2 resonances.

The sensitivity of the resonance data to AWID is shown in figure 5.2. To produce the results shown in the figure, RESMIN was first allowed to vary all resonance, background-amplitude, and resolution-function parameters within their constraints to find the best fit to the data. Then, AWID was fixed at the twelve different values shown in the figure. For each value of AWID, a complete minimization involving all other fit parameters was performed and the resulting parameter sets were recorded along with the best-fit values of $\chi^2$.

For AWID much less than 0.4 (yielding a measured, scaled beam resolution function of approximately 850 eV in width), the data showed little sensitivity: AWID could be traded off against the width of the Gaussian resolution function with little effect on the value of $\chi^2$. This is understandable since the total observed width is some 1700 eV; for AWID much less than 0.4, the total resolution function becomes dominated by the Gaussian resolution function, which (the data indicate) must largely make up the difference. The best fit value of

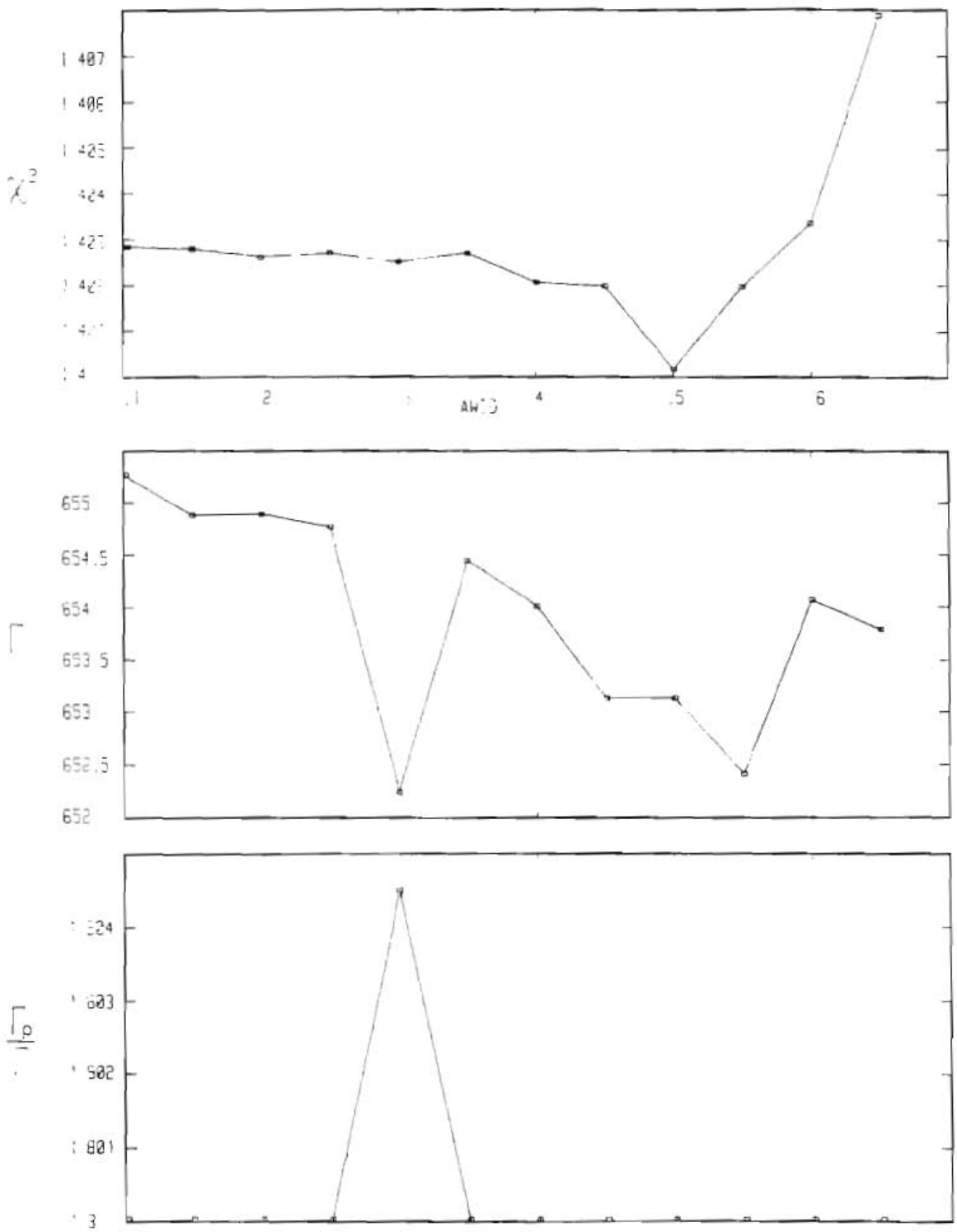


Figure 5.2 Determination of the parameter AWID from the lowest-energy, T = 3/2 state data.

AWID is very near 0.5; in the following analyses, AWID was fixed at this value.

Given AWID and the corresponding best-fit values of the resonance parameters $E_R$, $\Gamma$, and $\Gamma_p$, the sensitivity of the data to variation of those resonance parameters was investigated. This procedure was intended to yield error bars for the parameters $\Gamma$ and $\Gamma_p$.

Note that this method of assigning errors differs significantly from that employed in previous analyses ([Wil82] and [Iko75]). The computer program used in those analyses, T32GRD, could not fit simultaneously data from more than one scattering angle. Therefore, errors assigned were the standard deviations of the sets of resonance-parameter values found in separate fits to data from different scattering angles.

With AWID fixed at 0.5, the resonance width $\Gamma$ was varied in 50-eV steps about the best-fit value of 650 eV. For each value of $\Gamma$, a complete minimization, in which all other parameters were allowed to vary, was performed. The responses of $\chi^2$ and the fit parameter $\Gamma_p/\Gamma$ to this procedure are shown in fig. 5.3, along with the resulting values of the resonance partial width $\Gamma_p$. Although a minimum of $\chi^2$ is shown in figure 5.3, careful attention should be given to the vertical scale: $\chi^2$ varies by only one or two percent throughout the range of $\Gamma$ investigated. There is a marked anti-correlation between $\Gamma$ and the branching ratio (or, equivalently, a correlation between $\Gamma$ and the

value of $\Gamma_p$ derived from the branching ratio).

For these reasons, we cannot assign an error bar with the usual interpretation--i.e., that of a range within which the true value is expected, with probability .63, to lie. Nevertheless, the best-fit values of $\Gamma_p$, found with the branching ratio constrained to the range [.18 ... .22], were within $\pm$ 10 eV of 117 eV. Dividing this result by twice the Coulomb penetrability yields the value 125 eV for the reduced partial width $\gamma_p^2$.

In the searches described above, the resonance energy, $E_R$, varied by less than 100 eV about its best-fit value of 6.872 MeV. Since this variation is much smaller than the beam-energy reproducibility at TUNL, approximately 2 keV, it contributes negligibly to the error bar on $E_R$. Our assignment for the excitation energy of the lowest-energy T = 3/2 state, then, is 8.974 $\pm$ .002 MeV, in excellent agreement with previous measurement [McD69].

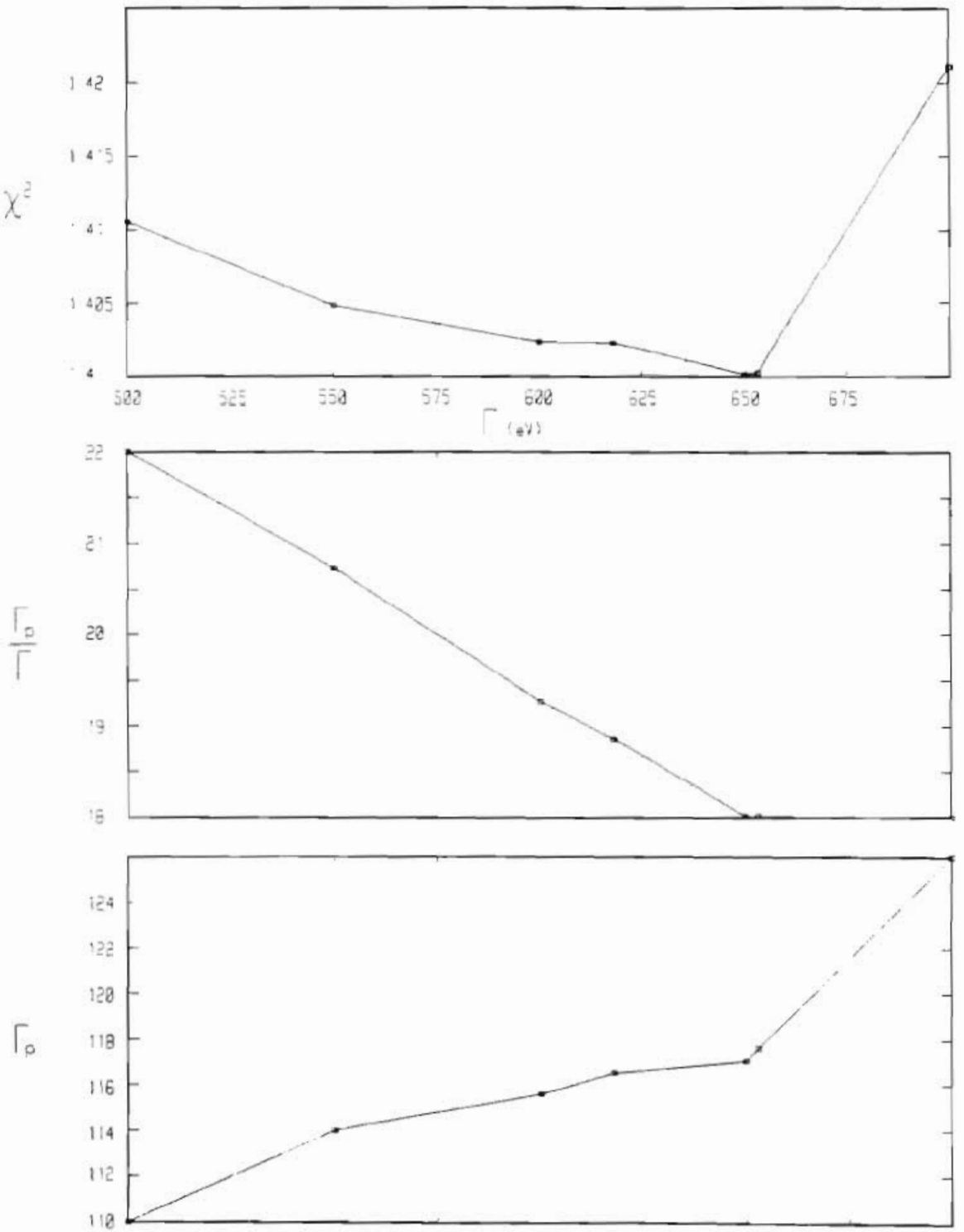


Figure 5.3 The sensitivity of the lowest-energy, T = 3/2 state data to variation of Γ about its best-fit value.

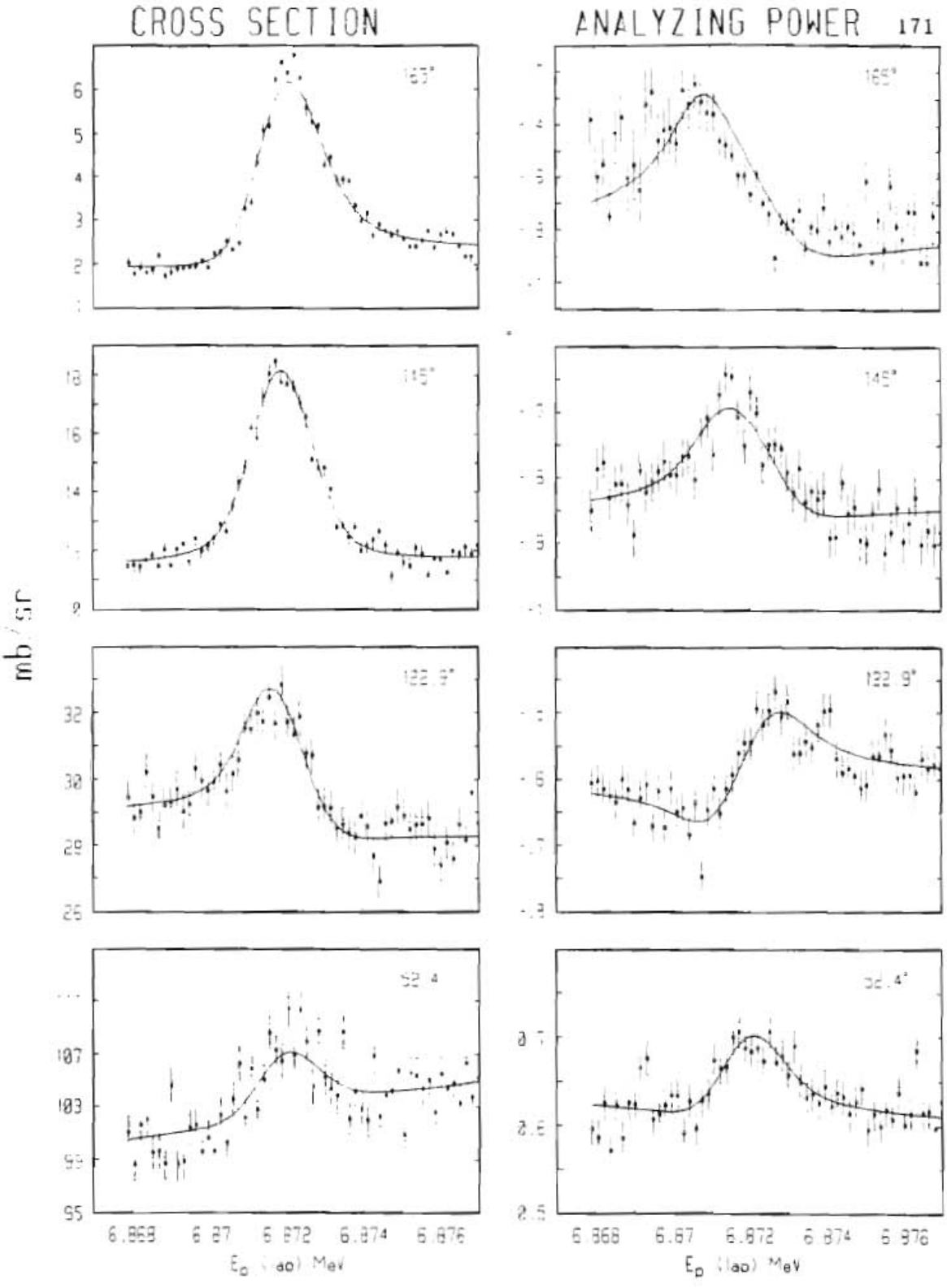


Figure 5.4 RESMIN fits to the lowest-energy T = 3/2 state in $^{21}$Na.

## 5.4 The 9.215 MeV T = 3/2 state

The analysis of data from the second T = 3/2 resonance was qualitatively very similar to the analysis described above. Investigation of the data's sensitivity to the value of the parameter AWID was not performed, however. In view of the similarity in measured beam resolution functions acquired for the two resonance analyses, the value of AWID determined in earlier analysis was taken as valid for this analysis as well.

The remaining analysis was performed in exactly the same way as that described above with qualitatively very similar results (see figure 5.5): a modest minimum of $\chi^2$ was found at the value of 2800 eV for the resonance width $\Gamma$. In response to variation of $\Gamma$ about this value, over the energy range [2500 ... 3300] eV, $\chi^2$ varied by approximately 2 percent. The value of 1450 eV was found for the partial width $\Gamma_p$, which varied in correlation with $\Gamma$ over the energy range [1300 ... 1600] eV. Dividing this best-fit result by twice the Coulomb penetrability yields the value 477 for the reduced partial width $\gamma_p^2$. Fits calculated from the best-fit parameter set are shown in figure 5.6.

The resonance energy, $E_R$, varied by less than 100 eV, about its best-fit value of 7.125 MeV, in response to the forced variation of the resonance full width $\Gamma$. Our assignment of the excitation energy is 9.215 $\pm$ .002 MeV, in good agreement with previous measurement [McD69].

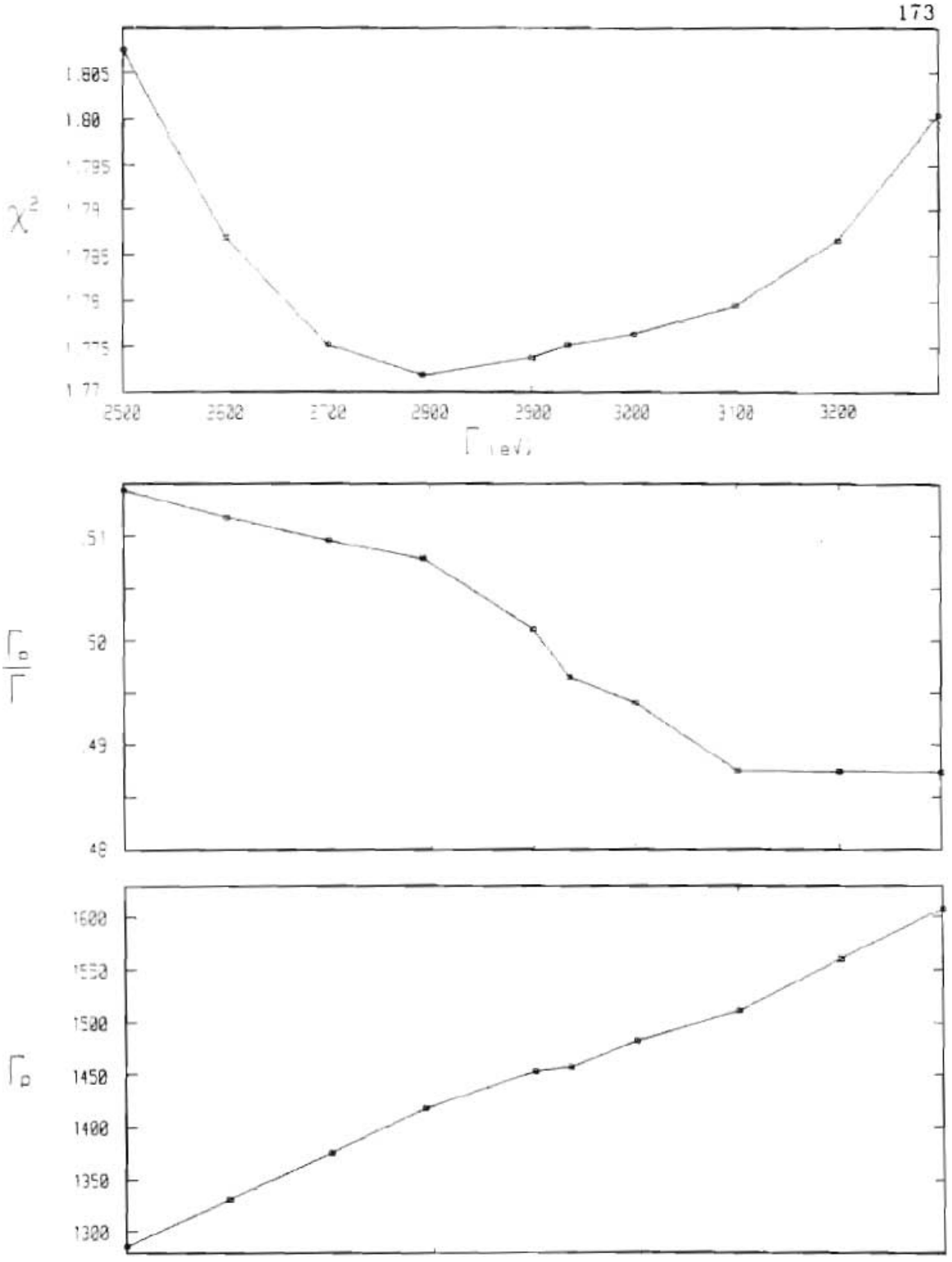


Figure 5.5 The sensitivity of the $2^{+}d$ T = 3/2 state data to variation of $\Gamma$ about its best-fit value.

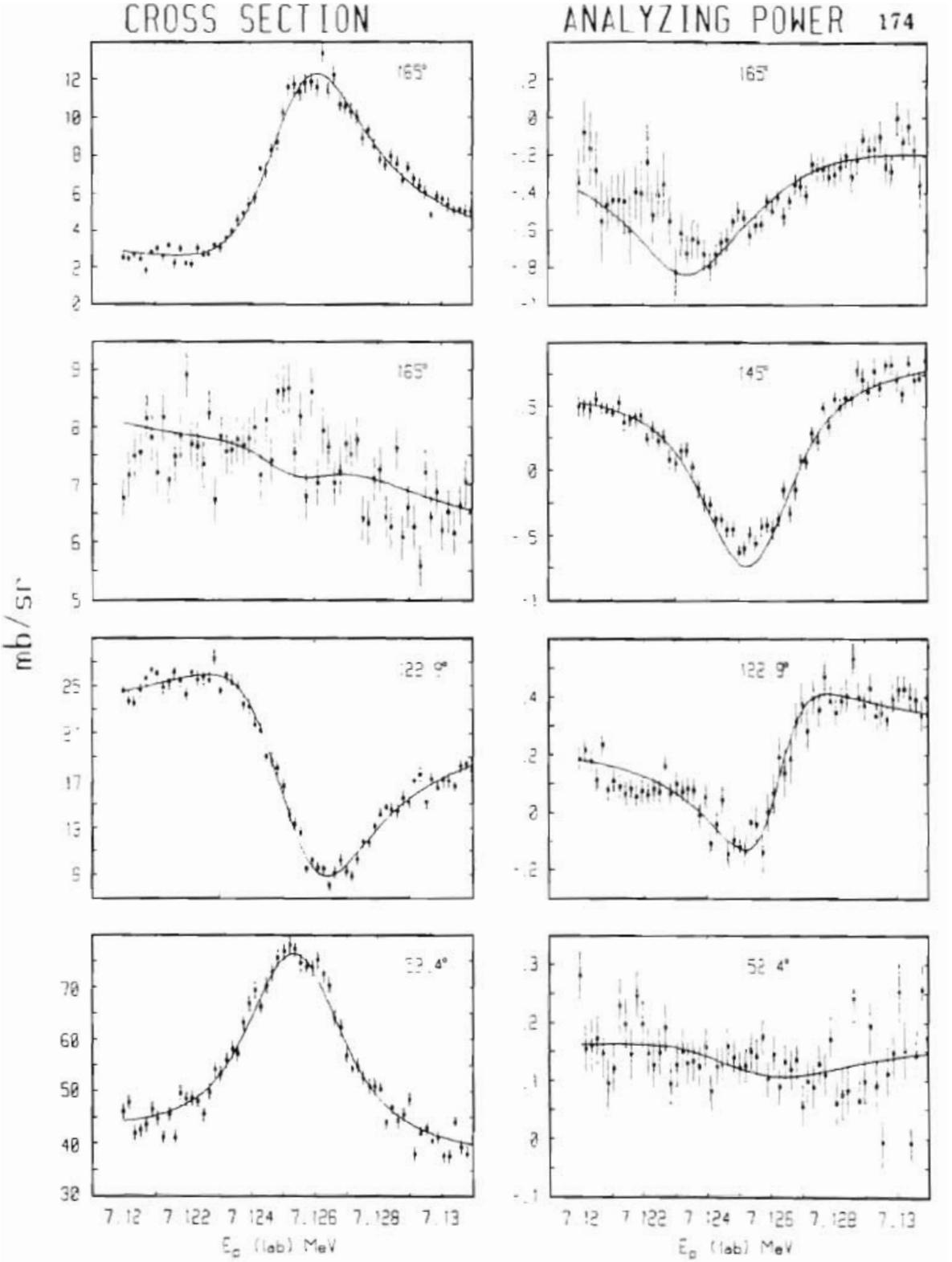


Figure 5.6 RESMIN fits to the $2s_{\frac{1}{2}}$ T = 3/2 state in $^{21}$Na.

## 5.5 The 10.082 MeV T = 3/2 candidate

The resonance we tentatively identify with the third T = 3/2 state in $^{21}$Na has not been seen before in a high-resolution excitation function. Also, we did not see a state with this energy in the $^{23}$Na(p,t)$^{21}$Na reaction data acquired at the Princeton AVF Cyclotron. Therefore, initial fits were performed to determine the spin and parity of the compound-nucleus state responsible for this resonance, and thus to help identify it. The best fits generated by both PSF and RESMIN were obtained with the spin and parity values $1/2^-$. Other values produced poorer--in most cases much poorer--results. Previously [Mai81], the third T = 3/2 level in the mass-21 system was deduced to be of spin and parity $1/2^-$.

This resonance occurs at approximately 30 keV higher in excitation energy than one would expect, given the known location of the first T = 3/2 state and the IMME-derived [Hin81] energy separation between the first and third T = 3/2 states (see table 3.2 in sec. 3.2.3). No resonances closer to the expected energy were seen in our high-resolution excitation functions.

This resonance is much broader than either of the two lower-energy resonances. Analysis of the data for this state are simplified somewhat by this fact, since it means that the resonance width is much larger than any plausible width of our total resolution function. The data, then, can't be expected to have any useful sensitivity to the resolution-function width.

Accordingly, both resolution function parameters, AWID and the Gaussian FWHM, were fixed at the best-fit values found in the previous analysis, and the sensitivity of the data to variation of the resonance width $\Gamma$ was performed as before. The result is a very smooth dependence of $\chi^2$ on the value of $\Gamma$ (see figure 5.7), which was varied over the range [4800 ... 6200] eV, with a modest but definite minimum at the point $\Gamma$ = 5475 eV. The resonance partial width $\Gamma_p$ was found to be linearly correlated with the full width $\Gamma$. In a $\Gamma$-driven variation over the energy range [1150 ... 1450] eV, the best-fit value of 1300 eV was found for $\Gamma_p$. Dividing this by twice the Coulomb penetrability yields the value 504 for the reduced partial width $\gamma_p^2$.

Once again, variation of the resonance-energy parameter $E_R$ about its best-fit value was small in comparison to our beam-energy reproducibility. That best-fit value was 8.036 MeV, and our assignment of excitation energy to this state is 10.082 $\pm$ .002. Fits calculated from the best-fit parameter set are shown in figure 5.8.

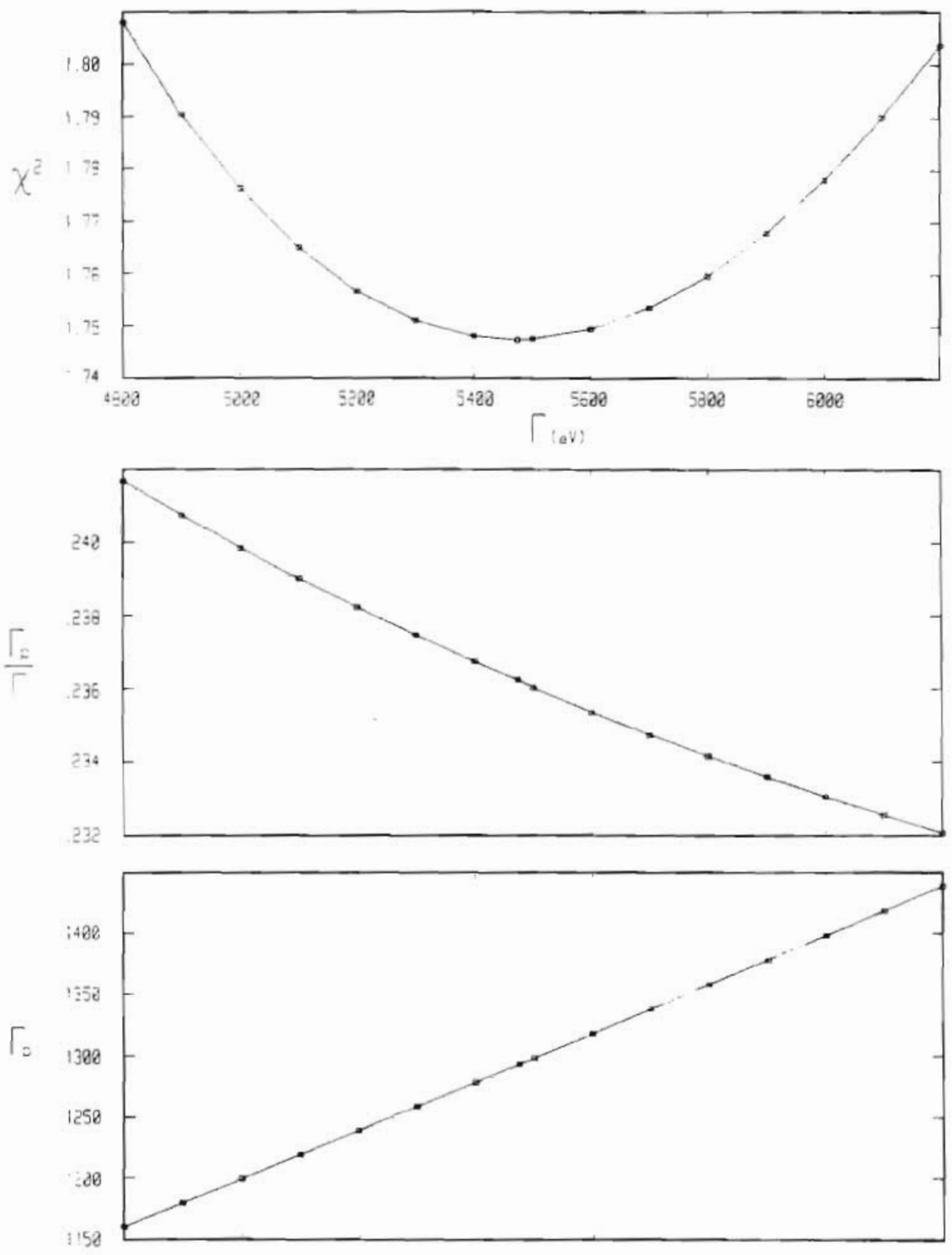


Figure 5.7 The sensitivity of data from the (candidate for the) 3rd T = 3/2 state to variation of Γ about its best-fit value.

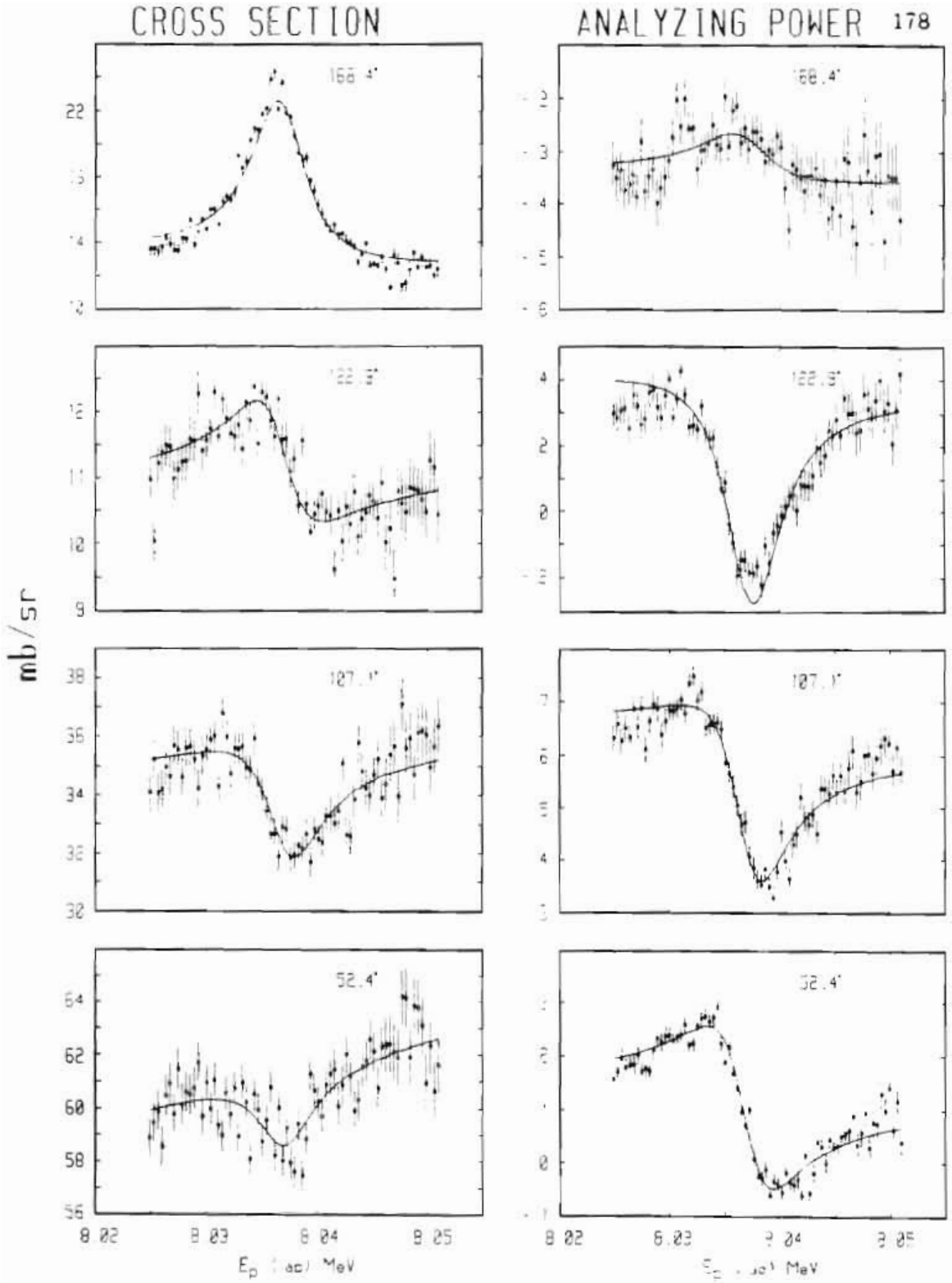


Figure 5.8 RESMIN fits to the (candidate for the) 3rd T = 3/2 state in $^{21}$Na.

## 5.6 The search for higher-lying T = 3/2 states in $^{21}$Na.

With the excitation energies determined from analysis of the $^{23}$Na(p,t)$^{21}$Na data (see table 3.2 in section 3.2.3.3), we searched with unpolarized beam in two high-resolution scattering experiments for the fourth through the seventh T = 3/2 states in $^{21}$Na. Some of the data from these runs are shown in figures 5.9 and 5.10.

Although the step excitations of figures 5.9 and 5.10 show some anomalies at excitation energies consistent with those assigned in table 3.2, few of the anomalies narrow enough to be considered likely T = 3/2 state candidates are outside of statistics, none are both outside of statistics and present in data from more than one scattering angle, and none were seen in closer examination with the target-ramp system. In view of the susceptibility of step-excitation data to time dependent normalization errors, ramp-excitation scans are believed more reliable indicators of local cross-section fluctuations.

Since these states weren't seen in high-resolution excitation functions, excitation-energy assignments for them derive from the $^{23}$Na(p,t)$^{21}$Na measurements made at the Princeton AVF Cyclotron.

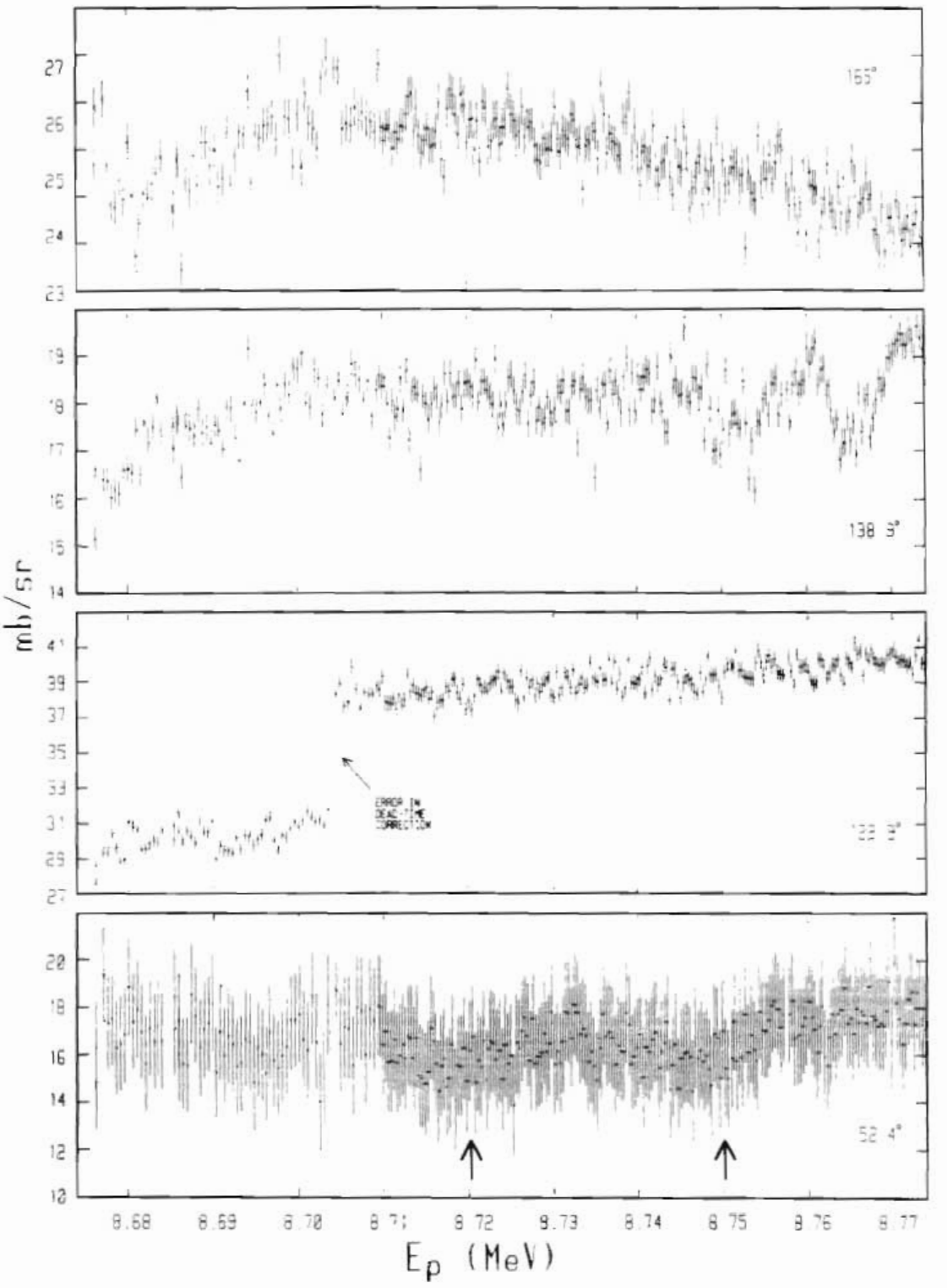


Figure 5.9 Cross-section excitation functions of $^{20}Ne(p,p)^{20}Ne$ acquired in the search for high-lying T = 3/2 states.

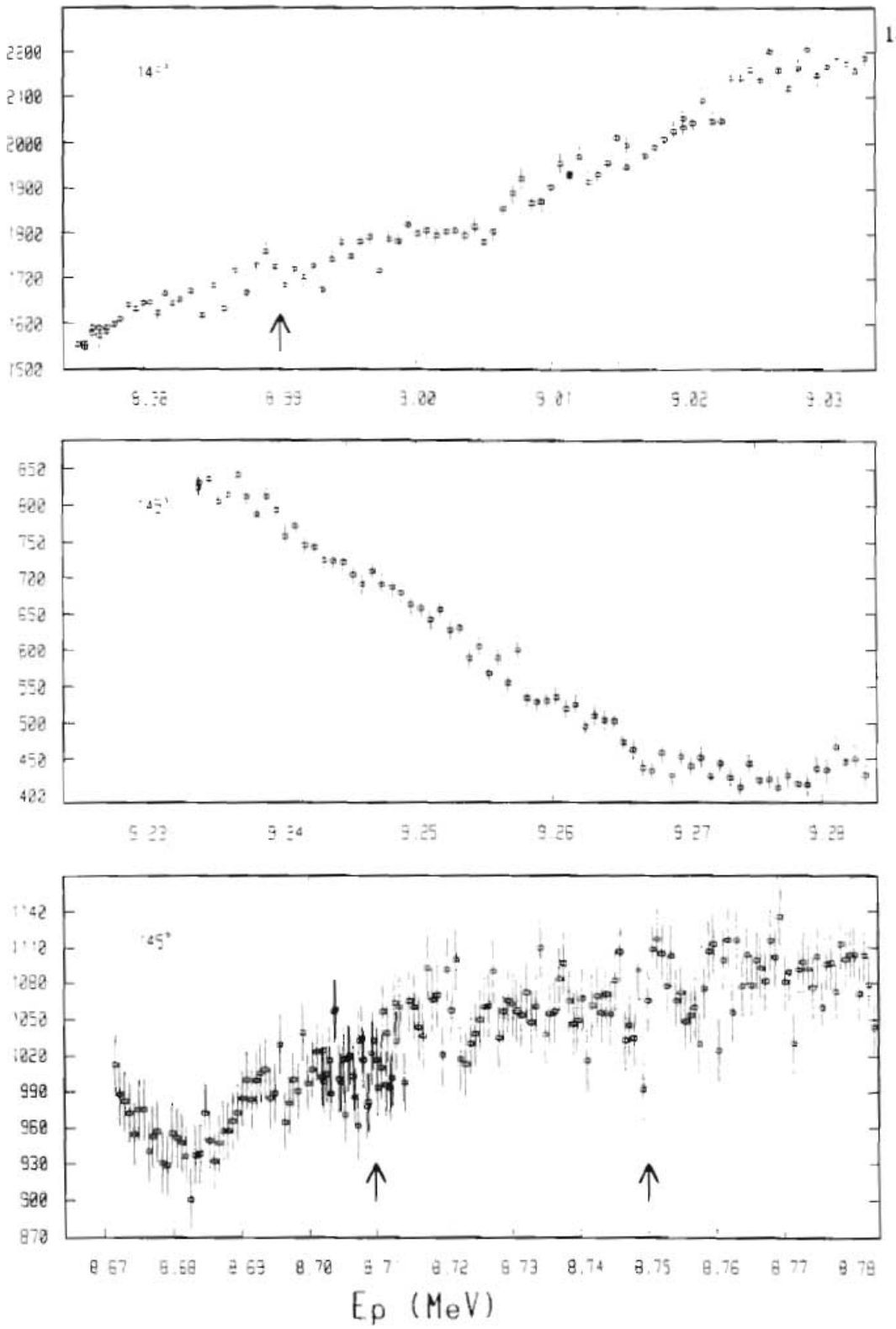


Figure 5.10 Raw scattering yields from $^{20}Ne(p,p)^{20}Ne$ acquired in the search for high-lying T = 3/2 states.

## 5.7 T = 1/2 states in the vicinity of the 8.974 MeV T = 3/2 state

A great deal of effort and time were spent attempting to discover the spins, parities, and energy locations of resonances that contribute to the excitation-function data shown in figure 5.11. These data were acquired in the hope that parameterizations of the contributing T = 1/2 resonances would facilitate calculation of isospin mixing between these states and nearby T = 3/2 states. The program PSF, described in sec. 4.3.4, was written and used in the hope that fitting resonance parameters directly to the data would yield a more complete and more definitive set of states than was previously found [Fer81] using a phase-shift analysis.

Several techniques, ranging from single-point, phase-shift analyses to all-out, multi-resonance fits were employed using PSF. The results were at once tantalizing and frustrating. When analyzing angular-distribution data from a single energy, or from a small number of energies simultaneously, PSF consistently yielded excellent fits to the data, but the data could not be shown to prefer one set of non-resonant phase shifts to all others.

In the first analyses, angular distributions of cross section and analyzing power at a single beam energy were fit to sets of phase shift parameters, using PSF. When an acceptable fit was found, the parameter set was recorded and fitting to data from the next beam energy was begun, starting with the recorded parameter set. In this way, we swept up and down in beam energy over a range, typically, of

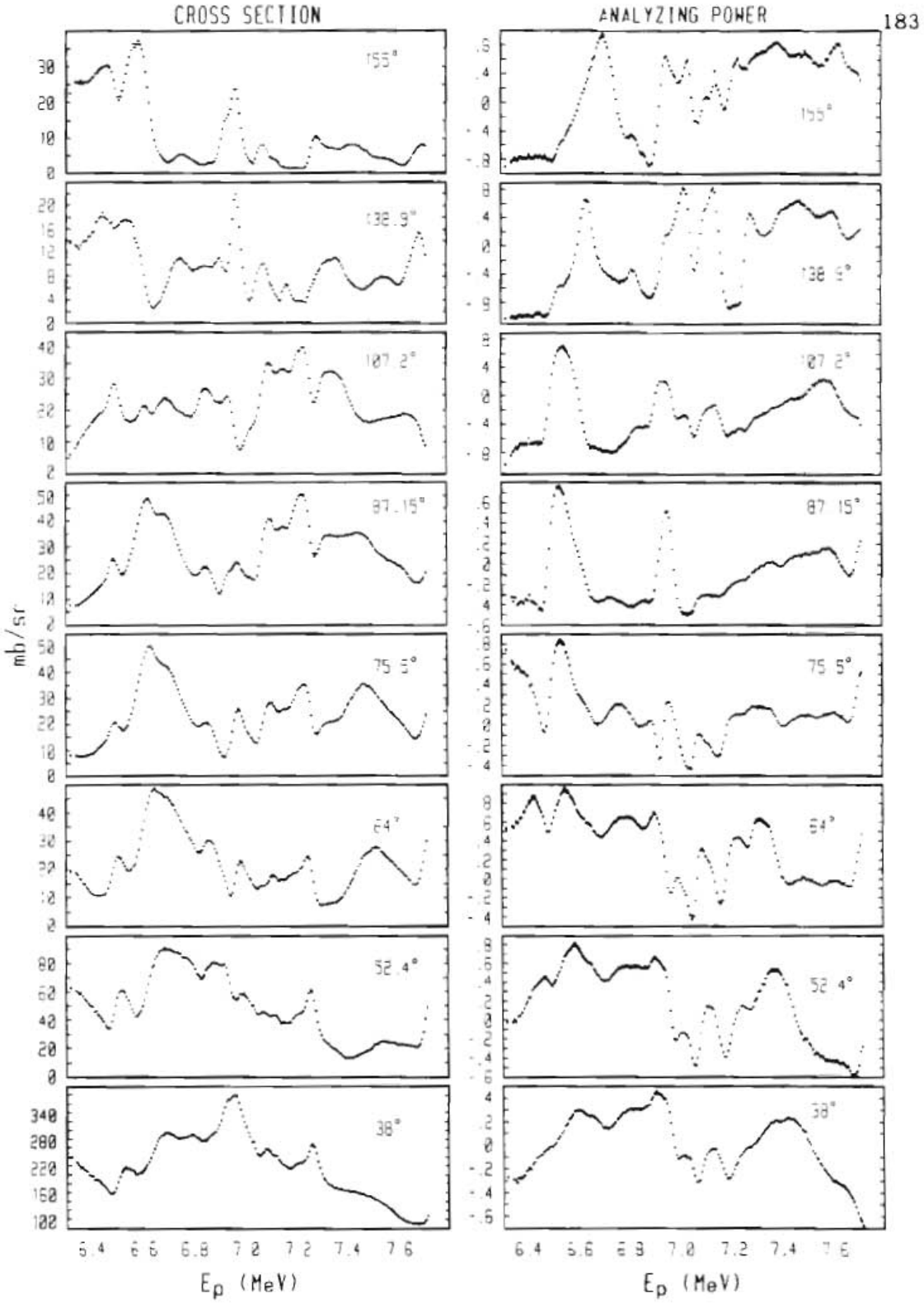


Figure 5.11 Low-resolution excitation functions of $^{20}Ne(p,p)^{20}Ne$.

100 keV, remaining always near an acceptable fit--near, at least, to the extent that data from adjacent energies were similar.

After sweeping up and down several times, the recorded parameter sets were reviewed for evidence of resonant behavior in the phase shifts. This process was repeated many times beginning at different energies within the studied region and beginning with different parameter sets. Some initial parameter sets were taken from optical-model calculations, some from what phase shifts we could extract from the earlier phase-shift analysis [Fer81] of similar data, and some were arrived at by randomization. In most cases, fits to the data were excellent, with values of chi-square per data point less than four. Many of the fits were visually indistinguishable from the data.

Reviewing the recorded phase-shift parameter sets, we found two disturbing, but not wholly unexpected, features: *collusion* among several phase shifts to produce excursions in the data, and poor "*tracking*", or reproducibility, of phase shifts from one sweep to another.

Collusion among phase shifts is expected. We may believe that excursions in the data are evidence of resonances and that phase shifts corresponding to a single scattering channel (L, J) should step up and take responsibility for those excursions, but we cannot express this expectation usefully without prescribing energy dependences to the phase shifts. The whole point in phase-shift analysis, as opposed to

resonance-fitting analysis, is to avoid prescribing energy dependences and, thereby, to minimize the number of parameters required to fit the data. Thus, while collusion is to be minimized, if possible, it should be regarded as a price to be paid for the convenience of working in the smaller-dimensional phase-shift parameter space.

By "poor tracking" of phase shifts, we mean that phase shifts did not retrace their paths as PSF's attention was directed upward and downward in energy over the studied region of the data. In some cases, several phase shifts would retrace their values of an earlier sweep for a few energies and then take off in a new direction, assuming values different from those in any other sweep. But the parameter set as a whole rarely visited the same point in parameter space twice during these fitting attempts. This suggests that a large number of different sets of phase shifts can produce fits of nearly the same (very good) quality to this angular-distribution data when the data are considered a single energy at a time.

In many of the analyses described above, we attempted to reduce the number of phase shifts varying simultaneously by fixing those that had varied only slightly in previous analyses, or that had varied in what seemed a non-resonant way. (The behavior of a scattering phase shift as a function of energy can be examined by plotting the real and imaginary parts of the related scattering amplitude (see eqn. 4.5) in the complex plane [McV67]. Resonant amplitudes, as parametric functions of increasing scattering energy, evolve along counter-clockwise,

roughly circular trajectories in the plane.) However, the questions of which phases to fix, and at what values to fix them are difficult to answer.

When we fixed phase shifts, chi-square generally increased, as one would naturally expect. Unexpectedly, however, we found little or no improvement in the behavior of the phase shifts left free. They typically did not behave more resonantly than they had before, and the increase in chi-square seemed to be the net effect of fixing previously colluding phase shifts. Evidently, either we never happened on correct values for the fixed phase shifts, or there are very many more overlapping resonances in the data than one would expect.

These are classic problems encountered in phase-shift analyses [Mey88]; the classic solutions are to acquire data from many scattering angles, so that there may be many more data points than parameters in a single-energy fit; and to allow only a few phase shifts to vary at the same time. By taking these steps, one presumably increases the likelihood that a reproducible set of resonant phase shifts will be gotten from the point-by-point fitting procedure.

But fitting to data from a single energy at a time makes very poor use of the information available in the scattering data. The smooth energy dependence of the data would be a very powerful constraint on the phase-shift parameters as functions of energy. We sought alternatives to the classic solution that would allow us to use

this information, and we failed beyond any euphemism: we found no acceptable fits to the data--no fits in which phase shifts both behaved resonantly and reproduced the data.

Our first attempt to make use of the smooth energy dependence in the data was to fit two adjacent (in energy) angular distributions simultaneously with a single parameter set, again sweeping up and down in energy as in the point-by-point fits described above. (I'll call this the "two-by-two method.") An advantage of this procedure is that, at each step, half of the data is the same as in the previous step. Therefore, one expects the recorded phase shifts to have a smoother energy dependence, and to track better from sweep to sweep. In fact, this is what we found in most cases. However, the disadvantage of the two-by-two method is that fits to the data are generally much poorer than in the point-by-point procedure described earlier. At best, the fits generated from phase shifts strikes an average between the two angular distributions simultaneously considered, and values of chi-square are typically much larger than in the point-by-point method. Also, this method seems actively to promote collusion among phase shifts to reproduce excursions in the data.

In another method, we tried to determine phase-shift values probabilistically. We fit angular-distribution data at a single energy, with a large number of different sets of phase shifts, by randomizing the phase-shift values, minimizing with MINUIT until chi-square ceased to improve, and repeating. Typically, a few hundred shots were taken

per energy, and the results were binned for display as functions of energy. Again we found marked indications of collusion among phase shifts and that most phase shifts were varying in ways not suggestive of resonances. Again we tried fixing selected phase shifts; again chi-square increased; again we found little or no improvement in the behavior of the (now distributions of) phase shifts left free.

Finally, we tried fitting parameterized resonances to the data. As discussed in section 4.3.3, fitting overlapping resonances in this way requires many more parameters (six per resonance) than are required in the classical, single-energy, phase-shift fit. It also brings many more data points under simultaneous consideration, and the total number of degrees of freedom generally decreases. In any case, we were unable to reproduce the data using this method, possibly because the time required to generate a fit and compare it with the data was so great (approximately one second) that we could not search the phase-shift parameter space extensively.

The most identifiable problem we encountered in resonance fitting was the inability to strike an effective balance between the number of resonances parameterized and the energy width of the fit region. With one resonance and a narrow enough fit region, we usually obtained good fits with several different resonance spins, parities, and energies. As we widened the fit region, hoping to pin down those parameters by including more information, chi-square became dominated by the ends of the region. We found we could make no further

progress without including additional resonances, whereupon the cycle began again, this time in a parameter space of substantially more dimensions--one which we could not hope to search thoroughly.

There is information in our systematic failure to fit excitation-function data, using PSF's many-energy mode, and our spectacular, but empty, success in fitting with PSF's single-energy mode. The clear implication of these two facts is that the many-energy fit, if it can be done at all, is by far the more definitive technique for analyzing data that contain many overlapping resonances. Unfortunately, there is a real question of whether this method is feasible for routine use with currently available computers.

PSF's many-energy, resonance-fitting mode addresses the problem of finding the *correct* combination of non-resonant phase shifts and resonance parameters, while the classical phase-shift calculation attempts only to find and identify resonances. As a consequence, PSF's resonance-fitting mode, as currently implemented, is an all-or-nothing technique. A compromise seems to be indicated.

## 5.8 Summary

Two previously-studied T = 3/2 states in $^{21}$Na have been observed in high-resolution scattering experiments and re-analyzed to determine resonance parameters. A candidate for the third T = 3/2 state in $^{21}$Na has also been observed and analyzed. Four states that we think are very likely to be the fourth through the seventh T = 3/2 states in $^{21}$Na have been observed in $^{23}$Na(p,t)$^{21}$Na spectra, but not in high-resolution scattering.

We originally intended to tighten the error bars on the resonance parameterizations of the two previously studied T = 3/2 states. Instead, we have found that the effects of correlations, in determining the chi-square goodness of fit to data, among the resonance width, the resonance partial width, and the beam resolution-function width pose a much greater difficulty for the assignment of resonance parameters than was suspected previously. In fact, these correlation effects prevented us from assigning error bars to the parameters at all, and instead, we have simply displayed the effects.

The data acquisition and analysis performed for this thesis were facilitated or made possible by the successful completion of a number of hardware and software development projects; electronic hardware and interface software were developed so that high-resolution, excitation-function data could be acquired with greater accuracy and precision than previously was possible at TUNL.

Central among these developments were the target voltage-ramp system, and the HIRES system of data-acquisition programs. The beam-energy calibration standard at TUNL, a Scanditronix model 751 NMR, was interfaced to CAMAC with electronics and software (the Fortran program NMR) developed for this thesis so that it could participate actively in HIRES-system data acquisition. Also, electronics were developed so that the beam resolution function could be measured, using HIRES-system software, before excitation-function data were acquired.

A relatively new means of fabricating targets for high energy-resolution nuclear-scattering experiments, ion implantation, was employed for this thesis work. Software (the Fortran program RANGE) was written to model the high-dose, low-energy implantation required to produce a target suitable for high-resolution work.

Data-analysis software (the HSYS package of Fortran routines) was written to calculate cross section and analyzing power from scattering yields. Programs (RESFIT and PSF) for resonance and phase-shift fitting were written to help analyze excitation-function data from many scattering angles simultaneously.

## 5.9 Conclusions

This thesis has demonstrated the usefulness of specific techniques in the acquisition and analysis of high energy-resolution, nuclear-scattering data. By exploring the effects of correlations among

resonance parameters and the experimental energy resolution function, it has demonstrated that resonance data alone are not always sufficient to determine accurately the value of the resonance partial width; knowledge of the resolution function or of the branching ratio $\Gamma_p/\Gamma$ may also be required.

Such a finding automatically calls for review of the significance of trends observed in previous resonance partial-width determinations, in which correlations were not systematically explored. Of particular interest here are trends in observed widths that signify violations of isospin conservation in low-mass, A = 4n+1 nuclei: the general increase in those widths with mass number A, and the A = 8 periodicity superimposed on that general increase.

These trends are so strikingly evident in the compiled data (see [Wil82]) that they would survive even 50 percent uncertainties in all of the most recent determinations of resonance partial widths. We don't believe that correlation effects in previous determinations, were they explored, would produce nearly such large uncertainties. However, one might now be inclined toward skepticism of uncertainties much smaller than 10 percent in resonance partial-width determinations.

Figure 5.12 Summary of $T=3/2^{*}$ states in $^{21}Na$

| STATE | $E_x$ in $^{21}F$ (MeV) (A) | $J^{\pi}$ (B) | $E_x$ in $^{21}Na$ (MeV) Previous (C) | Current | $E_p$ (MeV) | $\Gamma$ (eV) | $\Gamma_p$ (eV) | $\gamma^2$ (eV) | $E_x$ of nearby $T=1/2$ states of same $J^{\pi}$ (F) |
|---|---|---|---|---|---|---|---|---|---|
| 1 | 0.0 | $5/2^{+}$ | 8.973±.007 | 8.974±.002 | 6.872±.002 | 650 | 117 | 125 | 8.135, 8.595, 8.827 8.981 |
| 2 | 0.2799 | $1/2^{+}$ | 9.217±.007 | 9.215±.002 | 7.125±.002 | 2800 | 1450 | 477 | 7.253, 8.388, 8.554, 8.742, 8.960, 9.348 |
| 3 | 1.101 | $1/2^{-}$ | | *10.082±.002* | *8.036±.002* | *5475* | *1300* | *504* | 7.575, 7.960, 8.624, 9.775 |
| 4 | 1.730 | | | *10.73±.02* (D) | *(8.72)* (E) | | | | |
| 5 | 1.755 | | | *10.76±.02* (D) | *(8.75)* (E) | | | | |
| 6 | 2.040 | | | *10.96±.02* (D) | *(8.96)* (E) | | | | |
| 7 | 2.071 | | | *10.99±.02* (D) | *(8.99)* (E) | | | | |

* Italicized entries describe states whose $T=3/2$ character is unconfirmed

(A) [End78]

(B) [But68], [Bea70], [Mai81]

(C) [Mcd69]

(D) Princeton

(E) Expected, not seen

(F) [Fer81]; Energies ± .015 MeV

# 6. Suggestions for further work

## 6.1 The target-ramp system.

One problem encountered in acquiring high-resolution resonance data for this thesis stemmed from the limited range of the target-ramp system. Resonances whose effects extend beyond the range of the voltage ramp must be acquired in two or more ramp scans; many of the advantages of the ramping system are lost in such cases.

A 20-kV ramp seems feasible if the target-rod insulation can be shown to withstand such a voltage and if effects from electrons knocked out of the target and accelerated by the resulting potential difference can be controlled. If a 10-kV, fast, programmable supply can be found, a 20-kV ramp can be implemented with current control electronics. Otherwise, if another 5-kV supply should be procured, minor adaptations of the current target-room electronics would suffice minimally.

If such an upgrade is planned, however, it would present a good opportunity to do away with the voltage/frequency conversion presently used and replace it with an analog fiber-optic link.

## 6.2 The beamline slit-feedback system.

Another problem encountered during this research project stemmed from noise generated by the beamline slit-feedback system. This system, intended to keep a frequently jittery beam centered on target, was rarely used in high resolution experiments because it injected enough noise into the 90-90 system supplies to break the NMR-feedback loop.

If an upgrade of this system is planned, it would be a good idea to look into replacing the LH0042 hybrid slit-preamplifiers with, e.g., monolithic JFET amplifiers such as the LF441A. Monolithic amplifiers have improved considerably since the slit-feedback system was designed, and hybrid amplifiers may no longer be the only option.

## 6.3 The beam resolution-function measurement.

The ramp-ramp beam resolution-function measurement can be improved in several ways. Higher beam currents would make the measurement practical with narrower settings of the 90-90 exit slit, decreasing the width of the instrument function (sec. 2.1.6.4.). Since narrower slits would (in the current system) produce more slit scattering, the possibility of thinner slits is worth considering. Unless the slits are being used for feedback control, they needn't stop the beam that hits them, but only slow it down enough that it cannot be transmitted to target.

The problem of hysteresis in the downstream 90-90 magnet can

be addressed minimally by separating the data acquired while the magnetic field is increasing from data acquired while it is decreasing. It has so far been impossible to measure the effect of the hysteresis since the NMR field lock must be maintained while the field in the downstream magnet is changing and (at least) until the system settles after a field step. Attempts to measure fields in both magnets simultaneously (using two NMR Gaussmeters) failed because the NMR signals interfered with each other.

However, if equipped with two probes, the Scanditronix NMR could measure fields in both magnets. After the 90-90 supplies had settled from a magnet-ramp step, the NMR could be instructed to break the feedback loop, switch to a probe installed in the downstream magnet, measure the field in that magnet, switch back to the upstream magnet and re-establish the feedback loop. Such a virtually simultaneous measurement would determine the extent to which upswing ramp steps differ from downswing ramp steps. If the difference were significant, compared to difference in field between successive ramp steps, the data separation discussed above would be indicated.

The multiplexed field measurement required for this test probably should not be done manually, since a sequence of keystrokes must be entered quickly at the Gaussmeter panel, and the sequence must be repeated at least 32 times straight without error. It would be quite easy to write a program to use the NMR interface and make this measurement automatically.

## 6.4 Experimental support for isospin-mixing calculations.

In isospin-forbidden resonance studies, I think the service delivered by recent systematic experimental work [Wil82] has been returned by the even more recent theoretical interest [Orm86], and that the ball is again in "our" court. I do not think that more precise measurements of resonance widths are now called for, however. I think we should find a way of doing what we tried to do in this thesis project: measure the quantities needed for isospin-mixing calculation that can't be determined with accuracy theoretically. The quantities are the spins, parities, and excitation energies of T = 1/2 states in the compound nucleus, and spectroscopic factors for the decay from those states to one or more states in the target nucleus. The spectroscopic factors are important, I think, because they can help in correctly assigning measured excitation energies to calculated wave functions.

## 6.5 Analysis of overlapping resonances.

The analysis of strongly overlapping T = 1/2 resonances attempted in this thesis project showed, I think, the need for a technique intermediate between the classical phase-shift fit and a direct resonance fit. One possibility might be to simplify the excitation-function data--to extract or suppress specific features--with, e. g., the Fourier transform. (An application of the Fourier transform to analysis of resonance data can be found in [Tho84].)

The Fourier transform could be used to remove features of high spatial frequency (e.g., narrow resonances) from excitation-function

data, thus simplifying determination of the non-resonant phase shifts contributing to the data. This could be done by transforming the data into the spatial-frequency domain with the Fourier transform, multiplying the transformed data by a "low-pass" function, and transforming back into the energy domain with the inverse Fourier transform.

To accurate angular-distribution data from many scattering angles, it might be possible to apply a generalization of the Fourier transform, one based not on the circular functions, sin and cos, but on Legendre functions (for cross-section data) or their derivatives (for analyzing-power data). (An example of such a generalization is the Fourier-Bessel, or Hankel, transform, which is based on Bessel functions.)

The intent of such a transformation would be to display the angular-momentum dependence in complex angular-distribution data in a form more accessible to humans. It is very difficult to look at angular distributions of data as complex as the data in figure 5.11, and divine the spins and parities of any of the overlapping resonances, or even to determine what constitutes a resonance in the data. Should a reasonable Fourier-Legendre transform exist, application of it might be used to distinguish overlapping resonances of different L's from each other. In such use, the transform would be valuable even if no inverse transform could be found.

# 7. Appendix

Schematic diagrams of the target voltage-ramp system.

(See also the block diagram in sec. 2.1.5.2.)

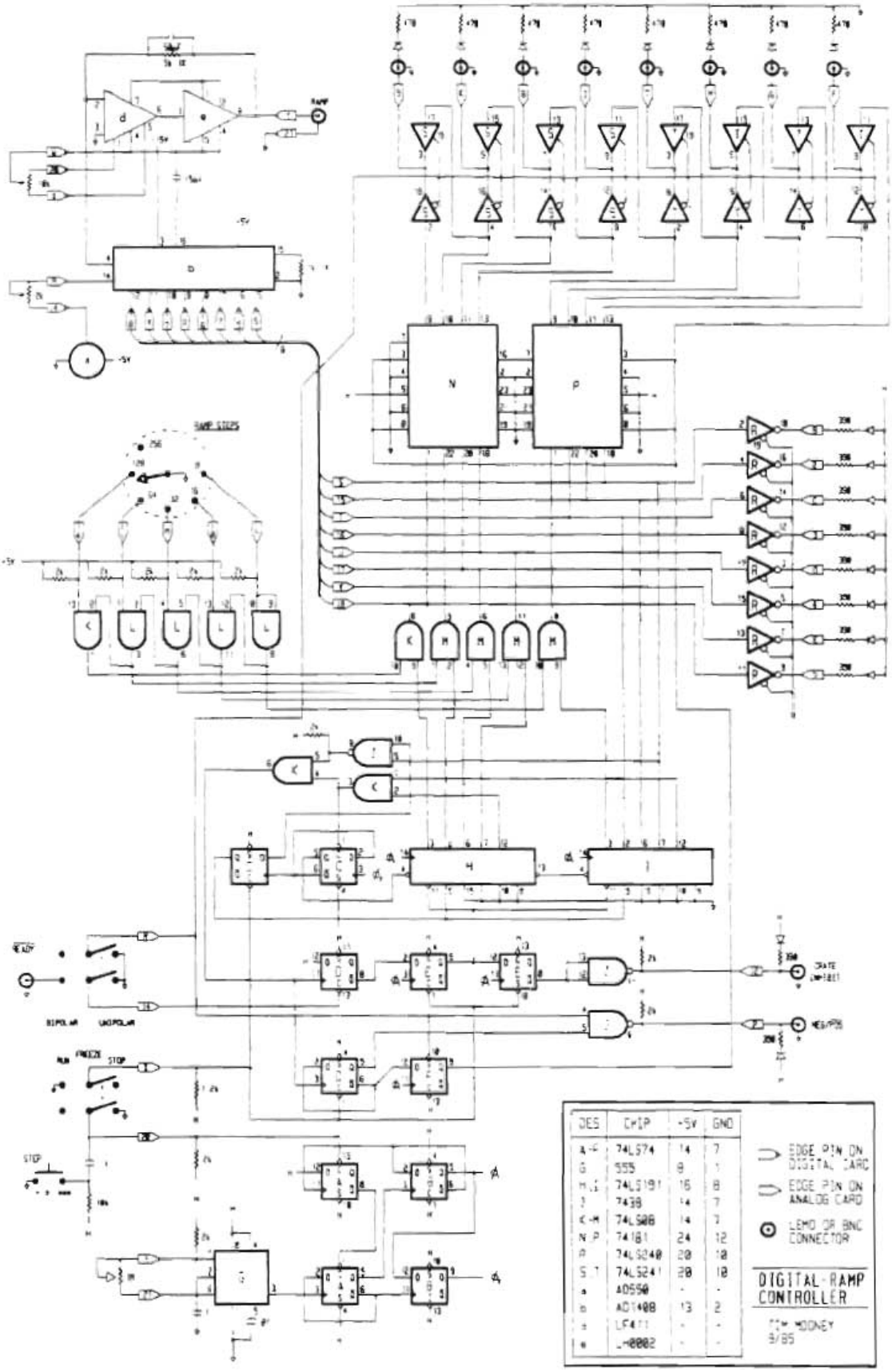
RAMP STEPS
FREEZE
RUN
STOP
BIPOLAR
UNIPOLAR
DES | CHIP | +5V | GND
A-C | 74LS74 | 14 | 7
G | 555 | 8 | 1
H,I | 74LS191 | 16 | 8
J | 7439 | 14 | 7
K-M | 74LS08 | 14 | 7
N,P | 74181 | 24 | 12
R | 74LS240 | 20 | 10
S,T | 74LS241 | 20 | 10
a | AD550 | - | -
b | AD1408 | 13 | 2
c | LF411 | - | -
e | J-0002 | - | -
EDGE PIN ON DIGITAL CARD
EDGE PIN ON ANALOG CARD
LEMO OR BNC CONNECTOR
DIGITAL-RAMP CONTROLLER
TIM MOONEY
9/85

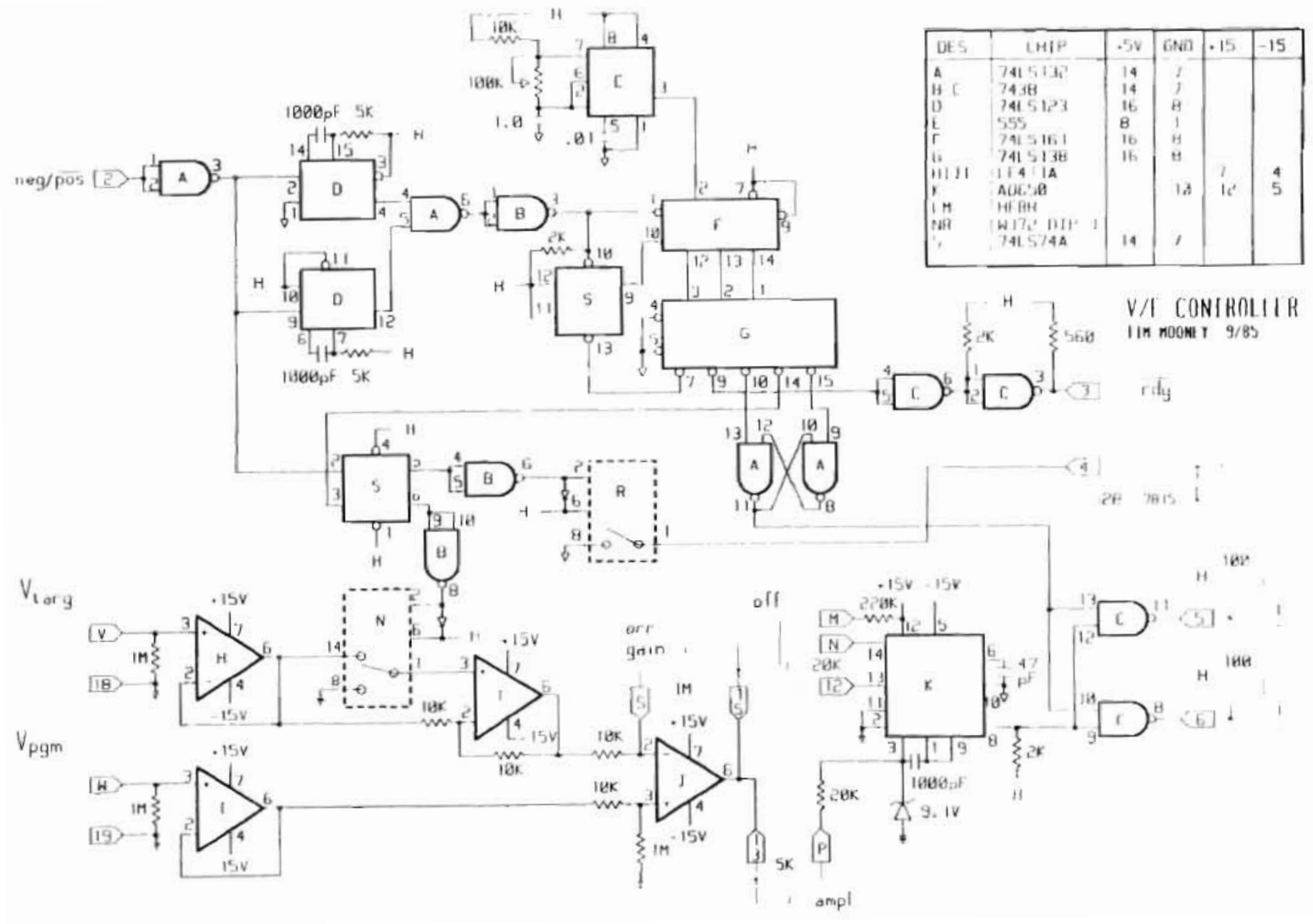


| DES | CHIP | +5V | GND | +15 | -15 |
|---|---|---|---|---|---|
| A | 74LS136 | 14 | 7 | | |
| B C | 7438 | 14 | 7 | | |
| D | 74LS123 | 16 | 8 | | |
| E | 555 | 8 | 1 | | |
| F | 74LS161 | 16 | 8 | | |
| G | 74LS138 | 16 | 8 | | |
| H I J | LF411A | | | 7 | 4 |
| K | AD630 | | 13 | 14 | 5 |
| L M | HEBN | | | | |
| NR | W17C DIP 1 | | | | |
| S | 74LS74A | 14 | 7 | | |

## References


[Ada66] J. L. Adams, W. J. Thompson, and D. Robson, Nucl. Phys. 89 (1966) 377.

[Alm61] O. Almen and G. Bruce, Nucl. Instr. and Meth. 11 (1961) 257.

[Ari71] A. Arima and S. Yoshida, Nucl. Phys. 161 (1971) 492.

[Aue71] N. Auerbach and A. Lev, Phys. Lett. 34B (1971) 13.

[Aue83] N. Auerbach, Physics Reports 98 (1983) 273.

[Bay66] B. F. Bayman, Amer. J. Phys. Vol. 43, No. 3, 216 (1966).

[Bea70] R. C. Bearse et al., Phys. Rev. Lett. C1 (1970) 608.

[Bet53] H. A. Bethe and J. Ashkin, in *Experimental Nuclear Physics*, Vol. 1, ed. E. Segre (Wiley, New York, 1953) part 2, p. 166.

[Bic75] Hans Bichsel and Roberta P. Saxon, Phys. Rev. A11 (1975) 1286.

[Ble78] M. E. Bleck, Ph.D. dissertation, Duke University, 1978 (unpublished), available from University Microfilms International, 300 N. Zeeb Rd., Ann Arbor, MI 48106.

[Boh69] A. Bohr and B. R. Mottleson, *Nuclear Structure* (Benjamin, New York, 1969).

[Bro70] K. L. Brown and S. K. Howrt, SLAC Report No. 91 (1970).

[Bur83] B. Burks, Ph.D. dissertation, University of North Carolina,

1983 (unpublished), available from University Microfilms International, 300 N. Zeeb Rd., Ann Arbor, MI 48106.

[But68] G. W. Butler et al., Phys. Rev. 166 (1968) 1096.

[Chu78] W. K. Chu, M. A. Nicolet, *Backscattering Spectrometry*, (Academic Press, New York, 1978).

[Cla71] R.G. Clarkson, Nelson Jarmie, Comp. Phys. Commun. 2 (1971) 433.

[Cle74] T. B. Clegg et al., Nucl. Instr. and Meth. 57 (1974) 167.

[End78] P. M. Endt and C. Van der Leun, Nucl. Phys. A310 (1978) 1.

[Fer81] M. Fernandez et al., Nucl. Phys. A369 (1981) 425.

[Gib75] James F. Gibbons et al., *Projected Range Statistics*, 2nd edition, (Drowden, Hutchinson & Ross, Inc., 1975).

[Gou73] R. A. Gough, R. G. Sextro and J. Cerny, Phys. Lett. 43B (1973) 33.

[Gou81] C. R. Gould et al., IEEE Trans. Nucl. Sci. NS-28 (1981) 3708.

[Hin84] F. Hinterberger et al., Nucl. Phys. A424 (1984) 335.

[Jam75] F. James and M. Roos, Comp. Phys. Commun. 10 (1975) 343.

[Jan69] J. Janecke, in *Isospin in Nuclear Physics*, ed. D. H. Wilkinson (North Holland Publishing Company, Amsterdam, 1969).

[Jar78] Nelson Jarmie et al., Comp. Phys. Commun. 13 (1978) 317.

[Kar85] B. C. Karp, private communication.

[Kou74] R. T. Kouzes, Ph.D. dissertation, Princeton University, 1974 (unpublished), available from University Microfilms International, 300 N. Zeeb Rd. Ann Arbor, MI 48106.

[Kou78] R. T. Kouzes, Nucl. Instr. and Meth. 155 (1978) 261.

[Lan44] L. Landau, J. Phys. USSR 8 (1944) 201.

[Lin61] J. Lindhard, M. Scharff, and H. E. Schiott, Mat. Fys. Medd. Dan. Vid. Selsk. 33, No. 14 (1963).

[Mai81] G. Mairle et al., Nucl. Phys. A363 (1981) 413.

[McD69] A. B. McDonald, J. R. Patterson, and H. Winkler, Nucl. Phys. A137 (1969) 545.

[McD76] A. B. McDonald et al., Nucl. Phys. A273 (1976) 451, 464, 477.

[McV67] K. W. McVoy, *Fundamentals in Nuclear Theory*, ed. A. de-Shalit and C. Villi (IAEA, Vienna 1967).

[Mey76] H. O. Meyer et al., Nucl. Phys. A269 (1976) 269.

[Mey88] H. O. Meyer, private communication.

[Mos65] S. J. Moss and W. Haeberli, Nucl. Phys. 72 (1965) 417.

[Orm86] W. E. Ormand, Ph.D. dissertation, Michigan State University, 1986 (unpublished), available from University Microfilms International, 300 N. Zeeb Rd., Ann Arbor, MI 48106.

[San68] J. B. Sanders, Can. J. Phys. 46 (1968) 445.

[Sch67] P. Schulek et al., Soviet J. Nucl. Phys. 4 (1967) 400.

[Sch71] P. Schwandt, T. B. Clegg, and W. Haeberli, Nucl. Phys. A163 (1971) 432.

[Sil59] E. A. Silverstein, Nucl. Instr. and Meth. 4 (1959) 53.

[Tho68] W. J. Thompson, J. L. Adams, and D. Robson, Phys. Rev. 173 (1968) 975.

[Tho84] W. J. Thompson, Computing in Applied Science (Wiley, New York 1984).

[Var86] R. L. Varner, Ph.D. dissertation, University of North Carolina, 1986 (unpublished), available from University

Microfilms International, 300 N. Zeeb Rd. Ann Arbor, MI 48106.

[Vav57] P. V. Vavilov, Sov. Phys.--JETP **5** (1957) 749.

[Wil82] J. F. Wilkerson, Ph.D. dissertation, University of North Carolina, 1982 (unpublished), available from University Microfilms International, 300 N. Zeeb Rd., Ann Arbor, MI 48106.

[Wil83] J. F. Wilkerson et al., Phys. Rev. Lett. **51** (1983) 2269.